박 사 학 위 논 문

Ph.D. Dissertation

2D-MITC4 솔리드 및 MITC4+ 쉘 유한요소의 개선

Improvement of 2D-MITC4 solid and MITC4+ shell finite elements

2022

최 형 규 (崔 亨 圭 Choi, Hyung-Gyu)

한 국 과 학 기 술 원

Korea Advanced Institute of Science and Technology

박 사 학 위 논 문

박 사 학 위 논 문

2D-MITC4 솔리드 및 MITC4+ 쉘 유한요소의 개선

2022

최 형 규

한 국 과 학 기 술 원

기계항공공학부/기계공학과

2D-MITC4 솔리드 및 MITC4+ 쉘 유한요소의 개선

최 형 규

위 논문은 한국과학기술원 박사학위논문으로
학위논문 심사위원회의 심사를 통과하였음

2022년 12월 8일

심사위원장 이 필 승 (인)

심 사 위 원 윤 정 환 (인)

심 사 위 원 유 승 화 (인)

심 사 위 원 전 형 민 (인)

심 사 위 원 김 산 (인)

Improvement of 2D-MITC4 solid and MITC4+ shell finite elements

Hyung-Gyu Choi

Advisor: Phill-Seung Lee

A dissertation submitted to the faculty of
Korea Advanced Institute of Science and Technology in
partial fulfillment of the requirements for the degree of
Doctor of Philosophy in Mechanical Engineering

Daejeon, Korea
December 8, 2022

Approved by

Phill-Seung Lee
Professor of Mechanical Engineering

The study was conducted in accordance with Code of Research Ethics[1].

1) Declaration of Ethical Conduct in Research: I, as a graduate student of Korea Advanced Institute of Science and Technology, hereby declare that I have not committed any act that may damage the credibility of my research. This includes, but is not limited to, falsification, thesis written by someone else, distortion of research findings, and plagiarism. I confirm that my dissertation contains honest conclusions based on my own careful research under the guidance of my advisor.

DME

최형규. 2D-MITC4 솔리드 및 MITC4+ 쉘 유한요소의 개선. 기계공학과. 2022년. 91+ix 쪽. 지도교수: 이필승. (영문 논문)

Choi, Hyung-Gyu. Improvement of 2D-MITC4 solid and MITC4+ shell finite elements. Department of Mechanical Engineering. 2022. 91+ix pages. Advisor: Lee, Phill-Seung. (Text in English)

Abstract

The objectives of this thesis were to develop a new 4-node quadrilateral solid (2D-MITC4) and shell (MITC4+) finite elements to improve the predictive capabilities, especially in distorted meshes. The proposed elements consist of two key concepts including the new assumed membrane strain field and the geometry dependent Gauss integration scheme. More specifically, the complicated assumed strain field of the previous 2D-MITC4 solid and MITC4+ shell elements are simplified and become more intuitive by directly using the strain coefficients. In addition, the geometry dependent Gauss integration is introduced to improve the membrane performance of the proposed elements. The geometry dependent Gauss integration with the new assumed strain field provides smoother solutions and good convergence, and thus the proposed elements can be used with relatively coarse meshes. In addition, it needs no additional degrees of freedom and does not reveal any numerical instability that is shown in the incompatible modes element. The new 2D-MITC4 solid and MITC4+ shell elements pass the three basic numerical tests: including zero energy mode, isotropy, and corresponding patch tests. It has been also thoroughly demonstrated that the proposed elements are very effective and reliable both in linear and nonlinear problems.

Keywords Finite element analysis; structural analysis; 4-node 2D finite element; MITC method; Numerical quadrature; Mesh distortion

Contents

Chapter 1. Introduction 1
1.1. Research background 1
1.2. Research objectives and scope 2
Chapter 2. New 4-node quadrilateral solid finite element 5
2.1. Geometry and displacement interpolations 6
2.2. Original 2D-MITC4 solid element 9
2.2.1. Assumed strain field 9
2.2.2. Formulation of the original 2D-MITC4 element 10
2.2.3. Treatment of the volumetric locking 11
2.3. New 2D-MITC4 solid element 12
2.3.1. Simplified assumed strain field 12
2.3.2. Classification of distortion 12
2.3.3. Geometry dependent Gauss integration 14
2.4. Basic numerical tests 18
2.5. Numerical examples for linear analysis 19
2.5.1. Cantilever problem 20
2.5.2. Cantilever beam with distortion parameter 21
2.5.3. Cook's skew beam 22
2.5.4. Curved beam 26
2.5.5. Block under complex body force 30
2.6. Numerical examples for nonlinear analysis 34
2.6.1. Block subjected to a compression force 34
2.6.2. Column under an eccentric load 36
Chapter 3. New 4-node quadrilateral shell finite element 38
3.1. Geometry and displacement interpolations 39
3.2. Original MITC4+ shell element 42
3.2.1. Treatment of transverse shear locking 42
3.2.2. Treatment of membrane locking 44
3.3. New MITC4+ shell element 48
3.3.1. New assumed strain field 48
3.3.2. Formulation of the new MITC4+ shell element 50
3.4. Basic numerical tests 54
3.5. Numerical examples for linear analysis 54
3.5.1. Square plate 57
3.5.2. Cylindrical shell 59
3.5.3. Hyperboloid shell 62

3.5.4. Scordelis-Lo roof 65
3.5.5. Hyperbolic cylinder shell 68
3.6. Numerical examples for nonlinear analysis 70
3.6.1. Thin curved beam 71
3.6.2. Slit annular plate 73
3.6.3. Hemispherical shell 77
Chapter 4. Conclusions 80
Appendix A. Physical strain patterns 81
Appendix B. Modification on Gauss integration point 82
Appendix C. Coupling distortion measure with adjusting parameter 85
Bibliography 87

List of Tables

Table 2.1. Normalized eigenvalues of stiffness matrix of single 2D-MITC4 element according to adjusting parameter μ . The original 2D-MITC4 element corresponds to $\mu = 1$. The eigenvalues are normalized by Young's modulus. 15

Table 2.2. Relative errors in the tip displacement ($\left| v_{ref} - v_h \right| / v_{ref} \times 100$) at point A in the cantilever problem. 20

Table 2.3. Relative errors in the *xx*-component of stress ($\left| \sigma_{ref} - \sigma_{xx/h} \right| / \sigma_{ref} \times 100$) at the support point B in the cantilever problem. 21

Table 2.4 Relative errors in the vertical displacement ($\left| v_{ref} - v_h \right| / v_{ref} \times 100$) at point A in Cook's skew beam. 24

Table 2.5 Relative errors in the horizontal displacement ($\left| u_{ref} - u_h \right| / u_{ref} \times 100$) at point A in Cook's skew beam. 25

Table 3.1. 4-node quadrilateral shell elements based on MITC method and descriptions. 42

Table 3.2. Comparison of the formulation between the improved MITC4+ and new MITC4+ shell elements 51

Table 3.3. List of six benchmark problems considered for the convergence studies. 54

Table 3.4. Considered shell elements and characteristics. 70

Table B.1. Strain energy with modified Gauss integration for Cook's beam with 4x4 elements mesh. 82

List of Figures

Fig. 2.1. A 4-node quadrilateral element in (a) the global Cartesian coordinate system and (b) the natural coordinate system. 6
Fig. 2.2. Characteristic geometry vectors. (a) Two vectors $\mathbf{x}_r$ and $\mathbf{x}_s$ correspond to covariant base vectors at the element center. (b) The vector $\mathbf{x}_d$ denotes in-plane distortion. 7
Fig. 2.3. Five tying points used to construct the assumed strain field of the original 2D-MITC4 element. 9
Fig. 2.4. Classification of distortion for 4-node quadrilateral element. (a) Characteristic vectors, (b) skewness, (c) taper in *r*-direction, and (d) taper in *s*-direction............ 13
Fig. 2.5. Integration points for (a) standard Gauss integration and (b) geometry dependent Gauss integration. 14
Fig. 2.6. Distorted element for eigenvalue analysis. 15
Fig. 2.7. Change in normalized eigenvalues of each deformation mode according to adjusting parameter μ 16
Fig. 2.8. Adjusting parameter and skew angle. (a) Adjusting parameter according to the skew angle. (b) Element geometries with skew angles $\theta = 0$, $\pi/8$, $\pi/4$, and $3\pi/8$. 17
Fig. 2.9. The distortion angle θ corresponding to the angle between covariant and contravaiant base vectors at the element center. The distortion angle satisfies the above proposed requirements.... 17
Fig. 2.10. Mesh pattern used for the patch tests............ 18
Fig. 2.11. Geometries for zero energy mode and isotropy tests. 18
Fig. 2.12. Mesh patterns used to numerical problems. (a) Regular and (b) distorted mesh patterns when $N = 4$ 19
Fig. 2.13. Cantilever problem ($E = 3\times10^4$ and $\nu = 0$). (a) regular mesh. (b) distorted mesh. 20
Fig. 2.14. Cantilever beam (E=1500 and ν=0.25) modeled using two elements with distortion parameter (e). 21
Fig. 2.15. Normalized vertical displacements (v_h/v_{ref}) at point A according to the distortion parameter (e). 22
Fig. 2.16. Cook's skew beam ($E = 1$ and $\nu = 1/3$). (a) Regular mesh when $N = 4$. (b) Distorted mesh when $N = 4$ 22
Fig. 2.17. Convergence curves for Cook's skew beam. The bold line represents the optimal convergence rate. 23
Fig. 2.18. Normalized vertical displacements (v_h/v_{ref}) at point A in Cook's skew beam............ 24
Fig. 2.19. Normalized horizontal displacements (u_h/u_{ref}) at point A in Cook's skew beam............ 25
Fig. 2.20. Shear stress (σ_{xy}) distributions calculated in Cook's skew beam using distorted meshes with $N = 8$. The reference stress distribution is obtained using a 64×64 mesh of 9-node quadrilateral

elements. 26
Fig. 2.21. Curved beam ($E = 1\times 10^3$ and $\nu = 0$). (a) 4×4 regular mesh, (b) 4×4 distorted mesh. 26
Fig. 2.22. Convergence curves for the curved beam. The bold line denotes the optimal convergence rate. 27
Fig. 2.23. Normalized vertical displacements (v_h/v_{ref}) at point A in the curved beam. 27
Fig. 2.24. von Mises stress (τ_{vM}) distributions of the curved beam problem obtained by using 16×16 distorted meshes. The reference stress distribution is obtained using a 64×64 mesh of 9-node quadrilateral elements. 28
Fig. 2.25. von Mises stress distributions along the arc AB of the curved beam problem for (a) 8×8, (b) 16×16 and (c) 32×32 distorted meshes. 29
Fig. 2.26. Clamped box under complex body force problem ($E = 2\times 10^7$ and plane strain conditions with $\nu = 0.47$, 0.49 or 0.499 for nearly incompressible materials). (a) Regular mesh when $N = 4$. (b) Distorted mesh I when $N = 4$ 30
Fig. 2.27. Convergence curves for the clamped box under complex body force problem with regular meshes. 30
Fig. 2.28. Convergence curves for the clamped box under complex body force problem with distorted meshes I. Nearly incompressible material properties are considered. The bold line denotes the optimal convergence rate. 31
Fig. 2.29. Distorted mesh II when (a) $N = 2$, (b) $N = 2$, (c) $N = 8$ and (d) $N = 16$ 32
Fig. 2.30. Convergence curves for block under body force. The bold line denotes the optimal convergence rate. 32
Fig. 2.31. Normalized (a) horizontal (u_h/u_{ref}) and (b) vertical (v_h/v_{ref}) displacements at point A in block under body force considering regular meshes. 33
Fig. 2.32. Normalized (a) horizontal (u_h/u_{ref}) and (b) vertical (v_h/v_{ref}) displacements at point A in block under body force considering distorted meshes I. 33
Fig. 2.33. Normalized (a) horizontal (u_h/u_{ref}) and (b) vertical (v_h/v_{ref}) displacements at point A in block under body force considering distorted meshes II. 33
Fig. 2.34. Block subjected to a compression force with 12×30 mesh ($E = 1\times 10^3$, $\nu = 0.3$ and $p_{\max} = -98$). 34
Fig. 2.35. Load-displacement curves at the point A in the block subjected to a compression force. The deformed shapes at the load step $p/p_{\max} = 0.5125$ are given in Fig. 2.36. 35
Fig. 2.36. The deformed configurations of the block subjected to a compression force at the load step $p/p_{\max} = 0.5125$ with magnifying the displacements two times: (a) Standard 9-node element, (b) Incompatible modes element, (c) Improved 2D-MITC4 element. 35
Fig. 2.37. Column under an eccentric load ($E = 10^6$, $\nu = 0$ and $P_{\max} = 4.5\times 10^3$) modeled with (a) 2×10 regular mesh and (b) 2×10 distorted mesh. 36

Fig. 2.38. Load-displacement curves ($-v_A$) for the column under an eccentric load for regular and distorted meshes. 36
Fig. 2.39. Load-displacement curves (u_A) of the column under an eccentric load for regular and distorted meshes.......... 37
Fig. 2.40. Deformed configurations of the column under an eccentric load at the initial, middle and final load steps obtained by 2×10 distorted meshes. The reference solutions obtained by 20×100 mesh of standard 9-node element. 37
Fig. 3.1. Geometry of a 4-node quadrilateral shell element. 39
Fig. 3.2. Charateristic geometry vectors for a 4-node quadrilateral shell element. (a) Two vectors $\mathbf{x}_r$ and $\mathbf{x}_s$ in the plane *P* with normal vector $\mathbf{n}$. (b) Distortion vector $\mathbf{x}_d$. 41
Fig. 3.3. Tying points (*A*)-(*D*) for the assumed transverse shear strain field of the MITC4 element and the corresponding strain components.......... 42
Fig. 3.4. Constant transverse shear strain is assumed along its edges. (a) Strain component e_{rt} is assumed constant in *r* direction. (b) Strain component e_{st} is assumed constant in *s* direction. ... 43
Fig. 3.5. Warped distortion in a 4-node quadrilateral shell element.......... 44
Fig. 3.6. Tying points (*A*)-(*E*) for the assumed membrane strain field of the MITC4+ element and the corresponding strain components. 45
Fig. 3.7. Temporal tying points for the new assumed membrane strain field to improve the membrane performance of the MITC4+ element. The tying points are merged into the element center........ 48
Fig. 3.8. Skewness of the 4-node quadrilateral shell element. (a) In-plane vectors $\mathbf{x}_r$ and $\mathbf{x}_s$ in the 3D space. (b) Skewness θ in the *r*-*s* space. 52
Fig. 3.9. The geometry for the patch tests and the boundary conditions for each test. 54
Fig. 3.10. $N\times N$ regular mesh pattern with $N=4$ 55
Fig. 3.11. $N\times N$ distorted mesh patterns with (a) $N=4$ and (b) $N=8$. 56
Fig. 3.12. Descripstion of the square plate problem. (a) Plate subjected to an uniform pressure ($p=1.0$). (b) Square plate with $E=1.7472\times10^7$, $\nu=0.3$, and $L=1.0$ 57
Fig. 3.13. Convergence curves for the square plate problem with fully clamped conditions considering (a) regular meshes and (b) distorted meshes. The bold line denotes the optimal convergence rate. 58
Fig. 3.14. Description of the cylindrical shell problem. (a) Cylindrical shell subjected to a smoothly varing pressure ($L=R=1.0$, $E=2.0\times10^5$, $\nu=1/3$, and $p_0=1.0$). (b) Pressure loading 59
Fig. 3.15. $N\times N$ element mesh with (a) regular and (b) distorted mesh patterns when $N=4$ 59
Fig. 3.16. Convergence curves for the cylindrical shell problem with fully clamped conditions considering (a) regular meshes and (b) distorted meshes. The bold line denotes the optimal convergence rate. 60
Fig. 3.17. Convergence curves for the cylindrical shell problem with free conditions considering (a) regular meshes and (b) distorted meshes. The bold line denotes the optimal convergence rate. .. 61

Fig. 3.18. Description of the hyperboloid shell problem. (a) hyperboloid shell ($L = 1.0$, $E = 2.0\times10^{11}$, and $\nu = 1/3$). (b) Smoothly varing pressure loading ($p_0 = 1.0$). 62
Fig. 3.19. $N \times N$ element mesh with (a) regular and (b) distorted mesh patterns when $N = 8$ 63
Fig. 3.20. Convergence curves for the hyperboloid shell problem with fully clamped conditions considering (a) regular meshes and (b) distorted meshes. The bold line denotes the optimal convergence rate. 63
Fig. 3.21. Convergence curves for the hyperboloid shell problem with free conditions considering (a) regular meshes and (b) distorted meshes. The bold line denotes the optimal convergence rate. .. 64
Fig. 3.22. Description of the Scordelis-Lo roof problem ($L = R = 25.0$, $E = 4.32\times10^{8}$, $\nu = 0.0$, and self-weight is 90 per unit area) with 4×4 regular mesh. 65
Fig. 3.23. $N \times N$ distorted mesh patterns with (a) distorted I and (b) distorted II when $N = 4$ 65
Fig. 3.24. Convergence curves for the Scordelis-Lo roof problem with rigid diaphragm conditions considering regular mesh patterns. The bold line denotes the optimal convergence rate. 66
Fig. 3.25. Convergence curves for the Scordelis-Lo roof problem with rigid diaphragm conditions considering distorted mesh patterns (distorted I). The bold line denotes the optimal convergence rate. 66
Fig. 3.26. Convergence curves for the Scordelis-Lo roof problem with rigid diaphragm conditions considering distorted mesh patterns (distorted II). The bold line denotes the optimal convergence rate. 67
Fig. 3.27. Description of the hyperbolic cylinder shell problem ($L = 2$, $E = 2.0\times10^{11}$, and $\nu = 1/3$). (a) Problem discriptions with 4×4 regular mesh. (b) 4×4 distorted mesh. 68
Fig. 3.28. Convergence curves for the hyperbolic cylinder shell problem with partly clamped conditions considering (a) regular meshes and (b) distorted meshes. The bold line denotes the optimal convergence rate. 69
Fig. 3.29. Description of the thin curved beam problem ($R_1 = 4.12$, $R_2 = 4.32$, $t = 0.1$, $E = 1.0\times10^{7}$, $\nu = 0.25$, and $P_1 = P_2 = 100$) with 1×6 regular mesh. 71
Fig. 3.30. Load-displacement curves of the thin curved beam problem for (a) $-u_A$ and (b) w_A 71
Fig. 3.31. Deformed configurations of the thin curved beam problem at several load steps with (a) MITC4, (b) MITC4+ and (c) new MITC4+ elements. (d) The reference solution with MITC9 element. 72
Fig. 3.32. Description of the slit annular plate problem ($R_1 = 6$, $R_2 = 10$, $t = 0.03$, $E = 2.1\times10^{7}$, $\nu = 0$ and $p = 0.8$) with 3×24 (a) regular and (b) distorted meshes. 73
Fig. 3.33. Deformed configurations of the slit annular plate problem considering 3×24 regular mesh of (a) MITC4, (b) MITC4+ and (c) new MITC4+ elements. (d) The reference solution with MITC9 element. 74
Fig. 3.34. Deformed configurations of the slit annular plate problem considering 3×24 distorted mesh of (a) MITC4, (b) MITC4+ and (c) new MITC4+ elements. (d) The reference solution with MITC9

element..75
Fig. 3.35. Load-displacement curves of the slit annular plate problem with 3×24 regular mesh at the points (a) C and (b) A 76
Fig. 3.36. Load-displacement curves of the slit annular plate problem with 3×24 distorted mesh at the points (a) C and (b) A 76
Fig. 3.37. Description of the hemispherical shell problem ($R=10$, $\varphi_0=18°$, $t=0.04$, $E=6.825\times 10^7$, $\nu=0.3$, $P=400$) with 12×12 (a) regular and (b) distorted meshes............77
Fig. 3.38. Deformed configurations of the hemispherical shell problem using the 12×12 regular mesh of the new MITC4+ shell element at the load steps of (a) $P=0.25P_{\max}$, (b) $P=0.5P_{\max}$, (c) $P=0.75P_{\max}$ and (d) $P=P_{\max}$ 78
Fig. 3.39. Load-displacement curves of the hemispherical shell problem at the point A and B with 12×12 (a) regular and (b) distorted mesh. 79
Fig. A.1. Physical strain patterns with the characteristic geometry and displacement vectors. (a) stretching strain patterns, (b) shearing strain patterns, and (c) bending strain patterns. 81
Fig. B.1. Possible ways to modify Gauss integratin points. (a) Rotation, (b) Scaling, and (c) Rotation and scaling. 82
Fig. B.2. Strain energy obtained from rotation modification for each element in Cook's beam. 83
Fig. B.3. Strain energy obtained from scaling modification in Cook's beam. 83
Fig. B.4. Optimally modified Gauss points based on (a) rotation and (b) scaling. 84
Fig. C.1. Cantilever beam (E = 1500 and ν = 0.25) modeled using two elements with distortion parameter (e)..85
Fig. C.2. Distortion measures. (a) skewness, (b) tapered, and (c) overall distortion. 85
Fig. C.3. Normalized vertical displacement in the cantilever beam with two elements at point A 86

Chapter 1. Introduction

1.1. Research background

For the past several decades, the finite element method (FEM) has been widely used for solving various engineering problems [1-3]. FEM can easily handle complex geometries using element meshes. Among various finite elements, low-order finite elements such as 4-node quadrilateral and 3-node triangular elements are often preferred due to simple implementation and computational efficiency compared with higher-order finite elements. However, low-order finite elements show insufficient predictive capability, especially in distorted meshes [4-9]. For this reason, many researchers still devote to developing finite elements that give more accurate and reliable solutions in a computationally efficient way [10-13].

There are major considerations when developing finite elements. For general use, ideal finite elements should pass the basic tests (patch, zero energy mode, and isotropy tests) and show optimal convergence behavior that provides a more accurate solution as more elements are used. However, under certain conditions including element geometries and material properties, the performance of finite elements substantially deteriorates and it is hard to obtain the optimally converged solution [4-7]. In general, finite elements reveal undesirable overly stiff behavior when they are distorted and this stiffening effect of the distorted element becomes more severe especially in low-order elements such as 4-node quadrilateral and 3-node triangular elements [4-7,14-16].

There have been various approaches used to improve the performance of finite elements, including reduced integration [17-20], assumed strain method, and use of incompatible modes [21,22]. The reduced integration method employs a single Gauss quadrature point at the element center instead of the standard 2×2 Gauss quadrature when constructing the stiffness matrix. The 4-node quadrilateral element with the reduced integration method shows excellent performance by alleviating in-plane shear locking. Moreover, the reduced integration method is also used in plate and shell finite elements to improve membrane behavior and reduce membrane locking. While the reduced integration method decreases the computational cost and improves the performance of finite elements, it reveals spurious zero energy modes that finite elements should not show.

The method of incompatible modes has been successfully used for low-order finite elements [23-27]; in this method, incompatible modes are adopted to enrich the displacement field of a finite element and corresponding degrees of freedom (DOFs) are added. The use of incompatible modes could be generalized into the enhanced assumed strains (EAS) method. Regardless of the further computational expense needed to handle the additional DOFs, the incompatible modes element has been widely employed in commercial software due to its excellent accuracy improvement in bending problems. While the incompatible modes element provides improved bending behavior and also alleviates the volumetric locking, it reveals spurious instabilities in the nonlinear analysis [12,28].

The mixed interpolation of tensorial components (MITC) method has been extensively employed to develop various solid and structural elements since it was first proposed to reduce transverse shear locking for a 4-node quadrilateral shell element (MITC4) [29]. Finite elements based on the MITC method effectively alleviate various types of locking without using additional degrees of freedom and do not show spurious instabilities in the both linear and nonlinear analysis [30-40]. In addition, the extension of the formulation to the nonlinear analysis could be accomplished once a linear formulation has been successfully developed.

Recently, Ko et al. developed the MITC4+ shell element, in which membrane locking is also reduced using the MITC method. The 2D and 3D MITC solid elements were also developed. Subsequently, the improved MITC4+ shell element was developed by adopting the assumed strain field of the 2D MITC solid elements. Their excellent performance has been demonstrated in both linear and nonlinear analysis.

In spite of the excellent performance of finite elements based on the MITC method, there is still room to improve the accuracy of the low order elements. The 4-node quadrilateral MITC element also suffers from performance deterioration due to the element distortion as other elements. For example, although the low order solid (2D-MITC4) and shell (MITC4+) elements show almost optimal performance in the uniform meshes [30,36], the performance substantially deteriorates when they are used in distorted meshes like other elements.

We focus on improving the convergence behavior of the 2D-MITC4 solid and MITC4+ shell elements in distorted meshes while preserving the promising properties of the MITC method aforementioned. To make the elements insensitive to distortion, the geometry dependent Gauss integration scheme is introduced in which the geometry distortion of an element is measured and used to adjust the position of Gauss integration points. In addition, the new assumed strain field that makes the original formulation simplified is proposed and collaborated with the geometry dependent Gauss integration scheme. Since the MITC4+ shell element is identical to the standard 4-node quadrilateral solid element when it is used for in-plane problems [36], the simplified assumed strain field and the geometry dependent Gauss integration scheme are extended to the MITC4+ shell element to improve its membrane performance.

1.2. Research objectives and scope

The objectives of this thesis are to make the low order quadrilateral MITC elements robust to the element distortion and also simplify the formulation of the elements. The 2D-MITC4 solid and MITC4+ shell finite elements are considered here. The formulation of the new 2D-MITC4 solid and MITC4+ shell elements are presented in detail and thoroughly studied in both geometrically linear and nonlinear analysis problems. In addition, the new 2D-MITC4/1 solid element is presented which employs the assumption of the constant volumetric strain and it shows improved behaviors in both plane stress and strain problems.

In the case of the previous 2D-MITC4 solid element, the formulation is complicated because of using the strain coefficients to express the assumed strain field. For the new 2D-MITC4 solid element, the formulation is rewritten with characteristic vectors directly and it becomes intuitive and simple. The simplified formulation provides results identical to the previous 2D-MITC4 solid element. To improve its performance further, the geometry dependent Gauss integration scheme is introduced. The positions of Gauss integration points are moved into the element center in accordance with the skew angle of the element distortion.

In order to investigate whether the modification of integration points can actually improve the bending performance, eigenvalues of a stiffness matrix of a single element are calculated. Through the numerical experiment, it is confirmed that geometry dependent Gauss integration scheme can selectively reduce the bending stiffness without affecting the constant strain modes. To adjust the bending stiffness depending on the geometry of the element, an adjusting parameter is introduced and practical requirements are summarized. We here present a function that satisfies the requiremenets and provides improved performance in the range of the overall distortion.

When the geometry dependent Gauss integration scheme is employed to analyse the geometrically nonlinear problems, the element distortion is measured in initial geometry because the total Lagrangian formulation is adopted. If the updated Lagrangian formulation is used, then the element distortion could be measured based on the current geometry. The stress field could be calculated by using the same adjusting parameter. In other words, the stress at the specific point is obtained at the point by scaling the adjusting parameter. The geometry dependent Gauss integration could be interpreted as the use of the MITC method twice.

In the case of the MITC4+ shell element, the formulation is simplified by introducing a new assumed membrane strain field. First, the generalized assumed strain field is defined by using a variable '*k*' which determines the distance between tying points and the element center, and then the new assumed membrane strain field is obtained by taking zero to the distance. The resultant strain field does not include the bilinear strain coefficient and thus the formulation becomes much simpler than the previous MITC4+ shell element. The MITC4+ shell element shows excellent bending performance in both regular and distorted meshes but it reveals overly stiff in-plane bending behavior when the element is distorted.

To further improve the membrane performance of the MITC4+ shell element, the geometry dependent Gauss integration scheme is extended. When calculating the stiffness matrix of the MITC4+ shell element, the integration points in the *r*-*s* plane are modified in accordance with the element distortion to reduce the in-plane bending stiffness. Along the thickness direction, the standard Gauss quadrature is employed. The performance of the new MITC4+ shell element is demonstrated through selected problem sets including both geometrically linear and nonlinear analysis. While the bending performance of the new MITC4+ shell element is identical to the original MITC4+ and improved MITC4+ shell elements, the membrane performance of the proposed element is prior to the others.

In chapter 2, the new 2D-MITC4 solid finite element is proposed. The previous 2D-MITC4 element is briefly reviewed and then, the simplified assumed strain field for the new 2D-MITC4 element is presented. Also, for the improvement of the performance in distorted element, the geometry dependent Gauss integration scheme is introduced. Since there are various ways to adjust Gauss integration points, the practical requirements to design an adjusting parameter are proposed. In this thesis, the position of Gauss integration points is adjusted using the skewness of the element. The proposed element could be used for 2D plane stress and strain problems with the treatment of volumetric locking.

In the following section, the three basic tests including zero energy modes test, patch tests, and isotropy are conducted. Then, the performance of the proposed element is compared with other elements. The convergence behavior is studied for the linear problems including the cantilever beam, Cook's skew beam, the curved beam, and the block under a body force. For the nonlinear analysis, the displacements at specific points and numerical instabilities are studied in the block under a compression force and the column under an eccentric load.

In chapter 3, the new MITC4+ shell finite element is proposed. Since there is various version of the MITC4 element, the features are summarized first. we briefly review the formulation of the improved MITC4+ shell element including the treatment of the transverse shear and membrane locking. Then, the formulation of the new MITC4+ shell element is presented by extending the simplified assumed strain field and the geometry dependent Gauss integration into the previous MITC4+ shell element.

In the following section, the performance of the proposed shell elemenet is investigated in both linear and nonlinear problems. For the linear problems, the well-known behavior-encompassing shell benchmark problems are considered including square plate, cylindrical shell, hyperboloid shell, Scordelis-Lo roof, and hyperbolic cylinder shell. For the nonlinear problems, thin curved beam, slit annular plate, and hemispherical shell problems are solved.

In chapter 4, the conclusions and further studies are discussed.

Chapter 2. New 4-node quadrilateral solid finite element

Using the mixed interpolation of tensorial components (MITC) method, the 2D-MITC4 element has been recently developed for two-dimensional analysis of solids [30]. The element based on MITC method does not require additional DOFs, and no numerical instability is observed in nonlinear analysis [30-40]. Through various benchmark problems, the good convergence behavior of the 2D-MITC4 element in regular meshes is shown. However, its performance deteriorates when distorted meshes are used.

In this chapter, the convergence behavior of the 2D-MITC4 element in distorted meshes is improved. The two key points are the simplified formulation and the modified integration rule. The complicated assumed strain field of the original 2D-MITC4 element is simplified and thus its formulation becomes simpler and more straightforward. Also, a geometry dependent Gauss integration scheme is presented in which integration positions are adjusted according to element geometry, leading to an element insensitive to geometry distortion.

More specifically, the skewness of the element geometry is measured and integration positions are changed according to the degree of skewness. The larger the skewness, the more the integration positions move toward the center of the element, by use of an adjusting parameter. The practical requirements for the adjusting parameter are proposed with observations in the eigen analysis of the stiffness matrix depending on the different adjusting parameters. An adjusting parameter function to satisfy certain practical requirements is proposed using the degree of skewness.

The geometry dependent Gauss integration scheme is not only very easy to implement but also effective in the accuracy improvement of the original 2D-MITC4 element and can be directly extended to the nonlinear analysis without any modification in the formulation. Consequently, we develop the new 2D-MITC4 element for plane stress analysis and the new 2D-MITC4/1 element referring to the new 2D-MITC4 element in which volumetric locking is alleviated for plane stress and plane strain analysis.

In section 2.1, the basic formulations of the standard 4-node quadrilateral solid element [1-3] are briefly reviewed and the important expressions that are repeatably used throughout this paper are introduced including interpolations [1, 12], characteristic vectors [36], and physical strain coefficients [30]. In Section 2.2, the original 2D-MITC4 element is reviewed and the assumed strain field of the original 2D-MITC4 element is given [30]. Section 2.3 presents the key concepts of the proposed element and its formulation in detail. In the following section, the performance of the new 2D-MITC4 element is demonstrated through basic numerical tests, and several linear and nonlinear problems considering both regular and distorted meshes.

2.1. Geometry and displacement interpolations

As shown in Fig. 2.1, the geometry and displacement of the standard 4-node quadrilateral 2D solid element are interpolated by using the natural coordinates r and s as [1-3,12]

$$\mathbf{x}(r,s)=\sum_{i=1}^{4}h_i(r,s)\mathbf{x}_i \quad \text{with } \mathbf{x}_i=\begin{bmatrix}x_i & y_i\end{bmatrix}^T, \tag{2.1}$$

$$\mathbf{u}(r,s)=\sum_{i=1}^{4}h_i(r,s)\mathbf{u}_i \quad \text{with } \mathbf{u}_i=\begin{bmatrix}u_i & v_i\end{bmatrix}^T, \tag{2.2}$$

where $\mathbf{x}_i$ is the position vector of node i, $\mathbf{u}_i$ is the displacement vector of node i, and $h_i(r,s)$ is the two-dimensional shape function of the standard isoparametric procedure corresponding to node i which is given by

$$h_i=\frac{1}{4}(1+\xi_i r)(1+\eta_i s) \quad \text{with } i=1,2,3,4, \tag{2.3}$$

$$\begin{bmatrix}\xi_1 & \xi_2 & \xi_3 & \xi_4\end{bmatrix}=\begin{bmatrix}1 & -1 & -1 & 1\end{bmatrix}, \tag{2.4}$$

$$\begin{bmatrix}\eta_1 & \eta_2 & \eta_3 & \eta_4\end{bmatrix}=\begin{bmatrix}1 & 1 & -1 & -1\end{bmatrix}. \tag{2.5}$$

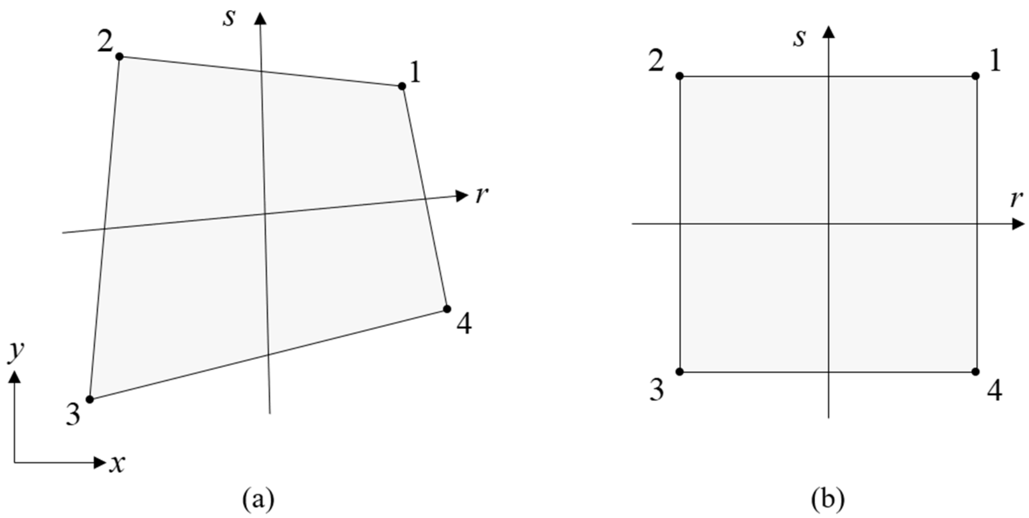

Fig. 2.1. A 4-node quadrilateral element in (a) the global Cartesian coordinate system and (b) the natural coordinate system.

The position and the displacement could be rewritten as

$$\mathbf{x}(r,s)=\mathbf{x}_a+r\mathbf{x}_r+s\mathbf{x}_s+rs\mathbf{x}_d, \tag{2.6}$$

$$\mathbf{u}(r,s)=\mathbf{u}_a+r\mathbf{u}_r+s\mathbf{u}_s+rs\mathbf{u}_d, \tag{2.7}$$

with characteristic geometry and displacement vectors as follows [30,36]:

$$\mathbf{x}_a=\frac{1}{4}\sum_{i=1}^{4}\mathbf{x}_i, \quad \mathbf{x}_r=\frac{1}{4}\sum_{i=1}^{4}\xi_i\mathbf{x}_i, \quad \mathbf{x}_s=\frac{1}{4}\sum_{i=1}^{4}\eta_i\mathbf{x}_i, \quad \mathbf{x}_d=\frac{1}{4}\sum_{i=1}^{4}\xi_i\eta_i\mathbf{x}_i, \tag{2.8}$$

$$\mathbf{u}_a = \frac{1}{4}\sum_{i=1}^{4}\mathbf{u}_i\ , \quad \mathbf{u}_r = \frac{1}{4}\sum_{i=1}^{4}\xi_i\mathbf{u}_i\ , \quad \mathbf{u}_s = \frac{1}{4}\sum_{i=1}^{4}\eta_i\mathbf{u}_i\ , \quad \mathbf{u}_d = \frac{1}{4}\sum_{i=1}^{4}\xi_i\eta_i\mathbf{u}_i\ , \tag{2.9}$$

where the vectors in Eq. (2.8) are determined from the nodal positions.

Note that the characteristic geometry vectors in Eq. (2.8) could be representative the geometry of the element as shown in Fig. 2.2. The vector $\mathbf{x}_a$ represents the center of the element and the two vectors $\mathbf{x}_r$ and $\mathbf{x}_s$ correspond with the covariant basis vectors. The vector $\mathbf{x}_d$ denotes the element distortion. The characteristic geometry and displacement vectors will be used to define physical strain patterns in the following section.

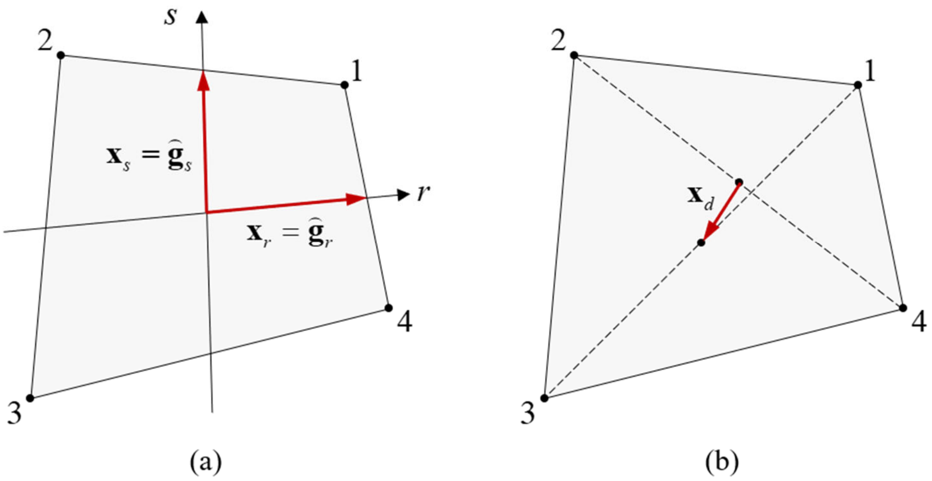

Fig. 2.2. Characteristic geometry vectors. (a) Two vectors $\mathbf{x}_r$ and $\mathbf{x}_s$ correspond to covariant base vectors at the element center. (b) The vector $\mathbf{x}_d$ denotes in-plane distortion.

The covariant base vectors and the derivatives of the displacements are obtained by [1, 30]

$$\mathbf{g}_r = \frac{\partial \mathbf{x}}{\partial r} = \mathbf{x}_r + s\mathbf{x}_d\ , \quad \mathbf{g}_s = \frac{\partial \mathbf{x}}{\partial s} = \mathbf{x}_s + r\mathbf{x}_d\ , \tag{2.10}$$

$$\mathbf{u}_{,r} = \frac{\partial \mathbf{u}}{\partial r} = \mathbf{u}_r + s\mathbf{u}_d\ , \quad \mathbf{u}_{,s} = \frac{\partial \mathbf{u}}{\partial s} = \mathbf{u}_s + r\mathbf{u}_d\ . \tag{2.11}$$

Note that the covariant base vectors in Eq. (2.10) become the characteristic vectors in Eq. (2.8) at the element center $(r = s = 0)$,

$$\mathbf{g}_r(0,0) = \mathbf{x}_r = \hat{\mathbf{g}}_r \quad \text{and} \quad \mathbf{g}_s(0,0) = \mathbf{x}_s = \hat{\mathbf{g}}_s\ . \tag{2.12}$$

The covariant strain components are defined by [33, 35]

$$\mathbf{e} = e_{ij}\left(\mathbf{g}^i \otimes \mathbf{g}^j\right) \quad \text{with} \quad e_{ij} = \frac{1}{2}\left(\mathbf{g}_i \cdot \mathbf{u}_{,j} + \mathbf{g}_j \cdot \mathbf{u}_{,i}\right),\ \ i, j = 1,2 \tag{2.13}$$

where the vector $\mathbf{g}^i$ is the contravariant base vector calculated by

$$\mathbf{g}^i \cdot \mathbf{g}_j = \delta^i_j \quad \text{with} \quad \mathbf{g}^1 = \mathbf{g}^r\ , \ \ \mathbf{g}^2 = \mathbf{g}^s\ , \ \ \mathbf{g}_1 = \mathbf{g}_r\ , \ \ \mathbf{g}_2 = \mathbf{g}_s\ . \tag{2.14}$$

Substituting Eqs. (2.10) and (2.11) into Eq. (2.13), the covariant strain components could be represented by using the characteristic vectors in Eqs. (2.8) and (2.9) as follows [36]:

$$e_{rr}\left(r,s\right)=e_{rr}\big|_{con}+s\cdot e_{rr}\big|_{lin}+s^2\cdot e_{rs}\big|_{bil}\ , \tag{2.15}$$

$$e_{ss}\left(r,s\right)=e_{ss}\big|_{con}+r\cdot e_{ss}\big|_{lin}+r^2\cdot e_{rs}\big|_{bil}\ , \tag{2.16}$$

$$e_{rs}\left(r,s\right)=e_{rs}\big|_{con}+r\cdot e_{rr}\big|_{lin}+s\cdot e_{ss}\big|_{lin}+rs\cdot e_{rs}\big|_{bil} \tag{2.17}$$

with

$$e_{rr}\big|_{con}=\mathbf{x}_r\cdot\mathbf{u}_r\ ,\ \ e_{rr}\big|_{lin}=\mathbf{x}_r\cdot\mathbf{u}_d+\mathbf{x}_d\cdot\mathbf{u}_r\ , \tag{2.18}$$

$$e_{ss}\big|_{con}=\mathbf{x}_s\cdot\mathbf{u}_s\ ,\ \ e_{ss}\big|_{lin}=\mathbf{x}_s\cdot\mathbf{u}_d+\mathbf{x}_d\cdot\mathbf{u}_s\ , \tag{2.19}$$

$$e_{rs}\big|_{con}=\frac{1}{2}\left(\mathbf{x}_r\cdot\mathbf{u}_s+\mathbf{x}_s\cdot\mathbf{u}_r\right),\ \ e_{rs}\big|_{bil}=\mathbf{x}_d\cdot\mathbf{u}_d\ , \tag{2.20}$$

in which the subscripts '*con*', '*lin*', and '*bil*' denote constant, linear, and bilinear terms of the strain components, respectively. The strain coefficients in Eqs. (2.18)-(2.20) are refered as 'physical strain coefficients' and they will be used to construct the assumed strain field. The physical strain coefficients in Eqs. (2.18)-(2.20) consist of physical strain patterns, see Appendix A for the details.

In vector and matrix forms, the displacement-based strain field in Eqs. (2.15)-(2.17) is transformed into the global Cartesian coordinates [1],

$$\varepsilon_{ij}=e_{kl}(\mathbf{i}_i\cdot\mathbf{g}^k)(\mathbf{i}_j\cdot\mathbf{g}^l)\ \text{ with }\ \mathbf{i}_1=\mathbf{i}_x\ \text{ and }\ \mathbf{i}_2=\mathbf{i}_y\ , \tag{2.21}$$

where $\mathbf{i}_i$ denotes the global Cartesian base vectors. Note that $\varepsilon_{11}=\varepsilon_{xx}$, $\varepsilon_{22}=\varepsilon_{yy}$ and $\varepsilon_{12}=\varepsilon_{xy}$. The relation between the strain components in Eq. (2.21) and the nodal displacement vector is expressed as

$$\mathbf{e}=\mathbf{B}\mathbf{U}\ \text{ with }\ \mathbf{e}=\begin{bmatrix}\varepsilon_{xx} & \varepsilon_{yy} & 2\varepsilon_{xy}\end{bmatrix}^{\mathrm{T}}\ \text{ and }\ \mathbf{U}=\begin{bmatrix}\mathbf{u}_1^{\mathrm{T}} & \mathbf{u}_2^{\mathrm{T}} & \mathbf{u}_3^{\mathrm{T}} & \mathbf{u}_4^{\mathrm{T}}\end{bmatrix}^{\mathrm{T}}, \tag{2.22}$$

where $\mathbf{B}$ is the strain-displacement matrix, and $\mathbf{U}$ is the nodal displacement vector.

The stiffness matrix of the 2D-MITC4 element is obtained as

$$\mathbf{K}=\int_{V_e}\mathbf{B}^{\mathrm{T}}\mathbf{C}\mathbf{B}\,dV_e\ , \tag{2.23}$$

where V_e is the element volume and $\mathbf{C}$ is the material law matrix [1], which is given by

$$\mathbf{C}=\frac{E}{1-\nu^2}\begin{bmatrix}1 & \nu & 0\\ \nu & 1 & 0\\ 0 & 0 & (1-\nu)/2\end{bmatrix}\ \text{ for plane stress problems,} \tag{2.24}$$

and

$$\mathbf{C}=\frac{E}{(1+\nu)(1-2\nu)}\begin{bmatrix}1-\nu & \nu & 0\\ \nu & 1-\nu & 0\\ 0 & 0 & 1/2-\nu\end{bmatrix}\ \text{ for plane strain problems,} \tag{2.25}$$

where E and ν are Young's modulus and Poisson's ratio, respectively.

2.2. Original 2D-MITC4 solid element

In this section, the assumed strain field for the original 2D-MITC4 element is reviewed [30] and then, the assumed strain field is rewritten with the physical strain coefficients in order to reduce computational cost.

2.2.1. Assumed strain field

In the original 2D-MITC4 elements, the assumed strain field is constructed for the following strain components

$$\hat{e}_{ij} = e_{kl} g_i^k g_j^l, \quad \mathbf{g}^i \cdot \hat{\mathbf{g}}_j = g_j^i, \tag{2.26}$$

where the vector $\hat{\mathbf{g}}_i$ is the constant base vector in Eq. (2.12).

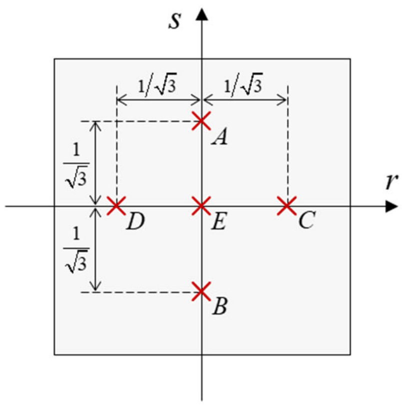

Fig. 2.3. Five tying points used to construct the assumed strain field of the original 2D-MITC4 element.

The original assumed strain fields employ the five tying points (*A*)-(*E*) as shown in Fig. 2.3. The center point E is used to represent the constant fields and the others are used to construct the linear fields as follows [30]:

$$\hat{e}_{rr}^{AS}(r,s) = \hat{e}_{rr}^{(E)} + \frac{\sqrt{3}}{2}\lambda(r,s)\, s\left(\hat{e}_{rr}^{(A)} - \hat{e}_{rr}^{(B)}\right), \tag{2.27}$$

$$\hat{e}_{ss}^{AS}(r,s) = \hat{e}_{ss}^{(E)} + \frac{\sqrt{3}}{2}\lambda(r,s)\, r\left(\hat{e}_{ss}^{(C)} - \hat{e}_{ss}^{(D)}\right), \tag{2.28}$$

$$\hat{e}_{rs}^{AS}(r,s) = \hat{e}_{rs}^{(E)}, \tag{2.29}$$

with $$\lambda(r,s) = \frac{\det(\mathbf{J}(0,0))}{\det(\mathbf{J}(r,s))}, \tag{2.30}$$

where $\mathbf{J}$ is the Jacobian matrix, and λ is the ratio of the determinants of the Jacobian matrices.

The strain components obtained at the center point are used to represent the constant strain behaviors and the strain components obtained at the others are used to construct the linear terms in Eqs. (2.18)-(2.19) for represent the bending behaviors. While the assumed strain fields in Eqs. (2.27)-(2.29) are closely related to the fields of the

QMITC element developed by Dvorkin and Vassolo [41], the assumed strain fields are differently constructed. Also, the 2D-MITC4 element uses only the 4 corner nodes to interpolate the geometry and displacement.

2.2.2. Formulation of the original 2D-MITC4 element

The assumed strain fields in Eqs. (2.27)-(2.29) could be computed at each Gauss integration points and thus it needs undesirable computational cost. In this section, the assumed strain fields are represented by the physical strain coefficients to reduce the computational cost because the physical strain coefficients could be pre-calculated at the element level [30].

To effectively calculate the strain field in Eqs. (2.27)-(2.29), the physical strain coefficients in Eqs. (2.18)-(2.20) are employed and then, the final formulation of the original 2D-MITC4 element is obtained as

$$\hat{e}_{rr}^{AS}(r,s) = e_{rr}\big|_{con} + \lambda(r,s)\, s\, \hat{e}_{rr}^{lin}, \tag{2.30}$$

$$\hat{e}_{ss}^{AS}(r,s) = e_{ss}\big|_{con} + \lambda(r,s)\, r\, \hat{e}_{ss}^{lin}, \tag{2.31}$$

$$\hat{e}_{rs}^{AS}(r,s) = e_{rs}\big|_{con}, \tag{2.32}$$

with

$$\hat{e}_{rr}^{lin} = \frac{n_1}{\sqrt{3}} e_{rs}\big|_{bil} + \sqrt{3}n_1\, e_{rr}\big|_{con} + \sqrt{3}n_2\, e_{ss}\big|_{con} + n_3\, e_{rr}\big|_{lin} + n_4\, e_{ss}\big|_{lin} + 2\sqrt{3}n_5\, e_{rs}\big|_{con}, \tag{2.33}$$

$$\hat{e}_{ss}^{lin} = \frac{m_1}{\sqrt{3}} e_{rs}\big|_{bil} + \sqrt{3}m_1\, e_{ss}\big|_{con} + \sqrt{3}m_2\, e_{rr}\big|_{con} + m_3\, e_{ss}\big|_{lin} + m_4\, e_{rr}\big|_{lin} + 2\sqrt{3}m_5\, e_{rs}\big|_{con}, \tag{2.34}$$

$$n_1 = \frac{1}{2}\left[\left(g_r^r\big|_{(A)}\right)^2 - \left(g_r^r\big|_{(B)}\right)^2\right],\ n_2 = \frac{1}{2}\left[\left(g_r^s\big|_{(A)}\right)^2 - \left(g_r^s\big|_{(B)}\right)^2\right],\ n_3 = \frac{1}{2}\left[\left(g_r^r\big|_{(A)}\right)^2 + \left(g_r^r\big|_{(B)}\right)^2\right], \tag{2.35}$$

$$n_4 = \frac{1}{2}\left[g_r^r\big|_{(A)} \cdot g_r^s\big|_{(A)} + g_r^r\big|_{(B)} \cdot g_r^s\big|_{(B)}\right],\ n_5 = \frac{1}{2}\left[g_r^r\big|_{(A)} \cdot g_r^s\big|_{(A)} - g_r^r\big|_{(B)} \cdot g_r^s\big|_{(B)}\right], \tag{2.36}$$

$$m_1 = \frac{1}{2}\left[\left(g_s^s\big|_{(C)}\right)^2 - \left(g_s^s\big|_{(D)}\right)^2\right],\ m_2 = \frac{1}{2}\left[\left(g_s^r\big|_{(C)}\right)^2 - \left(g_s^r\big|_{(D)}\right)^2\right],\ m_3 = \frac{1}{2}\left[\left(g_s^s\big|_{(C)}\right)^2 + \left(g_s^s\big|_{(D)}\right)^2\right], \tag{2.37}$$

$$m_4 = \frac{1}{2}\left[g_s^r\big|_{(C)} \cdot g_s^s\big|_{(C)} + g_s^r\big|_{(D)} \cdot g_s^s\big|_{(D)}\right],\ m_5 = \frac{1}{2}\left[g_s^r\big|_{(C)} \cdot g_s^s\big|_{(C)} - g_s^r\big|_{(D)} \cdot g_s^s\big|_{(D)}\right], \tag{2.38}$$

in which $g_i^j\big|_{(\bullet)}$ is g_i^j evaluated at a tying point $(\bullet)$. Note that the original assumed strain fields consist of the complicated combination of the strain coefficients.

Note that the linear terms in Eqs. (2.31)-(2.31) consist of six physical strain coefficients and ten additional coefficients. The physical strain coefficients and additional coefficients could be calculated by using the characteristic vectors at the element level before evaluating the stiffness matrix.

2.2.3. Treatment of the volumetric locking

To alleviate volumetric locking in the plane strain analysis of structures with nearly incompressible materials, it is effective to use the constant volumetric strain [1, 12], which also could enhance the performance of the element in plane stress analysis [30].

The assumed strain fields in Eqs. (2.30)-(2.32) are decomposed into volumetric and deviatoric parts as follows:

$$ {}^{vol}\bar{e} = \bar{e}_{xx}^{AS}\left(0,0\right) + \bar{e}_{yy}^{AS}\left(0,0\right) = {}^{vol}\bar{\mathbf{B}}\mathbf{U} \,, \tag{2.39} $$

$$ {}^{dev}\bar{e}_{ij} = \bar{e}_{ij}^{AS} - \frac{1}{2}\,{}^{vol}\bar{e}\,\delta_{ij} = {}^{dev}\bar{\mathbf{B}}_{ij}\mathbf{U} \quad \text{with} \quad \mathbf{U} = \left[\mathbf{u}_1 \;\, \mathbf{u}_2 \;\, \mathbf{u}_3 \;\, \mathbf{u}_4\right]^T , \tag{2.40} $$

where the overbar indicates that the value is in the global Cartesian coordinates, $\mathbf{B}$ is the strain-displacement matrix, and $\mathbf{U}$ is the nodal displacement vector. The constant volumetric strain in Eq. (2.39) is obtained from strain components at the element center.

Then, the element stiffness matrix of the improved 2D-MITC4 element could be obtained as

$$ \mathbf{K} = \int_{V_e} \left(\kappa + \frac{\mu}{3}G\right) {}^{vol}\bar{\mathbf{B}}^T\, {}^{vol}\bar{\mathbf{B}}\, dV_e + \int_{V_e} {}^{dev}\bar{\mathbf{B}}_{ij}^T C_{ij}^{dev}\, {}^{dev}\bar{\mathbf{B}}_{ij} dV_e \tag{2.41} $$

where $\mu = \frac{(1+\nu)(1-4\nu)}{(1-\nu)(1-2\nu)}$ for the plane stress analysis, $\mu = 1$ for the plane strain analysis, t, κ, G, and ν are the thickness, bulk modulus, shear modulus, and Poisson's ratio, respectively, and C_{ij}^{dev} denotes the material tensor for the deviatoric strain and stress ($C_{11}^{dev} = C_{22}^{dev} = 2G$ and $C_{12}^{dev} = G$).

2.3. New 2D-MITC4 solid element

In this section, the formulation of the new 4-node quadrilateral solid finite element (improved 2D-MITC4 element) is presented in detail. We derive a new assumed strain field for the element and present a numerical scheme to adjust Gauss integration points to enhance its bending behavior when the element is distorted. We also present the well-known scheme to alleviate volumetric locking that can be incorporated with the improved 2D-MITC4 elements.

2.3.1. Simplified assumed strain field

The strain components at each tying point are represented using the characteristic geometry and displacement vectors in Eqs. (2.8)-(2.9), and the resulting equations are substituted into Eqs. (2.30)-(2.32); the assumed strain field can be rewritten as

$$\hat{e}_{rr}^{AS}(r,s) = \mathbf{x}_r \cdot \mathbf{u}_r + \frac{3\lambda(r,s)}{3-\alpha^2}\left(-\alpha \mathbf{x}_r \cdot \mathbf{u}_r - \beta \mathbf{x}_r \cdot \mathbf{u}_s + \mathbf{x}_r \cdot \mathbf{u}_d\right)s \,, \tag{2.42}$$

$$\hat{e}_{ss}^{AS}(r,s) = \mathbf{x}_s \cdot \mathbf{u}_s + \frac{3\lambda(r,s)}{3-\beta^2}\left(-\beta \mathbf{x}_s \cdot \mathbf{u}_s - \alpha \mathbf{x}_s \cdot \mathbf{u}_r + \mathbf{x}_s \cdot \mathbf{u}_d\right)r \,, \tag{2.43}$$

$$\hat{e}_{rs}^{AS}(r,s) = \frac{1}{2}\left(\mathbf{x}_r \cdot \mathbf{u}_s + \mathbf{x}_s \cdot \mathbf{u}_r\right), \tag{2.44}$$

with $\alpha = \mathbf{x}_d \cdot \hat{\mathbf{g}}^r$ and $\beta = \mathbf{x}_d \cdot \hat{\mathbf{g}}^s$, (2.45)

where the vectors $\hat{\mathbf{g}}^r$ and $\hat{\mathbf{g}}^s$ are the contravariant base vectors evaluated at the element center with $\hat{\mathbf{g}}^r = \mathbf{g}^r(0,0)$ and $\hat{\mathbf{g}}^s = \mathbf{g}^s(0,0)$ as in Eq. (2.12).

The simplified assumed strain field in Eqs. (2.42)-(2.44) directly consists of the characteristic vectors. This assumed strain field has a much simpler form than that of the original assumed strain field, which consists of the strain coefficients in Eqs. (2.18)-(2.20).

2.3.2. Classification of distortion

The geometry distortion of a 4-node quadrilateral element can be expressed by the aspect ratio, skewness, and taper [4, 42]. It is interesting to note that the geometry distortion due to skewness and taper can be represented using three characteristic vectors, $\mathbf{x}_r$, $\mathbf{x}_s$, and $\mathbf{x}_d$ as shown in Fig. 2.4(a).

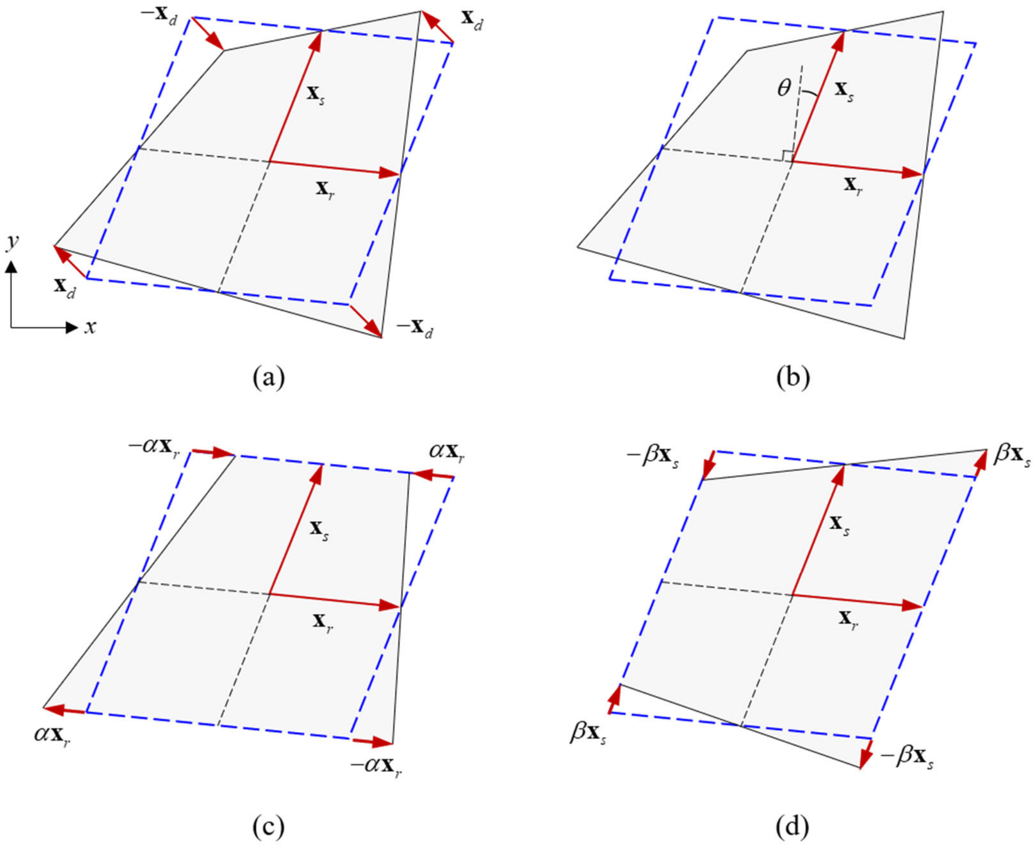

Fig. 2.4. Classification of distortion for 4-node quadrilateral element. (a) Characteristic vectors, (b) skewness, (c) taper in r-direction, and (d) taper in s-direction.

Using the two vectors $\mathbf{x}_r$ and $\mathbf{x}_s$, a parallelogram with blue dashed line can be constructed as shown in Fig. 2.4 (b). The skewness can be measured by angle θ and the skew angle is calculated as

$$\cos\theta = \frac{1}{|\hat{\mathbf{g}}_r||\hat{\mathbf{g}}^r|} = \frac{1}{|\hat{\mathbf{g}}_s||\hat{\mathbf{g}}^s|}. \tag{2.46}$$

In addition, the characteristic vector $\mathbf{x}_d$ representing the taper can be measured by α and β in Eq. (2.45).

$$\mathbf{x}_d = \alpha\mathbf{x}_r + \beta\mathbf{x}_s, \tag{2.47}$$

where α and β denote the tapers in the r - and s - directions, respectively; see Fig. 2.4(c) and (d).

2.3.3. Geometry dependent Gauss integration

It is well known that the performance of finite elements can be improved by modifying the integration rule [17-20, 43-45]. In most previous studies, a fixed integration rule was adopted without concern for element geometry. We here introduce a numerical scheme to adaptively adjust Gauss integration points according to the degree of element distortion to make the element performance less sensitive to its geometry distortion.

When evaluating the stiffness matrix, the standard 2×2 Gauss integration in Fig. 2.5(a) is employed in general

$$\mathbf{K} = t\sum_{i=1}^{2}\sum_{j=1}^{2} w_i w_j \mathbf{F}\left(\zeta_i, \zeta_j\right) \text{ with } \zeta_1 = 1/\sqrt{3}\,,\ \zeta_2 = -1/\sqrt{3}\,,\ w_1 = w_2 = 1\,, \tag{2.48}$$

in which t is the element thickness, and ζ_i and w_i denote the integration positions and the corresponding weight factors for the two-point Gauss integration, respectively.

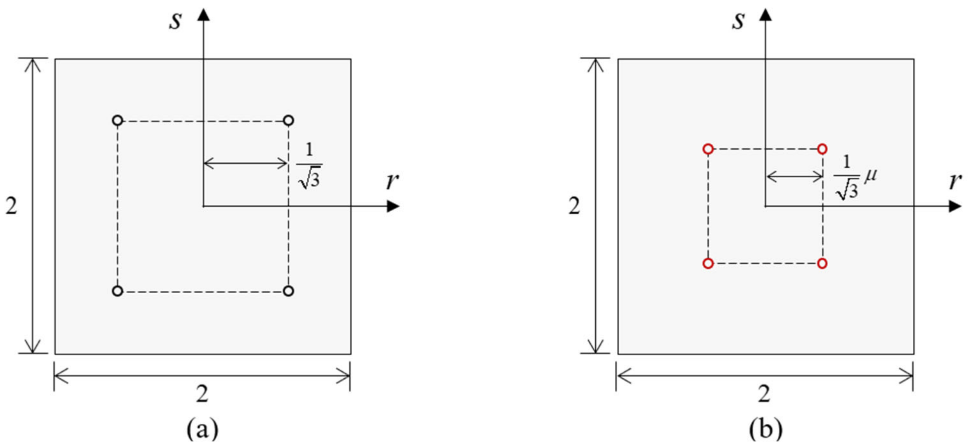

Fig. 2.5. Integration points for (a) standard Gauss integration and (b) geometry dependent Gauss integration.

In Eq. (2.48),

$$\mathbf{F}(r,s) = \mathbf{B}^{\mathrm{T}}\mathbf{C}\mathbf{B}\det(\mathbf{J}) \quad \text{for the 2D-MITC4 element,} \tag{2.49}$$

and

$$\mathbf{F}(r,s) = \left[\left(\kappa + \frac{\eta}{3}G\right){}^{vol}\mathbf{B}^{\mathrm{T}}\,{}^{vol}\mathbf{B} + {}^{dev}\mathbf{B}_{ij}^{\mathrm{T}} C_{ij}^{dev}\,{}^{dev}\mathbf{B}_{ij}\right]\det(\mathbf{J}) \text{ for the 2D-MITC4/1 element.} \tag{2.50}$$

With this standard integration rule, the original 2D-MITC4 and MITC4/1 elements reveal overly stiff bending behavior when the element is distorted. There are many ways to modify the position of Gauss integration points, see Appendix B.This stiffening effect arising with geometry distortion can be alleviated by moving the integration points toward the element center as

$$\mathbf{K} \approx t\sum_{i=1}^{2}\sum_{i=1}^{2} w_i w_j \mathbf{F}\left(\hat{\zeta}_i, \hat{\zeta}_j\right) \text{ with } \hat{\zeta}_i = \mu\zeta_i\,, \tag{2.51}$$

where μ is an adjusting parameter smaller than 1.0, as shown in Fig. 2.5(b).

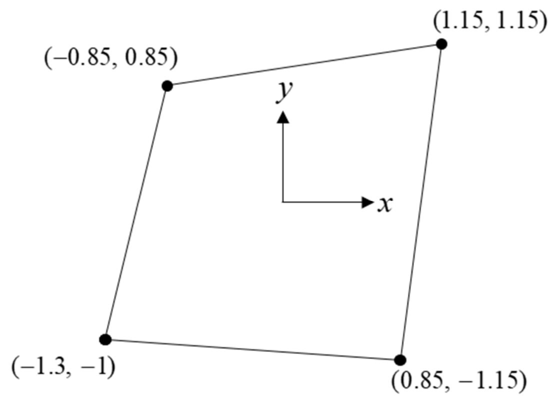

Fig. 2.6. Distorted element for eigenvalue analysis.

To show that adjusted integration points can alleviate overly stiff bending behavior of the distorted element, the eigen analysis of the stiffness matrix of a single 2D-MITC4 element shown in Fig. 2.6 is carried out. The plane stress condition is considered with Poisson's ratio $\nu = 0.3$.

Table 2.1 shows eigenvalues normalized by Young's modulus according to the adjusting parameter μ . The standard 2x2 Gauss integration is applied with the parameter $\mu = 1$. The case of $\mu = 0$ corresponds to the reduced integration, for which the eigenvalues for the two bending modes become zero and thus spurious zero energy modes occur.

Table 2.1. Normalized eigenvalues of stiffness matrix of single 2D-MITC4 element according to adjusting parameter μ . The original 2D-MITC4 element corresponds to $\mu = 1$. The eigenvalues are normalized by Young's modulus.

Mode		$\mu = 1$	$\mu = 0.5$	$\mu = 0.1$	$\mu = 0$
1	Rigid body modes	0	0	0	0
2		0	0	0	0
3		0	0	0	0
4	Bending modes	0.3094	0.0773	0.0031	0
5		0.4740	0.1198	0.0048	0
6	Constant strain modes	0.7205	0.7173	0.7169	0.7168
7		0.7976	0.7886	0.7875	0.7874
8		1.5374	1.5339	1.5330	1.5330

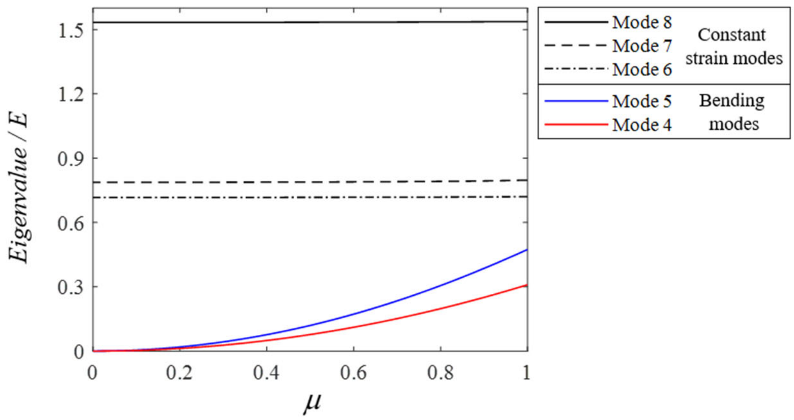

Fig. 2.7. Change in normalized eigenvalues of each deformation mode according to adjusting parameter μ .

Fig. 2.7 show the normalized eigenvalues of each deformation mode according to the adjusting parameter. The eigenvalues for the constant strain modes (modes 6, 7 and 8) are almost unaffected, but the eigenvalues corresponding to the bending modes (modes 4 and 5) rapidly decrease as the adjusting parameter become smaller. Therefore, it is possible to adaptively reduce the element bending stiffness by changing the integration points.

With this observation, we propose the following practical requirements to design a function $\mu = f(\mathbf{x}_1, \mathbf{x}_2, \mathbf{x}_3, \mathbf{x}_4)$ for the adjusting parameter.

- $\mu = 1$ for undistorted element geometries (Standard Gauss integration is used.)
- $\mu \leq 1$ when element geometry is distorted
- No spurious zero energy mode: $\mu > 0$
- Ideally optimal convergence for bending problems
- Same value for quadrilaterals in similarity: $\mu_{\square ABCD} = \mu_{\square EFGH}$ when $\square ABCD \sim \square EFGH$

A number of functions for the adjusting parameter satisfying the above requirements can be devised, and we here propose the following function

$$\mu = \cos^2(\theta) = \frac{1}{|\hat{\mathbf{g}}_r|^2 |\hat{\mathbf{g}}^r|^2} = \frac{1}{|\hat{\mathbf{g}}_s|^2 |\hat{\mathbf{g}}^s|^2}, \tag{2.52}$$

in which θ denotes the skew angle defined in Eq. (2.46). Fig. 2.8 shows the relationship between the adjusting parameter μ and the skew angle θ as shown in Fig. 2.9. For the details, see Appendix C.

The same adjusting parameter is also employed to calculate strain and stress. Strain at (r', s') is calculated by entering $(\mu r', \mu s')$ into Eqs. (2.22), (2.39) and (2.40) instead of (r', s'), and the corresponding stress is obtained through the material law.

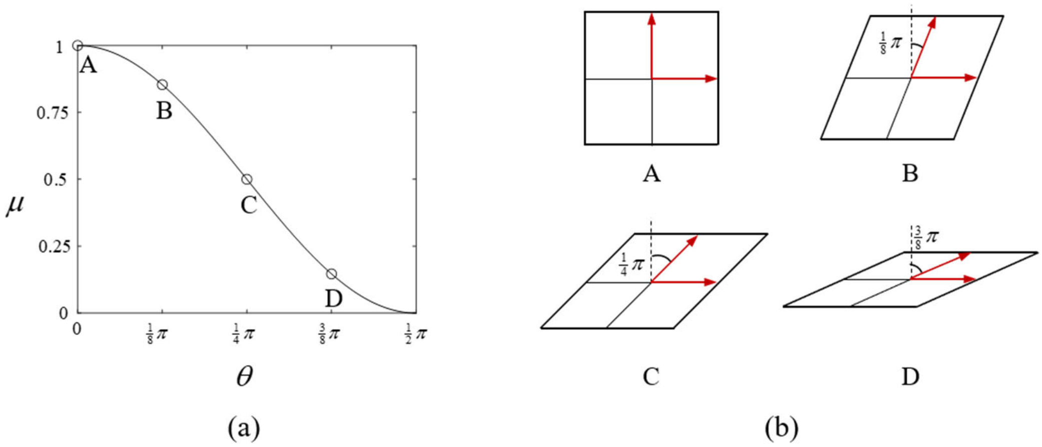

Fig. 2.8. Adjusting parameter and skew angle. (a) Adjusting parameter according to the skew angle. (b) Element geometries with skew angles $\theta = 0$, $\pi/8$, $\pi/4$, and $3\pi/8$.

In this study, the total Lagrangian formulation is employed for geometric nonlinear analysis and thus the adjusting parameter is obtained from the initial element geometry. If the updated Lagrangian formulation is adopted, the adjusting parameter could be updated.

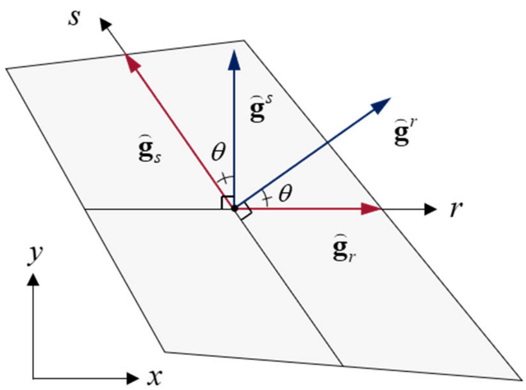

Fig. 2.9. The distortion angle θ corresponding to the angle between covariant and contravaiant base vectors at the element center. The distortion angle satisfies the above proposed requirements.

In the following section, it was confirmed that the improved 2D-MITC4 element passed all basic numerical tests including patch, isotrophy, and zero energy mode tests. Throughout various numerical examples, the improved 2D-MITC4 element shows better predictive capabilities especially in distorted meshes. The convergences in the strain energy and the displacements at specific node are studied and the improved 2D-MITC4 element shows almost optimal convergences in both regular and distorted meshes. The improved 2D-MITC4 element also provides more accurate results without showing any spurious instabilities in geomatrically nonlinear analayses.

2.4. Basic numerical tests

In this section, we perform three basic numerical tests (patch, zero energy mode, and isotropy tests) for the improved 2D-MITC4 element.

In order to check the consistency of the element, the normal and shear patch tests are carried out using the mesh shown in Fig. 2.10 [1,12]. The minimum number of fixed boundary conditions are given to suppress the rigid body motions. For both normal and shear patch tests using the improved 2D-MITC4 element, the constant stress fields are obtained which are identical to the analytical solutions.

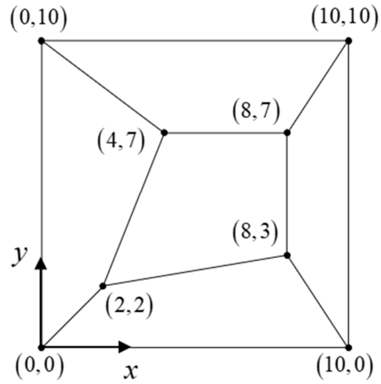

Fig. 2.10. Mesh pattern used for the patch tests.

In the zero energy mode test, a single 2D element without support should have only three zero energy modes corresponding to the rigid body modes which consist of two translations and one rotation [1-3]. The improved 2D-MITC4 element passes the zero energy mode test considering the geometry in Fig. 2.11.

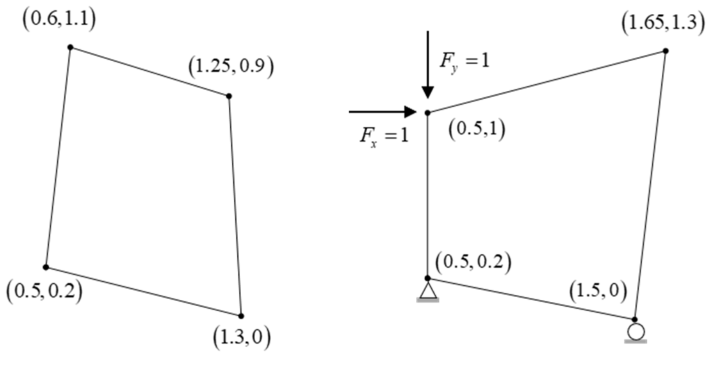

Fig. 2.11. Geometries for zero energy mode and isotropy tests.

All the elements in FEM should be spatially isotropic since the performance of an element should not be affected by the node numbering sequence [1,33]. Considering geometry in Fig. 2.11, The improved 2D-MITC4 element passes the isotropy test.

2.5. Numerical examples for linear analysis

In this section, to demonstrate the performance of the improved 2D-MITC4 element, we solve several numerical examples: a cantilever problem, a cantilever beam with distortion parameter, Cook's skew beam, a thick curved beam, and a block subjected to complex forces. The first two problems are considered to compare the diaplacement and stress with analytic solutions. The next two problems are considered to study convergences in strain energy and displacements. The stress contours are given in the problems. The last problems are considered with plane strain assumption to check the alleviation of the volumetric locking. The standard 4-node quadrilateral element (Q4), the original 2D-MITC4 element (2D-MITC4), the incompatible modes element (ICM-Q4) are considered for comparison with the improved 2D-MITC4 element (improved) [27,30].

To show the enhanced predictive capability of the improved 2D-MITC4 element in detail, we check the displacements and stresses at specific locations [1,12,30]. In addition, the convergence of the relative error in strain energy E_r is employed,

$$E_r = \frac{\left|E_{ref} - E_h\right|}{E_{ref}}, \tag{2.52}$$

where E_{ref} and E_h are the strain energies stored in the whole structure calculated from the reference and finite element solutions, respectively. The optimal convergence of the 4-node element for the relative error in strain energy is obtained as $E_r \cong ch^2$, where c is a constant and h denotes the element size. The reference solutions are either analytical solutions or sufficiently converged solutions obtained using 9-node quadrilateral solid element.

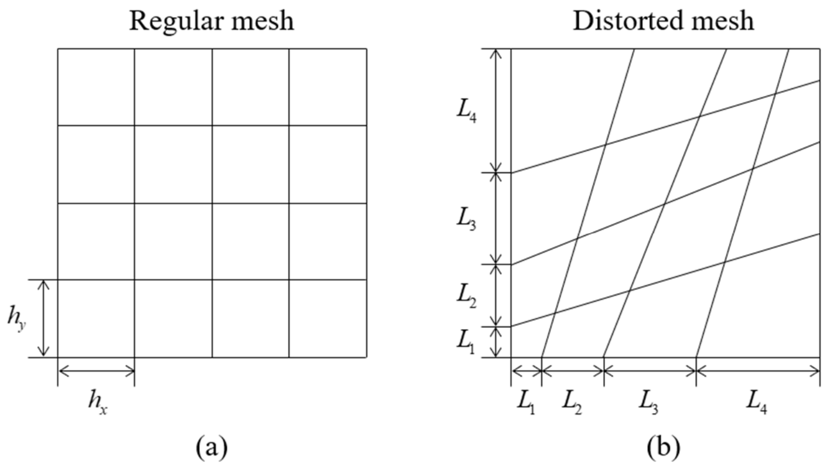

Fig. 2.12. Mesh patterns used to numerical problems. (a) Regular and (b) distorted mesh patterns when $N = 4$.

To generate the $N \times N$ regular and distorted meshes for the finite element models, the mesh patterns are first constructed in a square domain shown in Fig. 2.12 and then, linearly mapped to a problem domain under consideration [1,12]. In the distorted mesh pattern, each edge has been divided into the following ratio: $L_1 : L_2 : L_3 : \ldots\ldots L_N = 1:2:3:\ldots\ldots N$ for the $N \times N$ mesh.

2.5.1. Cantilever problem

We solve the cantilever beam subjected to a shearing force $P = 40$ at its end tip as shown in Fig. 2.13 [46-48]. The plane stress condition is considered with Young's modulus $E = 3\times10^4$ and Poisson's ratio $\nu = 0$. The cantilever beam is modeled using four elements in regular and distorted meshes.

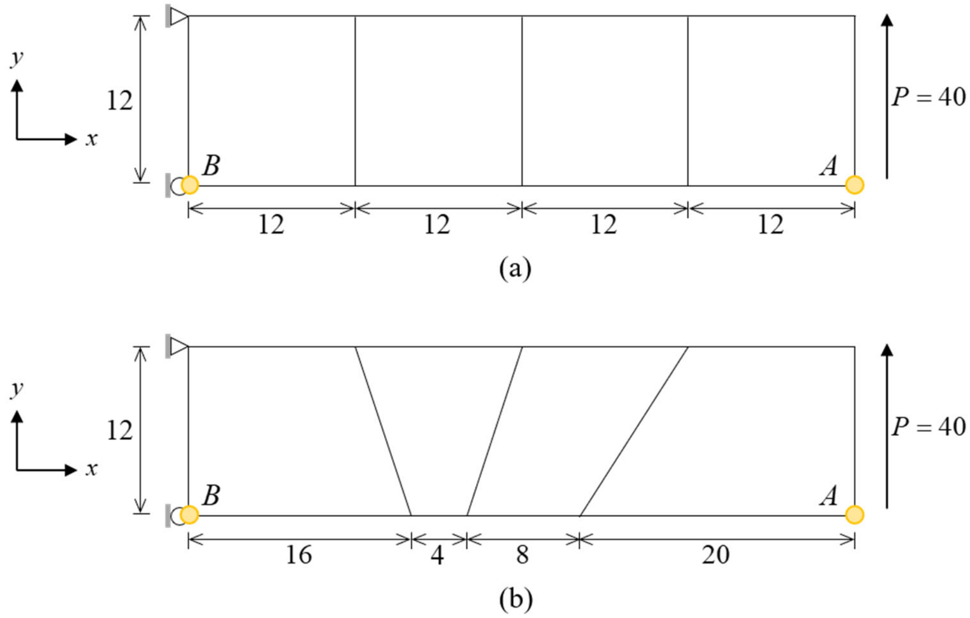

Fig. 2.13. Cantilever problem ($E = 3\times10^4$ and $\nu = 0$). (a) regular mesh. (b) distorted mesh.

Table 2.2. Relative errors in the tip displacement ($\left|v_{ref} - v_h\right| / v_{ref} \times 100$) at point A in the cantilever problem.

Elements	Regular mesh	Distorted mesh
Q4	32.26%	41.36%
ICM-Q4	0%	1.51%
2D-MITC4	0%	13.14%
Improved	0%	1.42%
Reference solution: $v_{ref} = 0.34781$		

Table 2.3. Relative errors in the *xx*-component of stress ($\left|\sigma_{ref} - \sigma_{xx/h}\right| / \sigma_{ref} \times 100$) at the support point B in the cantilever problem.

Elements	Regular mesh	Distorted mesh
Q4	33.33%	49.80%
ICM-Q4	0%	12.07%
2D-MITC4	0%	17.03%
Improved	0%	12.04%
Reference solution: $\sigma_{ref} = 70$		

The relative errors in the vertical displacement at point A and the xx-component of stress at point B for both regular and distorted meshes are listed in Table 2.2 and Table 2.3, respectively. For regular mesh, the ICM-Q4 and both the original and improved 2D-MITC4 elements give the exact solution. For the distorted mesh, the improved 2D-MITC4 element gives the most accurate solution.

2.5.2. Cantilever beam with distortion parameter

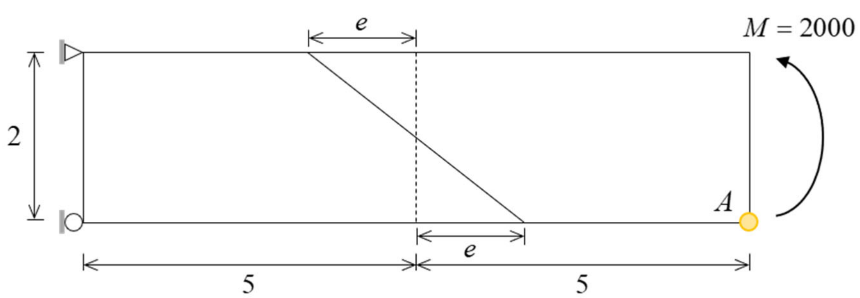

Fig. 2.14. Cantilever beam (*E*=1500 and *ν*=0.25) modeled using two elements with distortion parameter (*e*).

To further test the sensitivity to the mesh distortion, the cantilever beam modeled by using two elements with a distortion parameter is considered as shown in Fig. 2.14 [5,49]. The plane stress condition is considered with Young's modulus $E = 1500$ and Poisson's ratio $\nu = 0.25$. The left end is fixed and a bending moment $M = 2000$ is applied at the right end.

The shapes of the elements are symmetrically changed with respect to the distortion parameter, e, which indicates the degree of element distortion. As the distortion parameter e changes from 0 to 4.9, the element distortion becomes more severe. The normalized vertical displacement at point A is shown in Fig. 2.15. The result shows that the improved 2D-MITC4 element is least affected by element distortion.

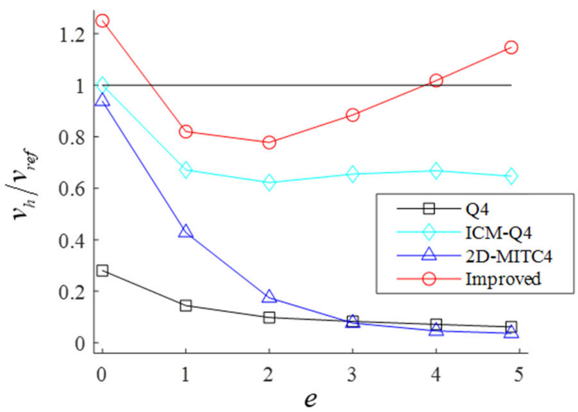

Fig. 2.15. Normalized vertical displacements (v_h/v_{ref}) at point A according to the distortion parameter (e).

2.5.3. Cook's skew beam

The well-known Cook's skew beam problem is considered as shown in Fig. 2.16 [12,21]. The left end of the structure is fixed, and a distributed shearing force $f_s = 1/16$ (force per length) is applied at the right end. We use the plane stress condition with Young's modulus $E = 1$ and Poisson's ratio $\nu = 1/3$. The solutions for both regular and distorted meshes are obtained with $N \times N$ meshes (N = 2, 4, 8, and 16). The distorted mesh patterns used for the problem are depicted in Fig. 2.16(b).

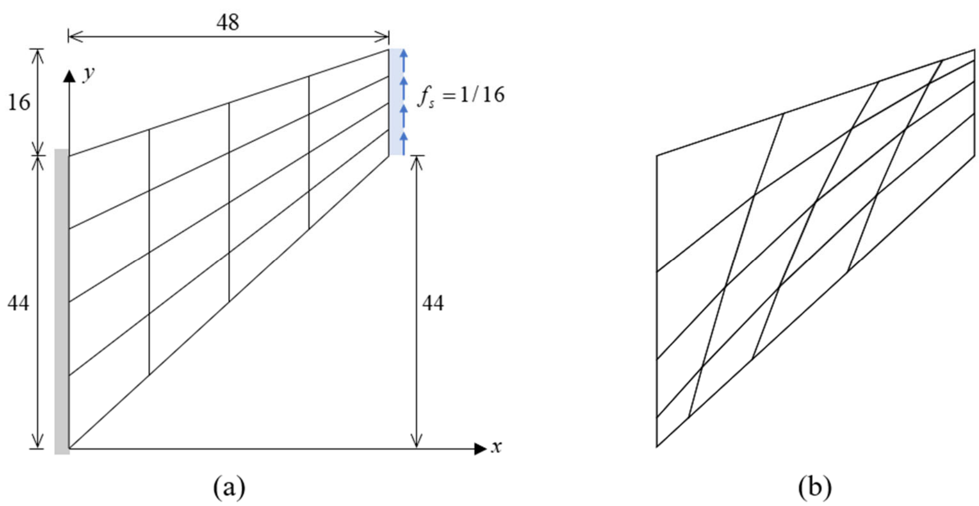

Fig. 2.16. Cook's skew beam ($E = 1$ and $\nu = 1/3$). (a) Regular mesh when $N = 4$. (b) Distorted mesh when $N = 4$.

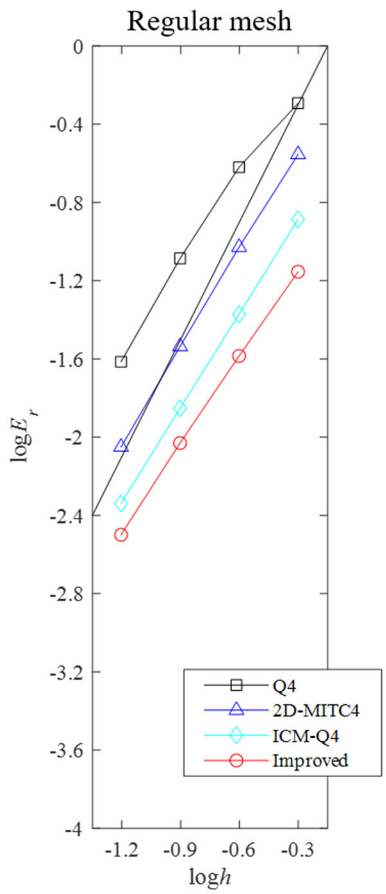

Fig. 2.17. Convergence curves for Cook's skew beam. The bold line represents the optimal convergence rate.

The convergences of the normalized vertical and horizontal displacements at point A are shown in Fig. 2.18 and Fig. 2.19, respectively. The convergence curves of the relative error according to the element size $h = 1/N$ are shown in Fig. 2.17. The reference solutions for displacements and strain energy are obtained by using a 64×64 mesh of 9-node quadrilateral element. The improved 2D-MITC4 element gives much more accurate results than the original 2D-MITC4 element and gives not much less accurate results than the ICM-Q4 element.

The relative errors in the vertical and horizontal dilaplacement at point A are given in Table 2.4 and Table 2.5, repectivley. The shear stress (σ_{xy}) distributions calculated in Cook's skew beam are also illustrated in Fig. 2.20 considering distorted meshes with $N = 8$. The reference shear stress distribution is obtained using a 64×64 mesh of 9-node quadrilateral elements. The results show the improved 2D-MITC4 element provides more accurate solutions in both regular and distorted meshes.

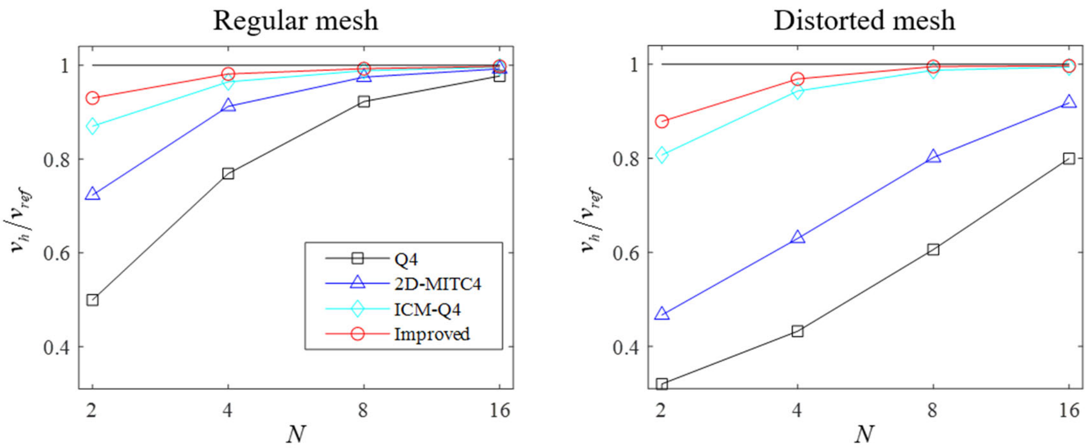

Fig. 2.18. Normalized vertical displacements (v_h/v_{ref}) at point A in Cook's skew beam.

Table 2.4 Relative errors in the vertical displacement ($|v_{ref}-v_h|/v_{ref}\times 100$) at point A in Cook's skew beam.

mesh	N	Q4	2D-MITC4	ICM-Q4	Improved
Regular	2	50.05517	27.68639	13.0034	6.999521
	4	23.10617	8.787242	3.552471	1.868016
	8	7.746865	2.547952	1.169934	0.74256
	16	2.311595	0.774109	0.384576	0.255881
Distorted	2	67.99257	53.31366	19.29182	12.16736
	4	56.77213	37.04392	5.68947	3.130528
	8	39.40818	19.82833	1.284105	0.481765
	16	20.05244	8.22445	0.578696	0.341865
Reference solution: $v_{ref}=23.2022$					

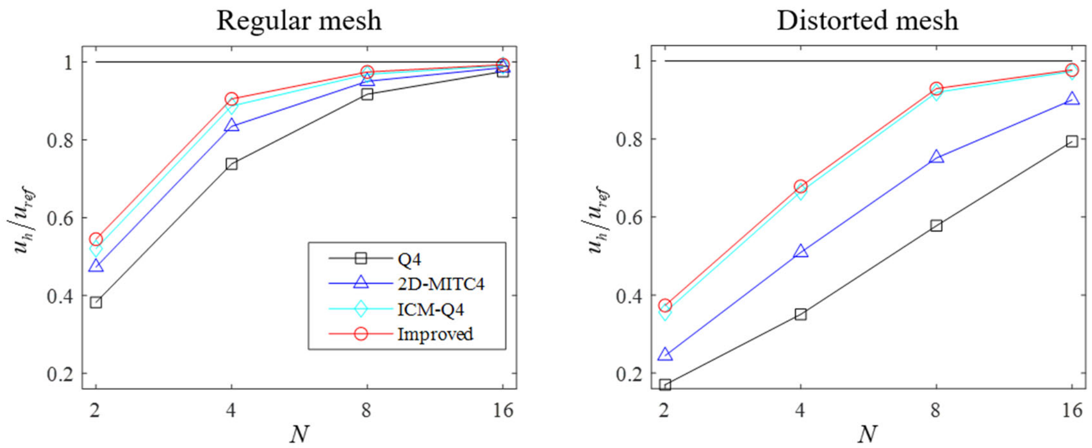

Fig. 2.19. Normalized horizontal displacements (u_h/u_{ref}) at point A in Cook's skew beam.

Table 2.5 Relative errors in the horizontal displacement ($|u_{ref} - u_h| / u_{ref} \times 100$) at point A in Cook's skew beam.

mesh	N	Q4	2D-MITC4	ICM-Q4	Improved
Regular	2	61.78692	52.71882	47.97745	45.54151
	4	26.18252	16.54475	11.30688	9.486452
	8	8.279696	4.95076	3.173436	2.560279
	16	2.450948	1.445494	0.901428	0.710326
Distorted	2	82.9852	75.53294	64.39452	62.65732
	4	64.92443	49.04938	33.49812	32.12622
	8	42.23079	24.85272	8.046069	7.06453
	16	20.6159	9.969728	2.638708	2.281475

Reference solution: $u_{ref} = -4.6373$

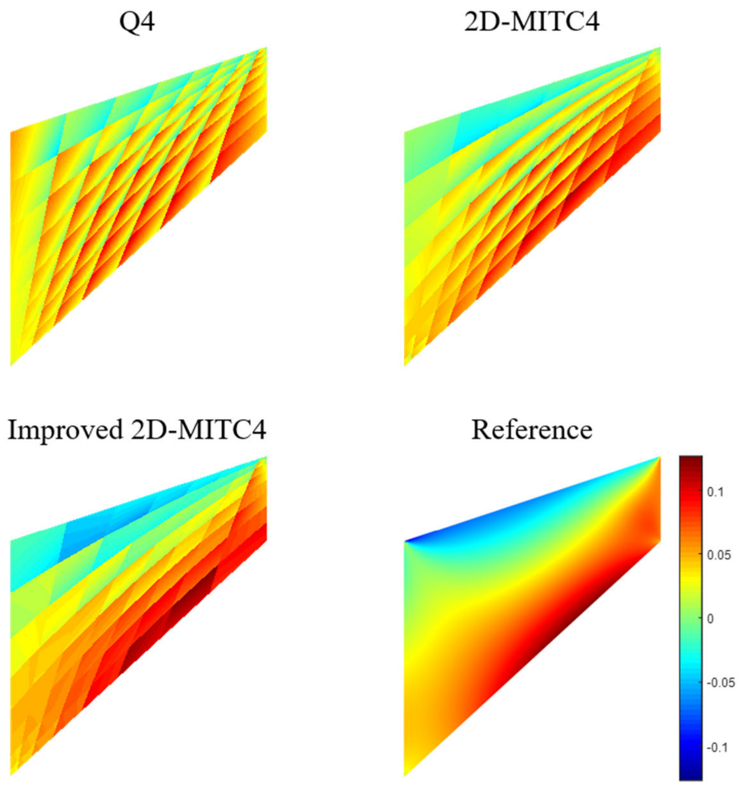

Fig. 2.20. Shear stress (σ_{xy}) distributions calculated in Cook's skew beam using distorted meshes with $N = 8$. The reference stress distribution is obtained using a 64×64 mesh of 9-node quadrilateral elements.

2.5.4. Curved beam

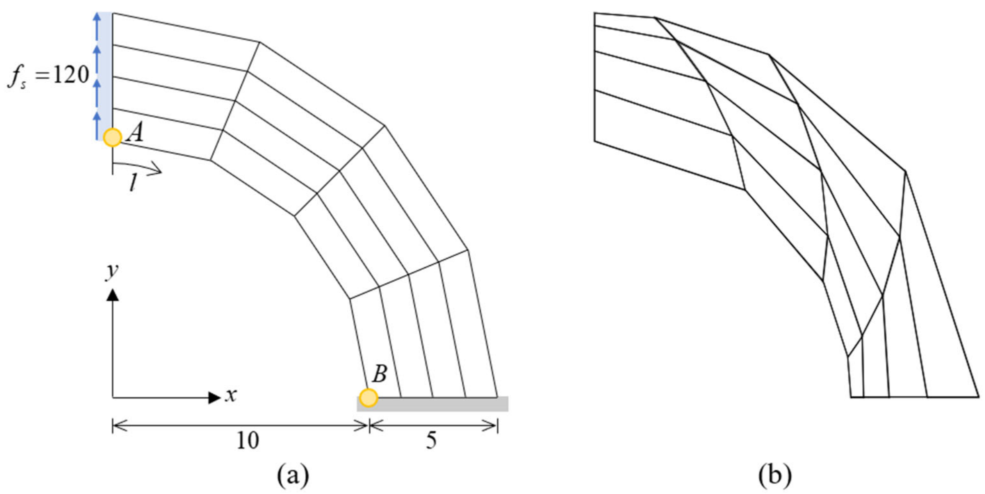

Fig. 2.21. Curved beam ($E = 1\times 10^3$ and $\nu = 0$). (a) 4×4 regular mesh, (b) 4×4 distorted mesh.

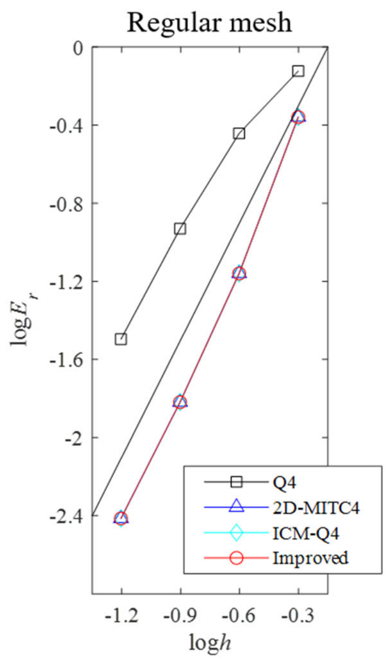

Fig. 2.22. Convergence curves for the curved beam. The bold line denotes the optimal convergence rate.

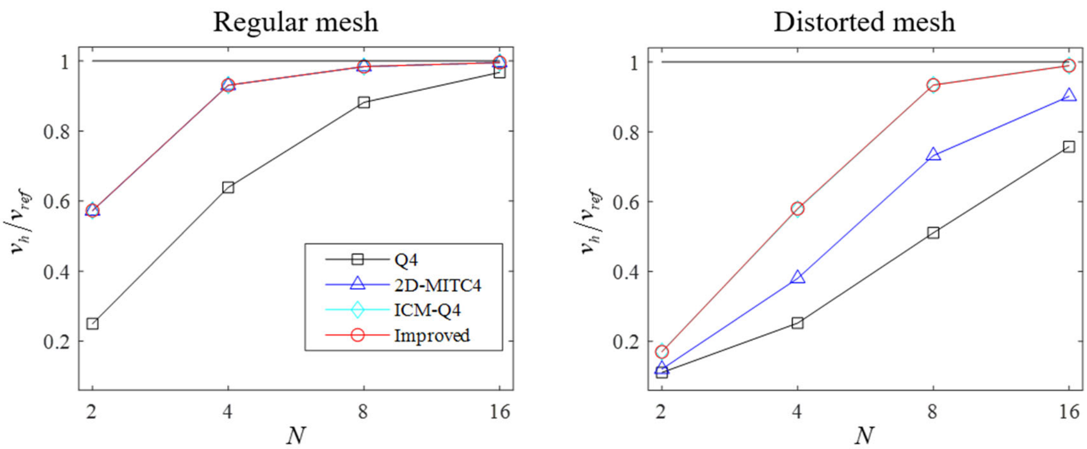

Fig. 2.23. Normalized vertical displacements (v_h/v_{ref}) at point A in the curved beam.

We consider the curved beam problem as shown in Fig. 2.21. The curved beam is clamped at the bottom and subjected to a distributed shearing force $f_s = 120$ (force per length) at the free tip [30,46]. The plane stress condition with $E = 1 \times 10^3$ and Poisson's ratio $\nu = 0$ is used. The convergence behavior is studied by using both regular and distorted meshes of $N \times N$ elements ($N = 2$, 4, 8, and 16). The configuration of the distorted meshes used for the problem is given in Fig. 2.21(b).

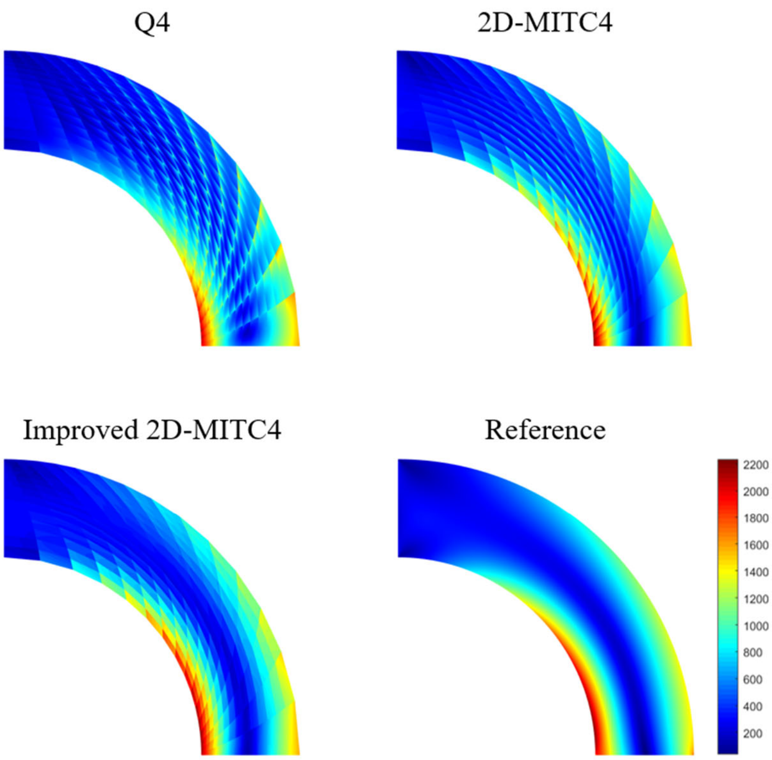

Fig. 2.24. von Mises stress (τ_{vM}) distributions of the curved beam problem obtained by using 16×16 distorted meshes. The reference stress distribution is obtained using a 64×64 mesh of 9-node quadrilateral elements.

Fig. 2.23 gives the normalized vertical displacements at point A . The convergence of the relative error in strain energy is depicted in Fig. 2.22. The reference solutions are obtained by using a 16×64 mesh of 9-node quadrilateral element. When the regular meshes are used, all elements except the Q4 element show similar performance, but when considering the mesh distortion, the performances of the original and simplified 2D-MITC4 elements deteriorate. However, the improved 2D-MITC4 and ICM-Q4 elements show much better predictive capability and give the almost same results.

The von Mises stress (τ_{vM}) distributions of the curved beam problem calculated by using 16×16 distorted meshes are given in Fig. 2.24. The reference von Mises stress (τ_{vM}) distribution is obtained using a 64×64 mesh of 9-node quadrilateral elements. Also, Fig. 2.25 gives the von Mises stress distributions along the curved edge AB considering distorted meshes with $N=8$,16 , and 32 . Note that the improved 2D-MITC4 element gives more accurate solutions and closely follows the reference stress distributions along the curved edge in spite of highly distorted meshes.

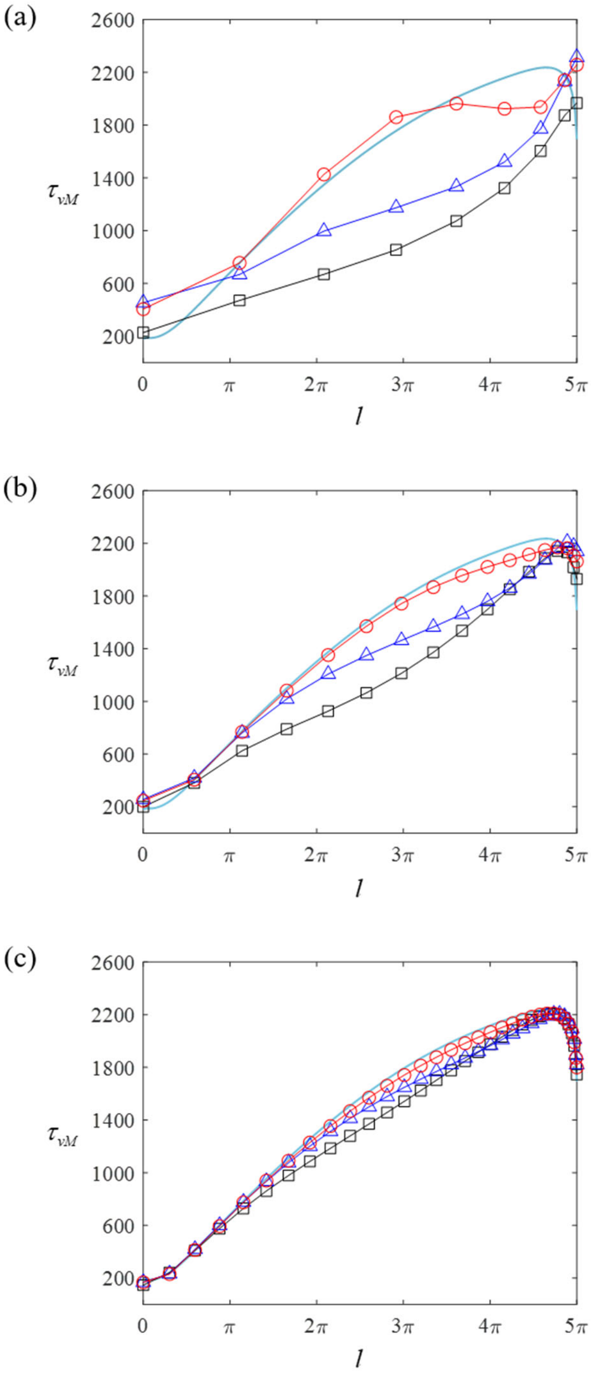

Fig. 2.25. von Mises stress distributions along the arc AB of the curved beam problem for (a) 8×8 , (b) 16×16 and (c) 32×32 distorted meshes.

2.5.5. Block under complex body force

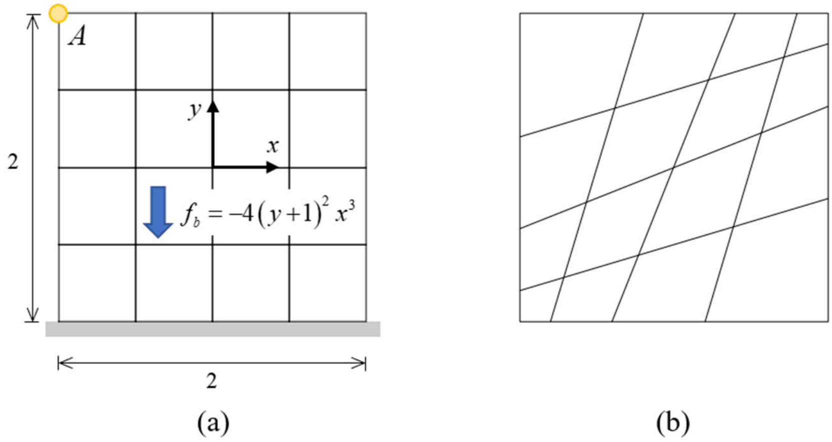

Fig. 2.26. Clamped box under complex body force problem ($E = 2 \times 10^7$ and plane strain conditions with $\nu = 0.47$, 0.49 or 0.499 for nearly incompressible materials). (a) Regular mesh when $N = 4$. (b) Distorted mesh I when $N = 4$.

A square box is clamped along its bottom and subjected to a body force $f_s = -4(y+1)^2 x^3$ (force per area), as shown in Fig. 2.26 [12]. The plane strain condition is employed with Young's modulus $E = 2.0 \times 10^7$ and Poisson's ratio $\nu = 0.3$. Solutions are obtained with $N \times N$ regular and distorted meshes (N = 2, 4, 8, and 16), see Fig. 2.26.

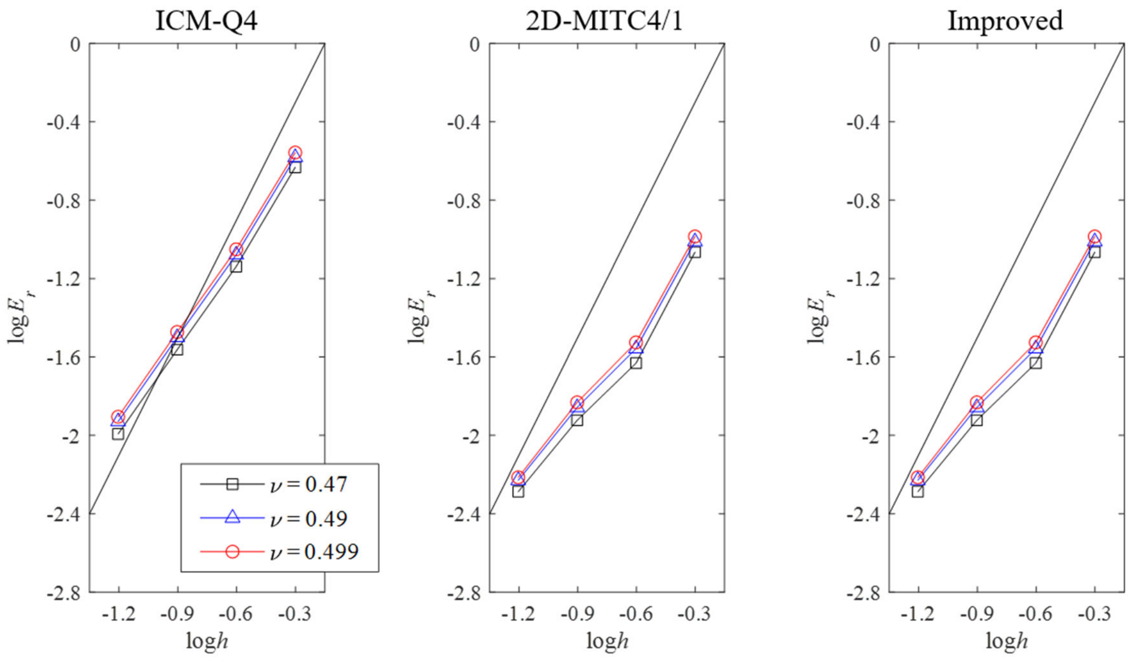

Fig. 2.27. Convergence curves for the clamped box under complex body force problem with regular meshes. Nearly incompressible material properties are considered. The bold line denotes the optimal convergence rate.

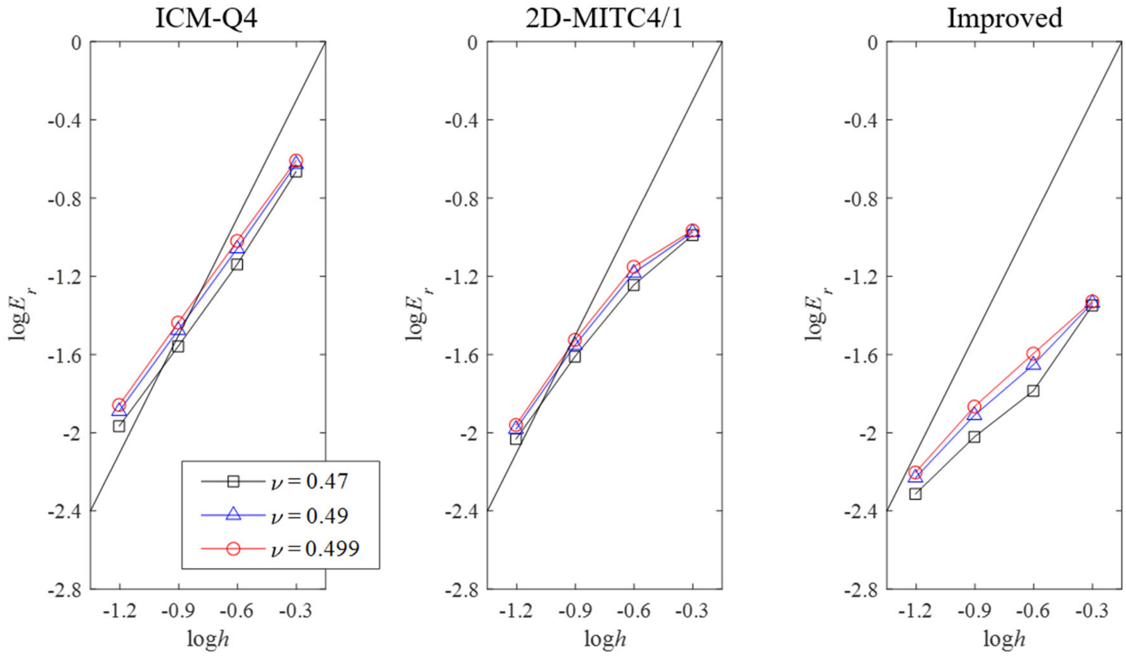

Fig. 2.28. Convergence curves for the clamped box under complex body force problem with distorted meshes I. Nearly incompressible material properties are considered. The bold line denotes the optimal convergence rate.

The plane strain analysis of nearly incompressible materials using the 2D-MITC4 element is performed first. Three Poisson's ratio $\nu = 0.47$, 0.49, and 0.499 are used. The convergences of relative errors in strain energy for regular and distorted meshes are given in Fig. 2.27 and Fig. 2.28 repectively. The improved 2D-MITC4 element performs well considering the nearly incompressible materials with plane strain assumption.

Then, the plane stress analysis is performed. One regular mesh and two distorted mesh patterns are considered: distorted mesh I in Fig. 2.26(b) and distorted mesh II in Fig. 2.29. The convergence curves of the relative error in strain energy are given in Fig. 2.30. The convergences of the normalized horizontal and vertical displacements at point A are shown in Fig. 2.31-Fig. 2.33 for each mesh patterns. The references for displacements and strain energy are calculated by using a 64×64 mesh of 9-node quadrilateral element. For the distorted mesh case, the improved 2D-MITC4 element gives much more accurate solutions than the original 2D-MITC4 element and also shows insensitivity to the mesh distortion similar to the ICM-Q4 element.

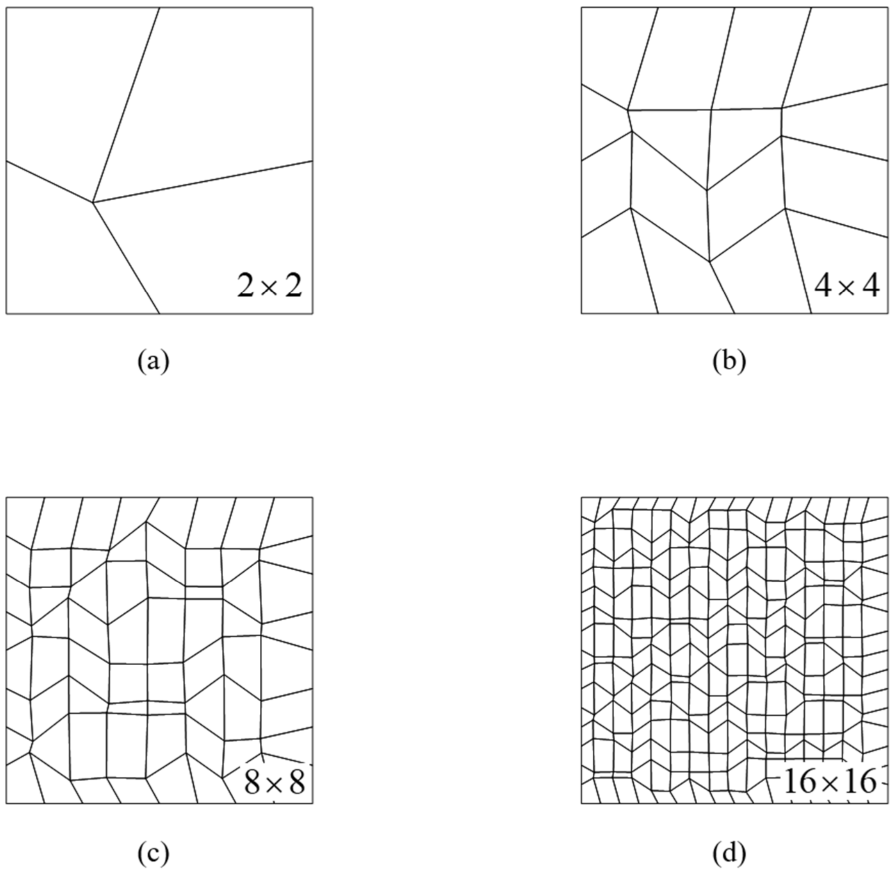

Fig. 2.29. Distorted mesh II when (a) $N = 2$, (b) $N = 2$, (c) $N = 8$ and (d) $N = 16$.

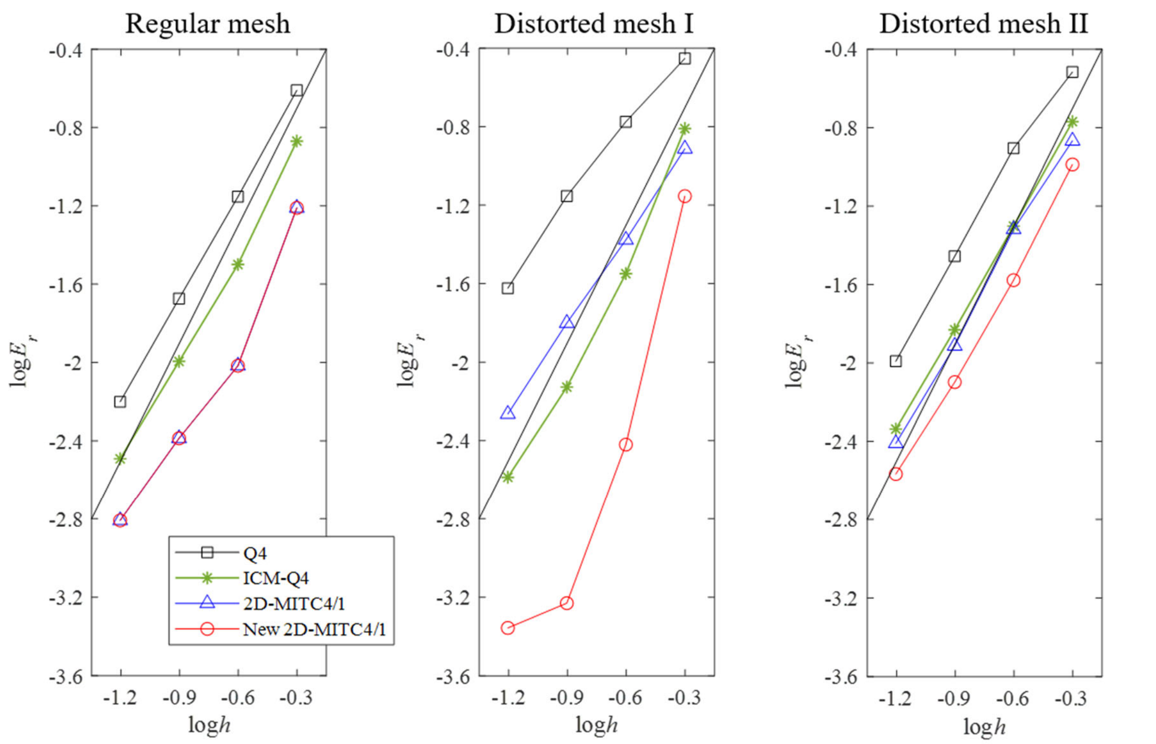

Fig. 2.30. Convergence curves for block under body force. The bold line denotes the optimal convergence rate.

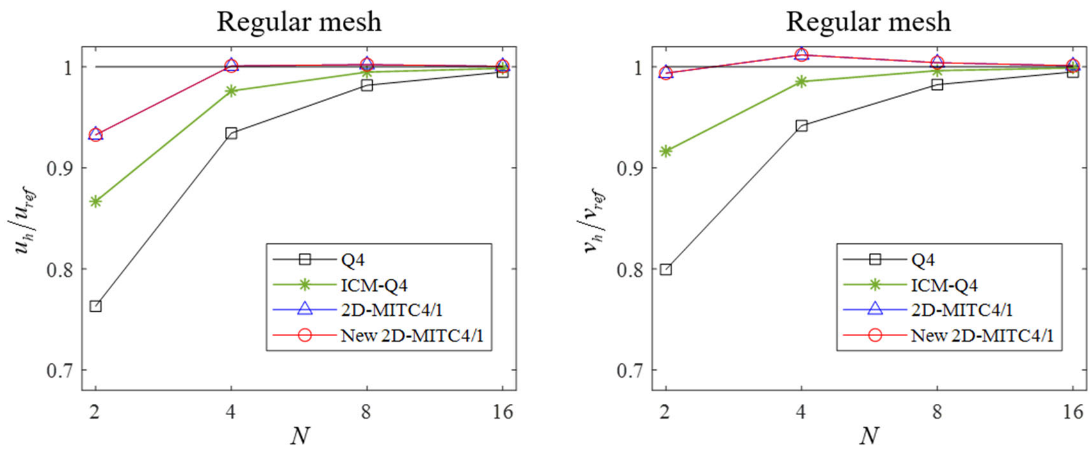

Fig. 2.31. Normalized (a) horizontal (u_h/u_{ref}) and (b) vertical (v_h/v_{ref}) displacements at point A in block under body force considering regular meshes.

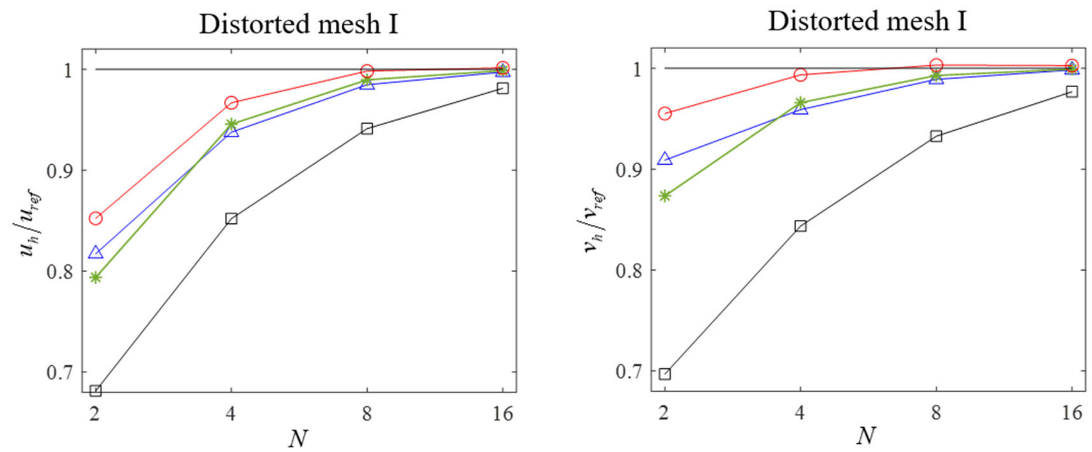

Fig. 2.32. Normalized (a) horizontal (u_h/u_{ref}) and (b) vertical (v_h/v_{ref}) displacements at point A in block under body force considering distorted meshes I.

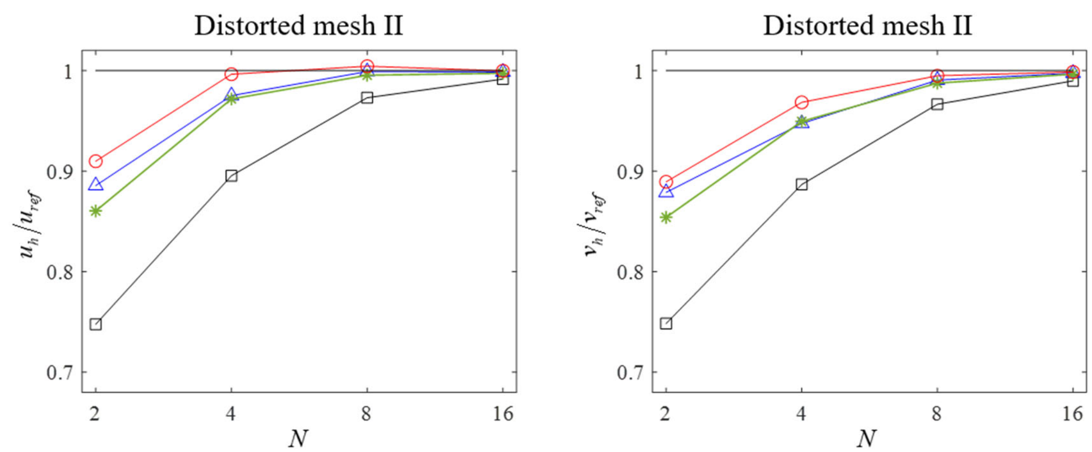

Fig. 2.33. Normalized (a) horizontal (u_h/u_{ref}) and (b) vertical (v_h/v_{ref}) displacements at point A in block under body force considering distorted meshes II.

2.6. Numerical examples for nonlinear analysis

In this section, nonlinear analysis using the improved 2D-MITC4 element is conducted including block sujected to a compression force, column under eccentric load, and cantilever beam subjected to a tip moment. The first example is considered to check wheather or not the element reveals spurious instabilities in nonlinear analysis. The next problem is conducted to show that the improved 2D-MITC4 element provides reliable solutions in both regular and distorted meshes.

2.6.1. Block subjected to a compression force

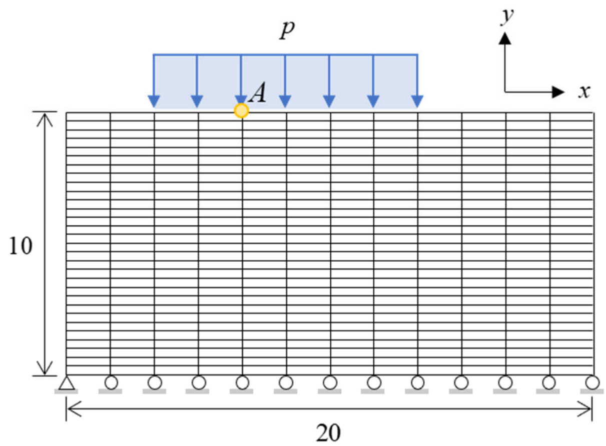

Fig. 2.34. Block subjected to a compression force with 12×30 mesh ($E = 1\times10^3$, $\nu = 0.3$ and $p_{\max} = -98$).

We solve the geometric nonlinear problem to investigate whether the improved 2D-MITC4 element shows spurious instabilities that appeared in the ICM-Q4 element. A block under a distributed compression force $P_{\max} = -98$ (force per length) is considered as shown in Fig. 2.34 [12,28,30]. The plane stress condition with Young's modulus $E = 1\times10^3$ and Poisson's ratio $\nu = 0.3$ is adopted and a 12×30 mesh is used.

The deformed configurations of each element at the load step $P/P_{\max} = 0.5125$ are given in Fig. 2.36. The 12×30 mesh of 9-node quadrilateral element is used to obtain the reference solutions. Fig. 2.35 shows the load-displacement curves representing the vertical displacement at point A according to a compression force. The original and improved 2D-MITC4 elements closely follow the reference path over the entire load steps without any spurious instability. However, the ICM-Q4 element reveals the instabilities showing a spurious hourglass mode as the load increases.

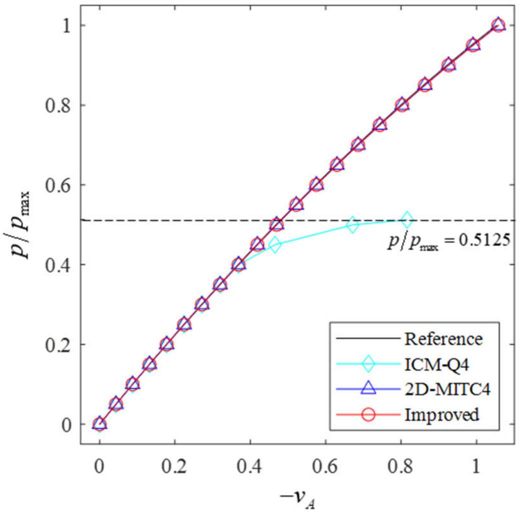

Fig. 2.35. Load-displacement curves at the point A in the block subjected to a compression force. The deformed shapes at the load step $p/p_{max} = 0.5125$ are given in Fig. 2.36.

(a)

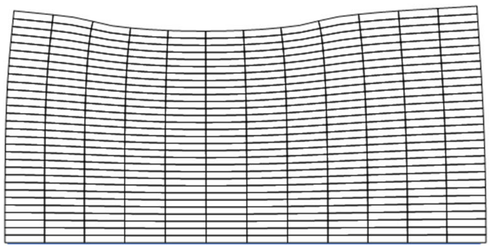

Reference

(b)

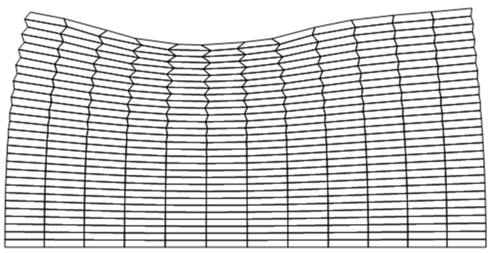

ICM-Q4

(c)

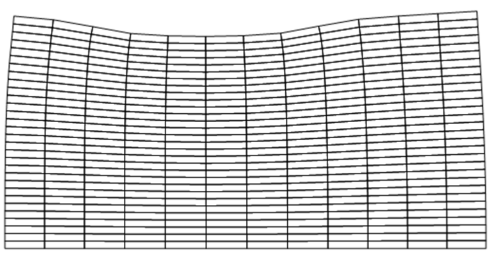

Improved 2D-MITC4

Fig. 2.36. The deformed configurations of the block subjected to a compression force at the load step $p/p_{max} = 0.5125$ with magnifying the displacements two times: (a) Standard 9-node element, (b) Incompatible modes element, (c) Improved 2D-MITC4 element.

2.6.2. Column under an eccentric load

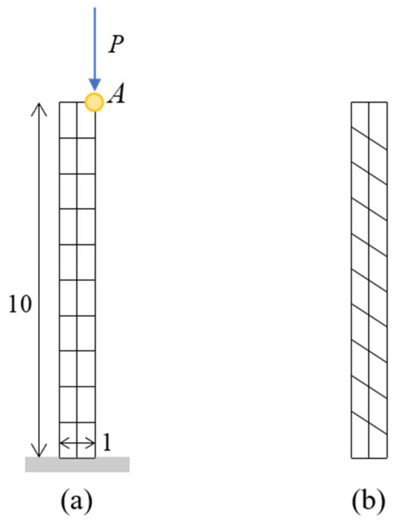

Fig. 2.37. Column under an eccentric load ($E = 10^6$, $\nu = 0$ and $P_{\max} = 4.5 \times 10^3$) modeled with (a) 2×10 regular mesh and (b) 2×10 distorted mesh.

The geometric nonlinear problem to investigate the performance of the improved 2D-MITC4 element considering both the regular and distorted meshes [40]. A column under an eccentric load $P_{\max} = 4.5 \times 10^3$ is applied at the point A as shown in Fig. 2.37. The plane stress condition with Young's modulus $E = 10^6$ and Poisson's ratio $\nu = 0$ is adopted and a 2×10 mesh is used for both regular and distorted meshes.

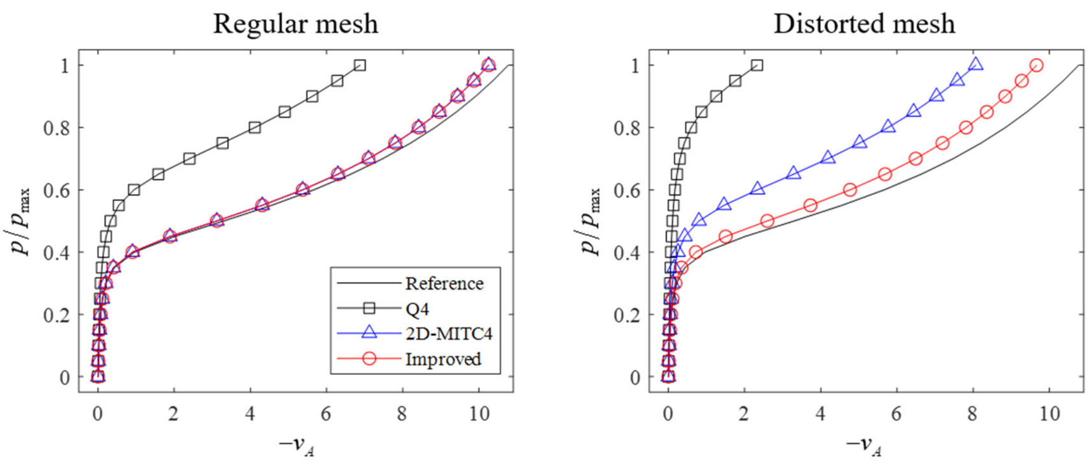

Fig. 2.38. Load-displacement curves ($-v_A$) for the column under an eccentric load for regular and distorted meshes.

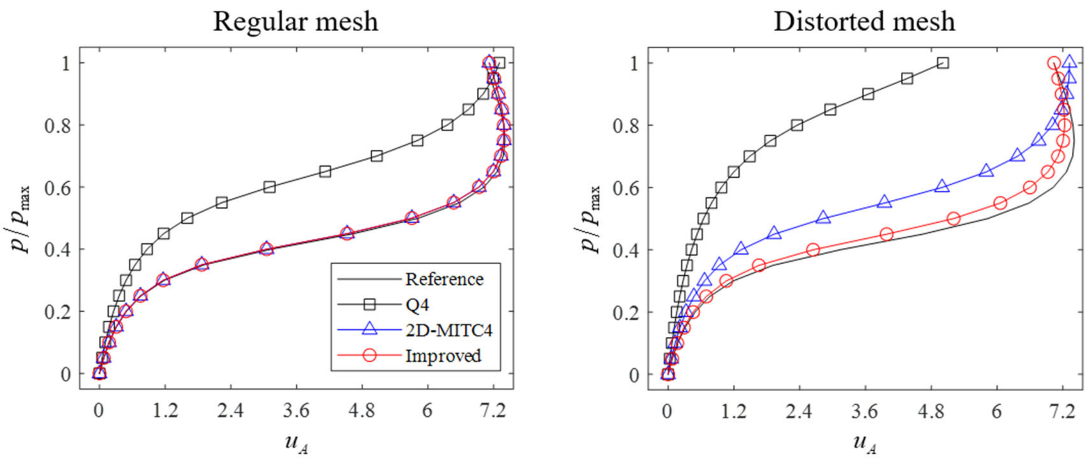

Fig. 2.39. Load-displacement curves (u_A) of the column under an eccentric load for regular and distorted meshes.

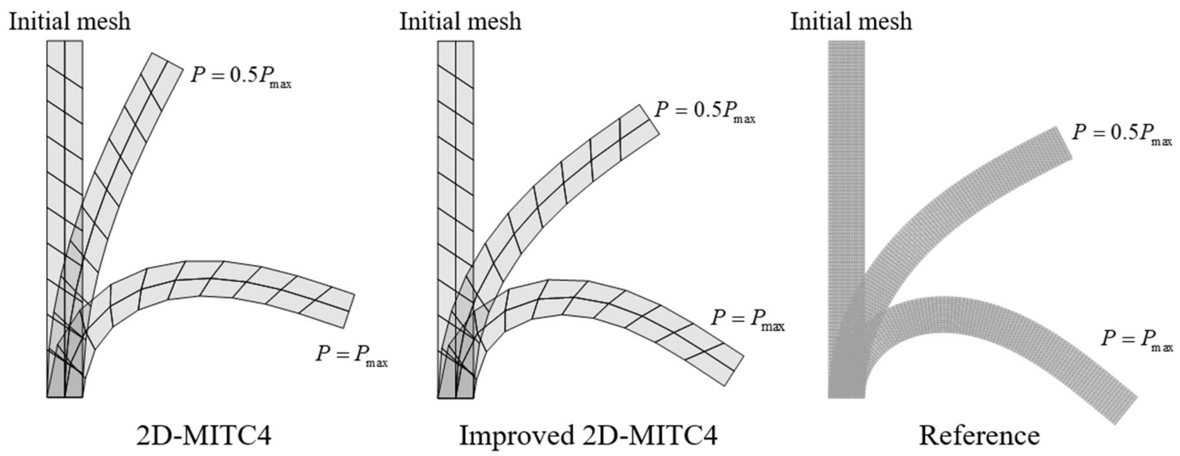

Fig. 2.40. Deformed configurations of the column under an eccentric load at the initial, middle and final load steps obtained by 2×10 distorted meshes. The reference solutions obtained by 20×100 mesh of standard 9-node element.

The deformed configurations of each element at the initia, middle, and final load steps ($P/P_{\max} = 0, 0.5, 1$) are given in Fig. 2.40. The 20×100 mesh of 9-node quadrilateral element is used to obtain the reference solutions. Fig. 2.38 and Fig. 2.39 shows the load-displacement curves representing the vertical ($-v_A$) and horizontal (u_A) displacement at point A according to a compression force, respectively. The original and improved 2D-MITC4 elements closely follow the reference path over the entire load steps when the regular mesh is used. However, the improved 2D-MITC4 element provides substantially improved results when considering the distorted mesh which is generally preferred in engineering practice.

Chapter 3. New 4-node quadrilateral shell finite element

Shell structures have been widely used in various engineering fields based on their efficient load-carrying capabilities [1,31]. For several decades, the finite element method (FEM) has been dominantly used to analyze shell structures [50]. Among various shell elements, 4-node quadrilateral shell elements are preferred due to their simplicity and efficiency [38,39], but most of them are not good enough to be used in engineering practice [36].

Shell finite elements suffer from the transverse shear and membrane locking problems which occur when the finite element discretization cannot accurately represent pure bending displacement fields [51,52]. The locking deteriorates the solution accuracy in bending-dominated problems and this deterioration becomes more serious as the shell thickness diminishes. Although there are a number of methods to reduce locking including assumed strain methods and reduced integration [17-19,53-65], it is well known that the mixed interpolation of tensorial components (MITC) method was successful [66-69].

Adopting the MITC method for the continuum mechanics based 4-node quadrilateral shell finite element [29], the MITC4+ shell element was recently developed by Ko et al [36]. Through a number of numerical examples, its excellent performance in both linear and nonlinear analysis has been demonstrated. The membrane behavior of the MITC4+ shell element is identical to the standard 4-node plane stress element. For this reason, the 2D-MITC4 solid element was embedded into the membrane strain field of the MITC4+ shell element, and consequently, the improved MITC4+ shell element was developed [30]. While the element shows great membrane performance in uniform meshes, the performance substantially deteriorates when the distorted meshes are used.

It is confirmed that the geometry dependent Gauss integration scheme is very effective at reducing the overly stiff in-plane bending behavior of 2D plane stress and strain problems. The major advantage of geometry dependent Gauss integration is that the solution accuracy is improved very efficiently. More specifically, the scheme doesn't need additional degrees of freedom, the computational cost for adjusting the integration points is merely increased, and it could be directly extended into the nonlinear analysis. As an interesting feature, the scheme is dependent only on the element geometry, not the formulation itself and thus, the scheme can be smoothly combined with the previous finite elements.

In this chapter, the new MITC4+ shell element is presented in detail. The covariant strain components are decomposed into the following three parts: membrane, bending, and transverse shear. To alleviate the transverse shear and membrane locking, the assumed strain field in the MITC4+ shell is adopted. The new assume membrane strain field is proposed to make the formulation more compact and straightforward compared with the improved MITC4+ shell element. Also, the geometry dependent Gauss integration scheme is extended to improve the membrane performance. Through various linear and nonlinear benchmark problems, the performance of the proposed element is demonstrated.

3.1. Geometry and displacement interpolations

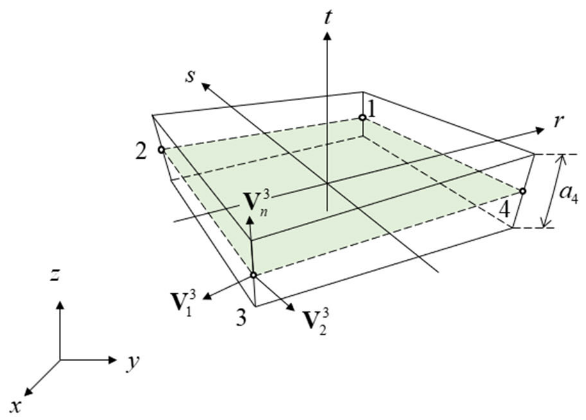

Fig. 3.1. Geometry of a 4-node quadrilateral shell element.

Using the natural coordinates *r*, *s*, and *t*, the geometry interpolation of the continuum mechanics based 4-node quadrilateral shell finite element is given by [66,67]

$$\mathbf{x}(r,s,t) = \sum_{i=1}^{4} h_i(r,s)\mathbf{x}_i + \frac{t}{2}\sum_{i=1}^{4} a_i h_i(r,s)\mathbf{V}_n^i \quad , \tag{3.1}$$

with $h_i(r,s) = \frac{1}{2}(1+\xi_i r)(1+\eta_i s)$, (3.2)

$$[\xi_1 \quad \xi_2 \quad \xi_3 \quad \xi_4] = [1 \quad -1 \quad -1 \quad 1], \tag{3.3}$$

$$[\eta_1 \quad \eta_2 \quad \eta_3 \quad \eta_4] = [1 \quad 1 \quad -1 \quad -1] \tag{3.4}$$

where a_i , $\mathbf{x}_i$ and $\mathbf{V}_n^i$ are shell thickness, position vectors, and director vectors corresponding to node *i*, respectively, and h_i is the two-dimensional shape function for the standard isoparametric procedure.

In the similar way, the displacement interpolation is obtained as

$$\mathbf{u}(r,s,t) = \sum_{i=1}^{4} h_i(r,s)\mathbf{u}_i + \frac{t}{2}\sum_{i=1}^{4} a_i h_i(r,s)(-\alpha_i \mathbf{V}_2^i + \beta_i \mathbf{V}_1^i) \tag{3.5}$$

in which $\mathbf{u}_i$ is the translational displacement vector in the global Cartesian coordinate system, $\mathbf{V}_1^i$ and $\mathbf{V}_2^i$ are unit vectors orthogonal to director vector $\mathbf{V}_n^i$ and to each other, and α_i and β_i are the rotational displacements of the director vectors about $\mathbf{V}_1^i$ and $\mathbf{V}_2^i$, respectively, at node *i*.

The displacement-based infinitesimal covariant strain components are given by [68,69]

$$e_{ij} = \frac{1}{2}(\mathbf{g}_i \cdot \mathbf{u}_{,j} + \mathbf{g}_j \cdot \mathbf{u}_{,i}) \quad \text{with} \quad i,j = 1,2,3 \tag{3.6}$$

in which $\mathbf{g}_i = \dfrac{\partial \mathbf{x}}{\partial r_i}$ and $\mathbf{u}_{,i} = \dfrac{\partial \mathbf{u}}{\partial r_i}$ with $r_1 = r$, $r_s = s$, $r_3 = t$ (3.7)

where $\mathbf{g}_i$ is the covariant base vector and $\mathbf{u}_{,i}$ is the displacement derivatives. The covariant strain components could be divided into in-layer strains (e_{rr}, e_{ss} and e_{rs}) and transverse shear strains (e_{rt} and e_{st}). Note that $e_{tt} = 0$ because the shell thickness is assumed to be constant.

The in-layer strain components could be divided further into membrane and bending strains as

$$e_{ij} = e_{ij}^{m} + te_{ij}^{b1} + t^2 e_{ij}^{b2} \quad \text{with } i, j = 1,2\ , \tag{3.8}$$

$$e_{ij}^{m} = \frac{1}{2}\left(\frac{\partial \mathbf{x}_m}{\partial r_i}\cdot\frac{\partial \mathbf{u}_m}{\partial r_j} + \frac{\partial \mathbf{x}_m}{\partial r_j}\cdot\frac{\partial \mathbf{u}_m}{\partial r_i}\right), \tag{3.9}$$

$$e_{ij}^{b1} = \frac{1}{2}\left(\frac{\partial \mathbf{x}_m}{\partial r_i}\cdot\frac{\partial \mathbf{u}_b}{\partial r_j} + \frac{\partial \mathbf{x}_m}{\partial r_j}\cdot\frac{\partial \mathbf{u}_b}{\partial r_i} + \frac{\partial \mathbf{x}_b}{\partial r_i}\cdot\frac{\partial \mathbf{u}_m}{\partial r_j} + \frac{\partial \mathbf{x}_b}{\partial r_j}\cdot\frac{\partial \mathbf{u}_m}{\partial r_i}\right), \tag{3.10}$$

$$e_{ij}^{b2} = \frac{1}{2}\left(\frac{\partial \mathbf{x}_b}{\partial r_i}\cdot\frac{\partial \mathbf{u}_b}{\partial r_j} + \frac{\partial \mathbf{x}_b}{\partial r_j}\cdot\frac{\partial \mathbf{u}_b}{\partial r_i}\right) \tag{3.11}$$

in which

$$\mathbf{x}_m = \sum_{i=1}^{4} h_i(r,s)\mathbf{x}_i\ ,\ \ \mathbf{x}_b = \frac{1}{2}\sum_{i=1}^{4} a_i h_i(r,s)\mathbf{V}_n^i\ , \tag{3.12}$$

$$\mathbf{u}_m = \sum_{i=1}^{4} h_i(r,s)\mathbf{u}_i\ ,\ \ \mathbf{u}_b = \frac{1}{2}\sum_{i=1}^{4} a_i h_i(r,s)(-\alpha_i \mathbf{V}_2^i + \beta_i \mathbf{V}_1^i)\,. \tag{3.13}$$

The strain term e_{ij}^{m} in Eq.(3.9) is the covariant membrane strain, and the remaining term including e_{ij}^{b1} and e_{ij}^{b2} is the covariant bending strain.

The membrane strain that is obtained at the mid surface of the element ($t = 0$) in Eq. (3.8) is rewritten as [36]

$$e_{rr}^{m} = e_{rr}^{con} + se_{rr}^{lin} + s^2 e_{rs}^{bil} \tag{3.14}$$

$$e_{ss}^{m} = e_{ss}^{con} + re_{ss}^{lin} + r^2 e_{rs}^{bil} \tag{3.15}$$

$$e_{rs}^{m} = e_{rs}^{con} + \frac{1}{2}re_{rr}^{lin} + \frac{1}{2}se_{ss}^{lin} + rse_{rs}^{bil} \tag{3.16}$$

with strain coefficients,

$$e_{rr}^{con} = \mathbf{x}_r \cdot \mathbf{u}_r\ ,\ \ e_{ss}^{con} = \mathbf{x}_s \cdot \mathbf{u}_s\ ,\ \ e_{rs}^{con} = \frac{1}{2}(\mathbf{x}_r \cdot \mathbf{u}_s + \mathbf{x}_s \cdot \mathbf{u}_r)\ , \tag{3.17}$$

$$e_{rr}^{lin} = \mathbf{x}_r \cdot \mathbf{u}_d + \mathbf{x}_d \cdot \mathbf{u}_r\ ,\ \ e_{ss}^{lin} = \mathbf{x}_s \cdot \mathbf{u}_d + \mathbf{x}_d \cdot \mathbf{u}_s\ ,\ \ e_{rs}^{bil} = \mathbf{x}_d \cdot \mathbf{u}_d \tag{3.18}$$

where the superscripts '*con*', '*lin*' and '*bil*' denote constant, linear and bilinear terms, repectively.

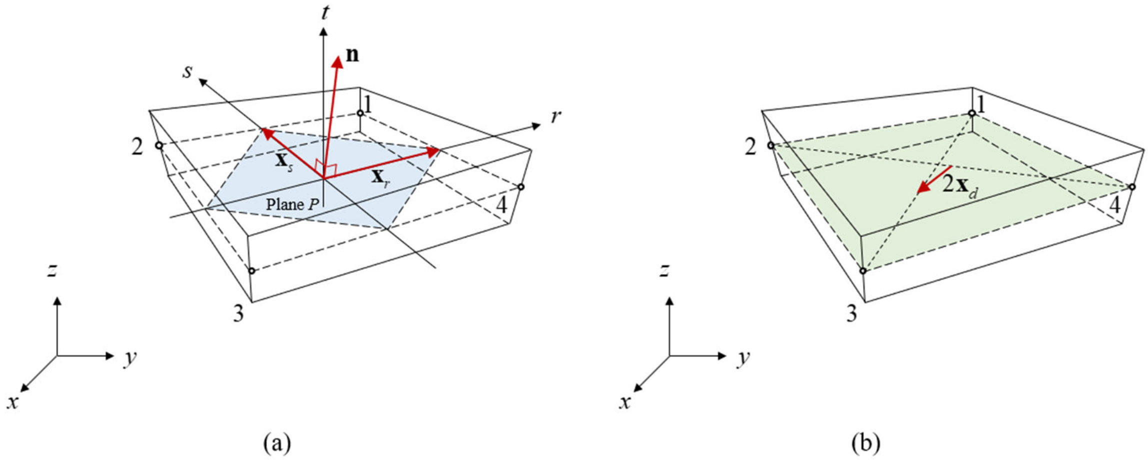

Fig. 3.2. Charateristic geometry vectors for a 4-node quadrilateral shell element. (a) Two vectors $\mathbf{x}_r$ and $\mathbf{x}_s$ in the plane *P* with normal vector $\mathbf{n}$. (b) Distortion vector $\mathbf{x}_d$.

The vectors in Eqs. (3.17) and (3.18) are characteristic geometry and displacement vectors as follows [30,36]:

$$\mathbf{x}_r = \frac{1}{4}\sum_{i=1}^{4}\xi_i \mathbf{x}_i \ , \ \ \mathbf{x}_s = \frac{1}{4}\sum_{i=1}^{4}\eta_i \mathbf{x}_i \ , \ \ \mathbf{x}_d = \frac{1}{4}\sum_{i=1}^{4}\xi_i \eta_i \mathbf{x}_i \ , \tag{3.19}$$

$$\mathbf{u}_r = \frac{1}{4}\sum_{i=1}^{4}\xi_i \mathbf{u}_i \ , \ \ \mathbf{u}_s = \frac{1}{4}\sum_{i=1}^{4}\eta_i \mathbf{u}_i \ , \ \ \mathbf{u}_d = \frac{1}{4}\sum_{i=1}^{4}\xi_i \eta_i \mathbf{u}_i \tag{3.20}$$

in which the vectors $\mathbf{x}_r$, $\mathbf{x}_s$ and $\mathbf{x}_d$ are the characteristic vectors as shown in Fig. 3.2, and the corresponding displacement vectors are $\mathbf{u}_r$, $\mathbf{u}_s$ and $\mathbf{u}_d$, respectively. Note that the vector $\mathbf{x}_d$ can stand for the warped distortion. The two vectors $\mathbf{x}_r$ and $\mathbf{x}_s$ construct the plane *P* with the normal vector $\mathbf{n}$,

$$\mathbf{n} = \frac{\mathbf{x}_r \times \mathbf{x}_s}{\left|\mathbf{x}_r \times \mathbf{x}_s\right|} \ . \tag{3.21}$$

Generally the displacement-based 4-node quadrilateral shell finite element suffers from the transverse shear locking and membrane locking. The transverse shear locking arises from the transverse shear strains e_{rt} and e_{st} and the membrane locking results from the covariant membrane strain component e_{ij}^{m}.

While there are various locking alleviation methods such as assumed strain method, enhanced strain method, and the reduced integration, the MITC method has been successfully used to develop the effective plate and shell elements, because the MITC method dosen’t need the additional degrees of freedom. In the following section, the treatment of both transverse shear and membrane locking in the MITC4+ is reviewed.

3.2. Original MITC4+ shell element

After the MITC method was first proposed to alleviate the transverse shear locking at the 4-node quadrilateral shell element (MITC4), various MITC family elements have been developed including high-order elements and quadrilateral and triangular elements [30-40,66-69]. There are many versions in the MITC4 shell element: MITC4 shell element with treatment of transverse shear locking [29], MITC4+ shell element with treatment of membrane locking [36], and improved MITC4+ shell element with improvement of the membrane performance [30]. Table 3.1 shows the features of the MITC based 4-node shell elements. In this chapter, the locking treamtments only for the 4-node quadrilateral shell element are reviewed.

Table 3.1. 4-node quadrilateral shell elements based on MITC method and descriptions.

Element	Descriptions
MITC4 (1984, Dvorkin and Bathe, [29])	▪ A continuum mechanics based 4-node shell element ▪ The transverse shear locking is alleviated by constructing the assumed transverse shear strain field based on MITC approach.
MITC4+ (2019,Ko et al., [36])	▪ The MITC4 shell element with alleviation of membrane locking ▪ The membrane locking is alleviated by assuming the locking-causing term as the linear combination of strain coefficients.
Improved MITC4+ (2019, Ko et al, [30])	▪ The MITC4+ shell element with improvement of membrane behavior ▪ The membrane performance is improved by embeding the original 2D-MITC4 solid element.
New MITC4+ (Proposed)	▪ The MITC4+ shell element with improvement of membrane behavior ▪ The membrane performance is improved by embeding the new 2D-MITC4 solid element and adopting geometry dependent Gauss integration.

3.2.1. Treatment of transverse shear locking

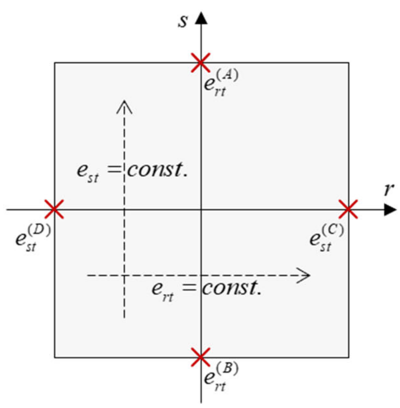

Fig. 3.3. Tying points (A)-(D) for the assumed transverse shear strain field of the MITC4 element and the corresponding strain components.

To reduce the transverse shear locking in the MITC4+ shell element, the following assumed covariant transverse shear strain fields are employed with four tying points (A)-(D) as shown in Fig. 3.3 [29,70].

$$\tilde{e}_{rt} = \frac{1}{2}(1+s)e_{rt}^{(A)} + \frac{1}{2}(1-s)e_{rt}^{(B)}, \tag{3.22}$$

$$\tilde{e}_{st} = \frac{1}{2}(1+r)e_{st}^{(C)} + \frac{1}{2}(1-r)e_{st}^{(D)}. \tag{3.23}$$

The above assumed transverse shear strain field is identical to the MITC4 shell element which was developed by Dvorkin and Bathe [29] and widely used in both research and industrial fields. It deosn't need an additional degrees of freedom and could be extended inro the nonlinear formulation in the same procedure.

The assumed strain field in Eqs. (3.22) and (3.23) is derived as follows:

$$\tilde{e}_{rt} = a + br + cs + drs \tag{3.24}$$

Let assume the strain is constant along the top and bottom edges of the element by the given tying points (A) and (B) as shown in Fig. 3.4(a). Then, the following conditions should be satisfied

$$\tilde{e}_{rt}(1,1) = e_{rt}^{(A)} \text{ and } \tilde{e}_{rt}(-1,1) = e_{rt}^{(A)} \text{ for the top edge,} \tag{3.25}$$

$$\tilde{e}_{rt}(1,-1) = e_{rt}^{(B)} \text{ and } \tilde{e}_{rt}(-1,-1) = e_{rt}^{(B)} \text{ for the bottom edge.} \tag{3.26}$$

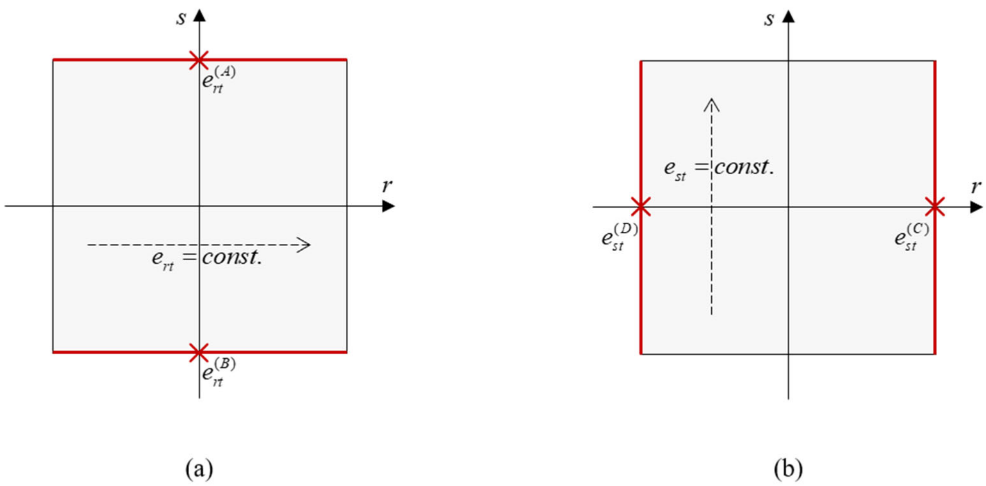

Fig. 3.4. Constant transverse shear strain is assumed along its edges. (a) Strain component e_{rt} is assumed constant in r direction. (b) Strain component e_{st} is assumed constant in s direction.

By substituting Eqs. (3.25) and (3.26) into Eq. (3.24), we can obtain the following linear equations

$$a+b+c+d = e_{rt}^{(A)}, \quad a-b+c-d = e_{rt}^{(A)} \tag{3.27}$$

$$a+b-c-d = e_{rt}^{(B)}, \quad a-b-c+d = e_{rt}^{(B)}. \tag{3.28}$$

Thus, the coefficients are obtained as

$$a = \frac{1}{2}(e_{rt}^{(A)} + e_{rt}^{(B)}), \quad c = \frac{1}{2}(e_{rt}^{(A)} - e_{rt}^{(B)}), \text{ and } b = d = 0. \tag{3.29}$$

The assumed transverse strain $\tilde{e}_{rt}$ becomes constant in the r direction. In the same way, the assumed transverse shear strain $\tilde{e}_{st}$ could be obtained, and it becomes constant in the s direction. Note that there is no modification in the covariant membrane strain field at Eq. (3.8) for the MITC4 element and it makes the MITC4 suffer membrane locking when they are distorted [70]. For this reason, the MITC4+ shell element was developed to reduce the membrane locking.

3.2.2. Treatment of membrane locking

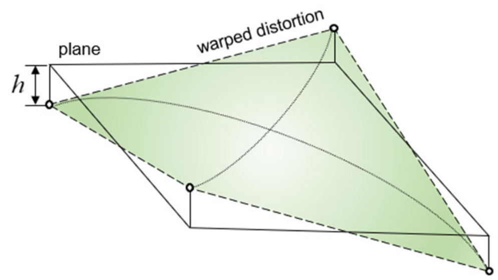

Fig. 3.5. Warped distortion in a 4-node quadrilateral shell element.

Unlike transverse shear locking, membrane locking occurs when the element geometry is warped as shown in Fig. 3.5 [36,70]. Since the geometry of the 3-node triangular shell element is always on a plane, it is free from membrane locking, but the 4-node quadrilateral shell element reveals membrane locking when the element geometry is distorted in the curved surface. Therefore, membrane locking should be treated appropriately in the 4-node quadrilateral element. First, the strain term that cause membrane locking is investigated and then, assumed strain field of the locking causing term is constructed by adopting MITC method.

Note that the treatment of the membrane locking is not to improve the membrane performance but to improve the bending performance of the shell element. Therefore, the membrane performance of the MITC4+ shell element is still identical the standard 4-node quadrilateral plane stress element and thus, it reveals some over stiff behavior under the in-plane bending deformation. Thus, the improved MITC4 shell element has been developed to enhance the membrane behavior of the shell element. However, the membrane performance still deteriorates when the element geometry is distorted. This issue will be handled at the new MITC4+ shell element by introducing the new membrane strain field and geometry dependent Gauss integration scheme. More specifically, the performance of the MITC4 and MITC4+ shell elements are identical when the geometry is flat, the performance of the improved MITC4+ and the new MITC4+ shell element are identical when there is no element distortion.

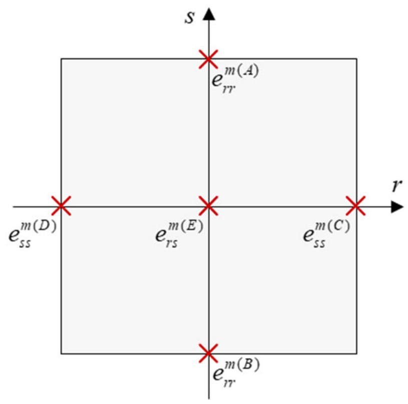

Fig. 3.6. Tying points (A)-(E) for the assumed membrane strain field of the MITC4+ element and the corresponding strain components.

Using tying points (A)-(E) as shown in Fig. 3.6, the assumed membrane strain field is constructed as follows [36]:

$$\hat{e}_{rr}^{m} = \frac{1}{2}(e_{rr}^{m(A)} + e_{rr}^{m(B)}) + \frac{1}{2}(e_{rr}^{m(A)} - e_{rr}^{m(B)})s \tag{3.30}$$

$$\hat{e}_{ss}^{m} = \frac{1}{2}(e_{ss}^{m(C)} + e_{ss}^{m(D)}) + \frac{1}{2}(e_{ss}^{m(C)} - e_{ss}^{m(D)})r \tag{3.31}$$

$$\hat{e}_{rr}^{m} = e_{rr}^{m(E)}. \tag{3.32}$$

By comparing the assumed strain field in Eqs. (3.30)-(3.32) with the displacement-based strain field in Eqs. (3.14)-(3.16), we can identify the following relations,

$$e_{rr}^{m} = \hat{e}_{rr}^{m} + (s^2 - 1)e_{rs}^{bil}, \tag{3.33}$$

$$e_{ss}^{m} = \hat{e}_{ss}^{m} + (r^2 - 1)e_{rs}^{bil}, \tag{3.34}$$

$$e_{rs}^{m} = \hat{e}_{rs}^{m} + rse_{rs}^{bil}. \tag{3.35}$$

Note that all the difference between the assumed strain field and the displacement-based strain contains the bilinear strain term, $e_{rs}^{bil} = \mathbf{x}_d \cdot \mathbf{u}_d$ in Eq. (3.18). The bilinear term is known to cause membrane locking [59].

In order to modify e_{rs}^{bil} to alleviate the membrane locking, the idea of Kulikov and Plotnikova is adopted. The assumed bilinear strain is established by the linear combination of the five strain coefficients in Eq. (3.17)

$$\tilde{e}_{rs}^{bil} = C_1(e_{rr}^{con} + e_{rs}^{bil}) + C_2(e_{ss}^{con} + e_{rs}^{bil}) + C_3 e_{rs}^{con} + C_4 e_{rr}^{lin} + C_5 e_{ss}^{lin} \tag{3.36}$$

whre the coefficients (C_1, C_2, C_3, C_4 and C_5) should be determined considering the membrane patch tests.

In other words, the assumed bilinear strain should be identical to the displacement-based bilinear strain when the element geometry is flat

$$\tilde{e}_{rs}^{bil} = e_{rs}^{bil} \quad \text{when} \quad \mathbf{x}_d \cdot \mathbf{n} = 0\,. \tag{3.37}$$

For a flat geometry ($\mathbf{x}_d \cdot \mathbf{n} = 0$), the distortion vector $\mathbf{x}_d$ in Eq. (3.19) is in the plane *P* and thus, become

$$\mathbf{x}_d = c_r \mathbf{x}_r + c_s \mathbf{x}_s \quad \text{with} \quad c_r = \mathbf{x}_d \cdot \widehat{\mathbf{g}}^r \quad \text{and} \quad c_s = \mathbf{x}_d \cdot \widehat{\mathbf{g}}^s \tag{3.38}$$

where the two vectors $\widehat{\mathbf{g}}^r$ and $\widehat{\mathbf{g}}^s$ are contravariant base vectors evaluated at the element center ($r = s = t = 0$) in *r* and *s* direction, respectively.

The five coefficients in Eq. (3.36) could be determined by solving Eq. (3.37) for arbitrary in-plane deformation modes. Here, the following two deformation modes are considered [36]

$$\mathbf{u}_r = \mathbf{a}_r \,,\ \mathbf{u}_s = \mathbf{a}_s \,,\ \mathbf{u}_d = \mathbf{0} \quad \text{for in-plane stretching and shearing modes,} \tag{3.39}$$

$$\mathbf{u}_r = \mathbf{0} \,,\ \mathbf{u}_s = \mathbf{0} \,,\ \mathbf{u}_d = \mathbf{x}_d \quad \text{for in-plane bending modes,} \tag{3.40}$$

whre the two vectors $\mathbf{a}_r$ and $\mathbf{a}_s$ are arbitrary vectors in the plane *P*.

Considering the deformation mode Eq. (3.39), the six strain coefficients in Eq. (3.17) and (3.18) are calculated as

$$e_{rr}^{con} = \mathbf{x}_r \cdot \mathbf{a}_r \,,\ e_{ss}^{con} = \mathbf{x}_s \cdot \mathbf{a}_s \,,\ e_{rs}^{con} = \frac{1}{2}(\mathbf{x}_r \cdot \mathbf{a}_s + \mathbf{x}_s \cdot \mathbf{a}_r) \,, \tag{3.41}$$

$$e_{rr}^{lin} = \mathbf{x}_d \cdot \mathbf{a}_r \,,\ e_{ss}^{lin} = \mathbf{x}_d \cdot \mathbf{a}_s \,,\ e_{rs}^{bil} = 0 \tag{3.42}$$

and the assumed bilinear strain should be zero from the relation in Eq. (3.37),

$$\tilde{e}_{rs}^{bil} = 0 \,. \tag{3.43}$$

Substituting Eqs. (3.41)-(3.42) into Eq. (3.37), the following equation is obtained

$$\left(C_1 \mathbf{x}_r + \frac{C_3}{2} \mathbf{x}_s + C_4 \mathbf{x}_d \right) \cdot \mathbf{a}_r + \left(C_2 \mathbf{x}_s + \frac{C_3}{2} \mathbf{x}_r + C_5 \mathbf{x}_d \right) \cdot \mathbf{a}_s = 0 \,. \tag{3.44}$$

Considering the deformation mode Eq. (3.40), the six strain coefficients in Eq. (3.17) are calculated as

$$e_{rr}^{con} = 0 \,,\ e_{ss}^{con} = 0 \,,\ e_{rs}^{con} = 0 \,, \tag{3.45}$$

$$e_{rr}^{lin} = \mathbf{x}_r \cdot \mathbf{x}_d \,,\ e_{ss}^{lin} = \mathbf{x}_s \cdot \mathbf{x}_d \,,\ e_{rs}^{bil} = \mathbf{x}_d \cdot \mathbf{x}_d \tag{3.46}$$

and from the relation in Eq. (3.37), the assumed bilinear strain should be

$$\tilde{e}_{rs}^{bil} = \mathbf{x}_d \cdot \mathbf{x}_d \,. \tag{3.47}$$

Substituting Eqs. (3.45)-(3.46) into Eq. (3.37), the following equation is obtained

$$C_1 \mathbf{x}_d \cdot \mathbf{x}_d + C_2 \mathbf{x}_d \cdot \mathbf{x}_d + C_4 \mathbf{x}_r \cdot \mathbf{x}_d + C_5 \mathbf{x}_s \cdot \mathbf{x}_d = \mathbf{x}_d \cdot \mathbf{x}_d \,. \tag{3.48}$$

Finally, the coefficients are determined by solving the linear equations in Eqs. (3.44) and (3.48)

$$C_1 = \frac{c_r^2}{d} \,,\ C_2 = \frac{c_s^2}{d} \,,\ C_3 = \frac{2 c_r c_s}{d} \,,\ C_4 = -\frac{c_r}{d} \,,\ C_5 = -\frac{c_s}{d} \quad \text{with} \quad d = c_r^2 + c_s^2 - 1 \tag{3.49}$$

and then, the assumed bilinear strain is written with the covariant membrane strains evaluated at five tying points (*A*)-(*E*),

$$\tilde{e}_{rs}^{bil} = e_{rr}^{m(A)} a_A + e_{rr}^{m(B)} a_B + e_{ss}^{m(C)} a_C + e_{ss}^{m(D)} a_D + e_{rs}^{m(E)} a_E \tag{3.50}$$

with $a_A = \dfrac{c_r(c_r-1)}{2d}$, $a_B = \dfrac{c_r(c_r+1)}{2d}$, $a_C = \dfrac{c_s(c_s-1)}{2d}$, $a_D = \dfrac{c_s(c_s+1)}{2d}$, and $a_E = \dfrac{2c_r c_s}{d}$. (3.51)

Considering the assumed membrane strain field in Eqs.(3.33)-(3.35) and the assumed bilinear strain all together, the following assumed membrane strain field is obtained

$$\tilde{e}_{rr}^{m} = \hat{e}_{rr}^{m} + (s^2-1)\tilde{e}_{rs}^{bil} \tag{3.52}$$

$$\tilde{e}_{ss}^{m} = \hat{e}_{ss}^{m} + (r^2-1)\tilde{e}_{rs}^{bil} \tag{3.53}$$

$$\tilde{e}_{rr}^{m} = \hat{e}_{rs}^{m} + rs\tilde{e}_{rs}^{bil} \tag{3.54}$$

and using Eqs. (3.30)-(3.32) and Eq. (3.50), the assumed strain field is represented by employing tying points (*A*)-(*E*)

$$\begin{aligned}\tilde{e}_{rr}^{m} &= \frac{1}{2}(1+s+2(s^2-1)a_A)e_{rr}^{m(A)} + \frac{1}{2}(1-s+2(s^2-1)a_B)e_{rr}^{m(B)} \\ &\quad + (s^2-1)a_C e_{ss}^{m(C)} + (s^2-1)a_D e_{ss}^{m(D)} + (s^2-1)a_E e_{rs}^{m(E)}\end{aligned}, \tag{3.55}$$

$$\begin{aligned}\tilde{e}_{ss}^{m} &= (r^2-1)e_{rr}^{m(A)} + (r^2-1)e_{rr}^{m(B)} + \frac{1}{2}(1+r+2(r^2-1)a_C)e_{ss}^{m(C)} \\ &\quad + \frac{1}{2}(1-r+2(r^2-1)a_D)e_{ss}^{m(D)} + (r^2-1)a_E e_{rs}^{m(E)}\end{aligned}, \tag{3.56}$$

$$\begin{aligned}\tilde{e}_{rs}^{m} &= \frac{1}{4}(r+4rsa_A)e_{rr}^{m(A)} + \frac{1}{4}(-r+4rsa_B)e_{rr}^{m(B)} + \frac{1}{4}(s+4rsa_C)e_{ss}^{m(C)} \\ &\quad + \frac{1}{4}(-s+4rsa_D)e_{ss}^{m(D)} + (1+rsa_E)e_{rs}^{m(E)}\end{aligned}. \tag{3.57}$$

Using the assumed membrane strain field, the assumed in-layer covariant strain is finally constructed as

$$\tilde{e}_{ij} = \tilde{e}_{ij}^{m} + te_{ij}^{b1} + t^2 e_{ij}^{b2}. \tag{3.58}$$

Note that only the membrane strain field is modified and the other terms for bending are not modified. The assumed membrane strain $\tilde{e}_{ij}^{m}$ is identical to the displacement-based membrane strain e_{ij}^{m} when the element geometry is flat.

The treatment of the membrane locking is only to improve the bending behavior of the shell structures in the curved geometry with distorted elements [39,70]. The membrane performance of the shell is equal to the standard 4-node quadrilateral plane stress element, and thus it needs to be enhanced to improve the in-plane bending behavior. For this reason, the improved MITC4+ shell element was developed by embedding the original 2D-MITC4 solid element into its membrane strain field [30]. The membrane performance is almost opimal by reducing the in-plane shear lockin in the uniform meshes without any numerical instabilities which is shown in the element with incompatible modes. However, the membrane performance of the improved MITC4+ shell element still deteriorates when the element mesh is distorted.

3.3. New MITC4+ shell element

The formulation of the new MITC4+ shell element is presented in detail. The new assumed membrane strain field is proposed to improve the membrane performance of the original MITC4+ shell element. The simplified assumed strain field in Eqs. (2.42)-(2.45) could be included as a specific case of the new assumed membrane strain field in this section. In addition, the geometry dependent Gauss integration scheme is extended into the new MITC4+ shell element. For the treatments of transverse shear locking, the same assumed transverse strain field of the MITC4 element is used and for the treatment of the membrane locking, the same assumed bilinear strain coefficient is adopted and collaborated with the new membrane strain field.

3.3.1. New assumed strain field

The new assumed strain field is constructed using temporal tying points that only exist during the derivation procedure and disappear in the final formulation. The new assumed strain field is almost identical in the simplified assumed strain field in Eqs. (2.42)-(2.45), but it is more simple and straightforward. Most of the performance improvement comes from the geometry dependent Gauss integration scheme. However, note that the geometry dependent Gauss integration gives the best results when it works together with the assumed strain field. For this reason, the membrane performance of the new MITC4+ shell elemnt is almost identical to the improved MITC4+ shell element when the element geometry is not distorted.

The new assumed membrane strain field for improving the membrane performance is constructed using the following strain components [30]

$$\hat{e}_{ij}^{m} = e_{kl}^{m} g_i^k g_j^l \quad \text{with} \quad \mathbf{g}^i \cdot \hat{\mathbf{g}}_j = g_i^j \tag{3.59}$$

where the vector $\hat{\mathbf{g}}_i$ is the covariant base vector evaluated at the element center ($r = s = t = 0$).

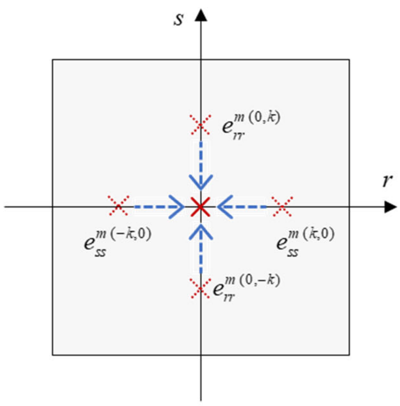

Fig. 3.7. Temporal tying points for the new assumed membrane strain field to improve the membrane performance of the MITC4+ element. The tying points are merged into the element center.

In order to figure out how the position of the tying points affect the performance of the element, we first generalize the formulation of the 2D-MITC4 element with a variable *k*, which determine the positions of points *A*, *B*, *C* and *D* in the range $[0, 1]$, as shown in Fig. 3.7.

$$\hat{e}_{rr}^{AS}(r,s) = \hat{e}_{rr}^{(0,0)} + \lambda(r,s)\frac{\hat{e}_{rr}^{(0,k)} - \hat{e}_{rr}^{(0,-k)}}{2k}s\,, \tag{3.60}$$

$$\hat{e}_{ss}^{AS}(r,s) = \hat{e}_{ss}^{(0,0)} + \lambda(r,s)\frac{\hat{e}_{ss}^{(k,0)} - \hat{e}_{ss}^{(-k,0)}}{2k}r\,, \tag{3.61}$$

$$\hat{e}_{rs}^{AS}(r,s) = \hat{e}_{rs}^{(0,0)} \text{ with } \lambda(r,s) = \frac{\det(\mathbf{J}(0,0))}{\det(\mathbf{J}(r,s))}\,, \tag{3.62}$$

The simplified assumed strain field in Eqs. (2.42)-(2.45) can be obtained by setting k to $1/\sqrt{3}$.

By calculating the strain components at each tying point and substituting them into Eqs. (3.60)-(3.62), the assumed strain field could be rewritten using the characteristic geometry and displacement vectors as

$$\hat{e}_{rr}^{AS}(r,s) = \mathbf{x}_r \cdot \mathbf{u}_r + \frac{1}{1-k^2\alpha^2}\left[\lambda(r,s)\left(-\alpha\mathbf{x}_r \cdot \mathbf{u}_r - \beta\mathbf{x}_r \cdot \mathbf{u}_s + \mathbf{x}_r \cdot \mathbf{u}_d\right)s\right], \tag{3.63}$$

$$\hat{e}_{ss}^{AS}(r,s) = \mathbf{x}_s \cdot \mathbf{u}_s + \frac{1}{1-k^2\beta^2}\left[\lambda(r,s)\left(-\beta\mathbf{x}_s \cdot \mathbf{u}_s - \alpha\mathbf{x}_s \cdot \mathbf{u}_r + \mathbf{x}_s \cdot \mathbf{u}_d\right)r\right], \tag{3.64}$$

$$\hat{e}_{rs}^{AS}(r,s) = \frac{1}{2}\left(\mathbf{x}_r \cdot \mathbf{u}_s + \mathbf{x}_s \cdot \mathbf{u}_r\right), \tag{3.65}$$

$$\text{with } \alpha = \mathbf{x}_d \cdot \hat{\mathbf{g}}^r \text{ and } \beta = \mathbf{x}_d \cdot \hat{\mathbf{g}}^s\,, \tag{3.66}$$

where the vectors $\hat{\mathbf{g}}^r$ and $\hat{\mathbf{g}}^s$ are the contravariant base vectors at the element center. Note that the tying position affects the second terms in Eqs. (3.63) and (3.64) which represent the bending behavior.

As the tying points move away from the element center, the bending stiffness becomes larger. To minimize the bending stiffness, a new assumed strain field is obtained by setting $k = 0$,

$$\hat{e}_{rr}^{AS}(r,s) = \mathbf{x}_r \cdot \mathbf{u}_r + \lambda(r,s)\left(-\alpha\mathbf{x}_r \cdot \mathbf{u}_r - \beta\mathbf{x}_r \cdot \mathbf{u}_s + \mathbf{x}_r \cdot \mathbf{u}_d\right)s\,, \tag{3.67}$$

$$\hat{e}_{ss}^{AS}(r,s) = \mathbf{x}_s \cdot \mathbf{u}_s + \lambda(r,s)\left(-\beta\mathbf{x}_s \cdot \mathbf{u}_s - \alpha\mathbf{x}_s \cdot \mathbf{u}_r + \mathbf{x}_s \cdot \mathbf{u}_d\right)r\,, \tag{3.68}$$

$$\hat{e}_{rs}^{AS}(r,s) = \frac{1}{2}\left(\mathbf{x}_r \cdot \mathbf{u}_s + \mathbf{x}_s \cdot \mathbf{u}_r\right). \tag{3.69}$$

The new assumed strain field in Eqs. (3.67)-(3.69) consists of the characteristic vectors in a direct way and thus, the element formulation becomes much simpler than that of the original 2D-MITC4 element. In addition, the performance is merely better than the assumed strain field in Eqs. (2.42)-(2.45).

The new assumed strain field is then rewritten with strain coefficients in Eqs. (3.17)-(3.18)

$$\hat{e}_{rr}^{AS}(r,s) = e_{rr}^{con} + \lambda(r,s)(-2\alpha e_{rr}^{con} - 2\beta e_{rs}^{con} + e_{rr}^{lin})\,, \tag{3.70}$$

$$\hat{e}_{ss}^{AS}(r,s) = e_{ss}^{con} + \lambda(r,s)(-2\beta e_{ss}^{con} - 2\alpha e_{rs}^{con} + e_{ss}^{lin})\,, \tag{3.71}$$

$$\hat{e}_{rs}^{AS}(r,s) = e_{rs}^{con}\,. \tag{3.72}$$

3.3.2. Formulation of the new MITC4+ shell element

In the formulation of the new MITC4+ shell element, the new assumed membrane strain field in Eqs. (3.70)-(3.72) is used to improve the membrane performance and the treatment of transverse shear and membrane locking is adopting.

For the assumed transverse strain field to alleviate the transverse shear locking, the assumed field in MITC4 element is adopted [69],

$$\tilde{e}_{rt} = \frac{1}{2}(1+s)e_{rt}^{(A)} + \frac{1}{2}(1-s)e_{rt}^{(B)}, \quad \tilde{e}_{st} = \frac{1}{2}(1+r)e_{st}^{(C)} + \frac{1}{2}(1-r)e_{st}^{(D)} \tag{3.73}$$

where the tying points (A)-(D) are denoted in Fig. 3.3.

In order to improve the membrane performance, the new assumed strain field in Eqs. (3.70)-(3.72) is embeded into the membrane strain field of the MITC4+ shell element. For the compact formulation, the assumed strain field is represented in matrix form [30],

$$\begin{bmatrix} \hat{e}_{rr}^{AS} \\ \hat{e}_{ss}^{AS} \\ \hat{e}_{rs}^{AS} \end{bmatrix} = \mathbf{M}(r,s)\begin{bmatrix} e_{rr}^{con} & e_{ss}^{con} & e_{rs}^{con} & e_{rr}^{lin} & e_{ss}^{lin} \end{bmatrix}^{\mathrm{T}} \tag{3.74}$$

$$\text{with } \mathbf{M}(r,s) = \begin{bmatrix} 1-2\alpha s\lambda & 0 & -2\beta s\lambda & \lambda s & 0 \\ 0 & 1-2\beta r\lambda & -2\alpha r\lambda & 0 & \lambda r \\ 0 & 0 & 1 & 0 & 0 \end{bmatrix} \tag{3.75}$$

where the strain coefficients are defined at Eqs. (3.17)-(3.18), and the α and β are given by Eq. (3.66)

The strain coefficient is calculated by using tying points (A)-(E) as follows:

$$e_{rr}^{con} + e_{rs}^{bil} = \frac{1}{2}(e_{rr}^{m(A)} + e_{rr}^{m(B)}) \; e_{rr}^{lin} = \frac{1}{2}(e_{rr}^{m(A)} - e_{rr}^{m(B)}) \tag{3.76}$$

$$e_{ss}^{con} + e_{rs}^{bil} = \frac{1}{2}(e_{ss}^{m(C)} + e_{ss}^{m(D)}) \; e_{ss}^{lin} = \frac{1}{2}(e_{ss}^{m(C)} - e_{ss}^{m(D)}) \tag{3.77}$$

$$e_{rs}^{con} = e_{rs}^{m(E)}. \tag{3.78}$$

By taking into account both the assumed strain field in Eqs. (3.76)-(3.77) and the treamtment of membrane locking in Eqs. (3.55)-(3.57), the following formulation is defined as

$$\begin{bmatrix} e_{rr}^{con} & e_{ss}^{con} & e_{rs}^{con} & e_{rr}^{lin} & e_{ss}^{lin} \end{bmatrix}^{\mathrm{T}} = \mathbf{C}\begin{bmatrix} e_{rr}^{m(A)} & e_{rr}^{m(B)} & e_{ss}^{m(C)} & e_{ss}^{m(D)} & e_{rs}^{m(E)} \end{bmatrix}^{\mathrm{T}} \tag{3.79}$$

$$\text{with } \mathbf{C} = \begin{bmatrix} 1/2-a_A & 1/2-a_B & -a_C & -a_D & -a_E \\ -a_A & -a_B & 1/2-a_C & 1/2-a_D & -a_E \\ 0 & 0 & 0 & 0 & 1 \\ 1/2 & -1/2 & 0 & 0 & 0 \\ 0 & 0 & 1/2 & -1/2 & 0 \end{bmatrix}. \tag{3.80}$$

To couple the new assumed membrane strain field in Eqs.(3. 74) with the bending and transverse shear strain in MITC4+ shell element, the strain field should be transformed into covariant strain field consistently,

$$\begin{bmatrix} \tilde{e}_{rr}^{m} \\ \tilde{e}_{ss}^{m} \\ \tilde{e}_{rs}^{m} \end{bmatrix} = \mathbf{Q} \begin{bmatrix} \hat{e}_{rr}^{AS} \\ \hat{e}_{ss}^{AS} \\ \hat{e}_{rs}^{AS} \end{bmatrix} \tag{3.81}$$

in which the matrix $\mathbf{Q}$ is the transformation matrix of strain components Eq.(3.59) into covariant strain components.

Finally, the new assumed membrane field is expressed using tying points (*A*)-(*E*) in Fig. 3.6 as

$$\begin{bmatrix} \tilde{e}_{rr}^{m} \\ \tilde{e}_{ss}^{m} \\ \tilde{e}_{rs}^{m} \end{bmatrix} = \mathbf{QMC}\begin{bmatrix} e_{rr}^{m(A)} & e_{rr}^{m(B)} & e_{ss}^{m(C)} & e_{ss}^{m(D)} & e_{rs}^{m(E)} \end{bmatrix}^{\mathrm{T}} \tag{3.82}$$

and the in-layer strain components are given by

$$\tilde{e}_{ij} = \tilde{e}_{ij}^{m} + te_{ij}^{b1} + t^{2}e_{ij}^{b2}\ . \tag{3.83}$$

The assumed field in Eq. (3.82) is closely related to the field of the improved MITC4+ shell element [30]. However, there is no bilinear strain coefficients and thus the formulation become much simpler than that of the improved MITC4+ shell element. Of course, if there is no distorted element, the resultant strain field is identical to each other, but for the distorted element case, the proposed assumed strain field performs merely better. The difference between the new MITC4+ and improved MITC4+ shell elements is compared in Table 3.2.

Table 3.2. Comparison of the formulation between the improved MITC4+ and new MITC4+ shell elements

	Original MITC4+ (2019, Ko. et al., [30])	New MITC4+ (proposed)
M	$\lambda\begin{bmatrix} 1/\lambda+\sqrt{3}n_1 s & \sqrt{3}m_2 r & 0 \\ \sqrt{3}n_2 s & 1/\lambda+\sqrt{3}m_1 r & 0 \\ 2\sqrt{3}n_5 s & 2\sqrt{3}m_5 r & 1 \\ n_3 s & m_4 r & 0 \\ n_4 s & m_3 r & 0 \\ n_1 s/\sqrt{3} & m_1 r/\sqrt{3} & 0 \end{bmatrix}^{\mathrm{T}}$ $n_1 \sim n_5$ and $m_1 \sim m_5$ are calculated from the Eqs. (2.33)-(2.38)	$\lambda\begin{bmatrix} 1/\lambda-2\alpha s & 0 & 0 \\ 0 & 1/\lambda-2\beta r & 0 \\ -2\beta s & -2\alpha r & 1 \\ s & 0 & 0 \\ 0 & r & 0 \end{bmatrix}^{\mathrm{T}}$
C	$\begin{bmatrix} 1/2-a_A & 1/2-a_B & -a_C & -a_D & -a_E \\ -a_A & -a_B & 1/2-a_C & 1/2-a_D & -a_E \\ 0 & 0 & 0 & 0 & 1 \\ 1/2 & -1/2 & 0 & 0 & 0 \\ 0 & 0 & 1/2 & -1/2 & 0 \\ a_A & a_B & a_C & a_D & a_E \end{bmatrix}$	$\begin{bmatrix} 1/2-a_A & 1/2-a_B & -a_C & -a_D & -a_E \\ -a_A & -a_B & 1/2-a_C & 1/2-a_D & -a_E \\ 0 & 0 & 0 & 0 & 1 \\ 1/2 & -1/2 & 0 & 0 & 0 \\ 0 & 0 & 1/2 & -1/2 & 0 \end{bmatrix}$

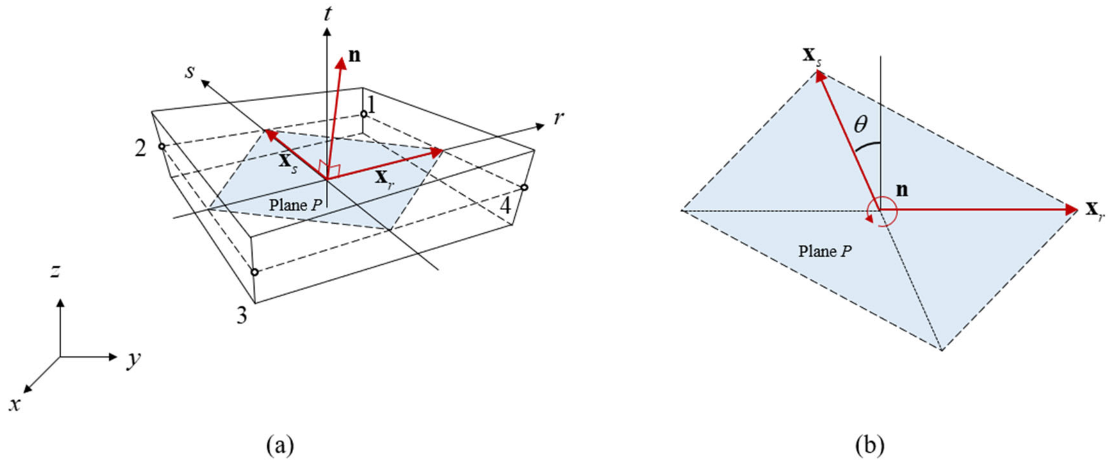

Fig. 3.8. Skewness of the 4-node quadrilateral shell element. (a) In-plane vectors $\mathbf{x}_r$ and $\mathbf{x}_s$ in the 3D space. (b) Skewness θ in the *r*-*s* space.

For the 4-node quadrilateral shell elements, the stiffness matrix is obtained generally unsing standard 2×2 Gauss integration in the *r*-*s* plane and also, standard 2 points Gauss integration in the thickness direction as follows:

$$\mathbf{K} = \sum_{k=1}^{2}\sum_{j=1}^{2}\sum_{i=1}^{2} w_i w_j w_k \mathbf{f}(\xi_i, \xi_j, \xi_k) \text{ with } \xi_1 = \frac{1}{\sqrt{3}},\ \xi_2 = -\frac{1}{\sqrt{3}},\ w_1 = w_2 = 1 \tag{3.84}$$

$$\text{and } \mathbf{f}(r,s,t) = \left[\mathbf{B}(r,s,t)^{\mathrm{T}}\mathbf{D}\mathbf{B}(r,s,t)\right]\det(\mathbf{J}(r,s,s)) \tag{3.85}$$

where ξ_i and w_i are Gauss quadrature point and the corresponding weight, and $\mathbf{B}$ is the strain-displacement relation matrix, and $\mathbf{J}$ is the Jacobian matrix, and $\mathbf{D}$ is the material law matrix for the shell element.

For the continuum mechanics based shell elements, the material law matrix in Eq. (3.86) is given by [1]

$$\mathbf{D} = \frac{E}{1-\nu^2}\begin{bmatrix} 1 & \nu & 0 & 0 & 0 & 0 \\ \nu & 1 & 0 & 0 & 0 & 0 \\ 0 & 0 & 0 & 0 & 0 & 0 \\ 0 & 0 & 0 & \frac{1-\nu}{2} & 0 & 0 \\ 0 & 0 & 0 & 0 & k\frac{1-\nu}{2} & 0 \\ 0 & 0 & 0 & 0 & 0 & k\frac{1-\nu}{2} \end{bmatrix} \tag{3.86}$$

where E and ν are the Young's modulus and Poisson's ratio, respectively.

In addition to the new assumed strain field, the geometry dependent Gauss integration in chapter 2 is adopted to improve the membrane performance. Note that the most of the performance improvement comes form the geometry dependent Gauss integration scheme.

For the shell element, the skewness θ of the element geometry and the corresponding adjusting parameter should be appropriately defined. Here, the skew anle of the element geometry is determinded using the characteristic geometry vectors $\mathbf{x}_r$ and $\mathbf{x}_s$ in the plane *P* in Fig. 3.8 and thus, the adjusting parameter μ is obtained as

$$\mu = \cos^2(\theta) \quad \text{with} \quad \cos(\theta) = \frac{1}{|\hat{\mathbf{g}}_r||\hat{\mathbf{g}}^r|} = \frac{1}{|\hat{\mathbf{g}}_s||\hat{\mathbf{g}}^s|}. \tag{3.87}$$

For the nonlinear analysis of the new MITC4+ shell element, the adjusting parameter is obtained from the initial element geometry since the total Lagrangian formulation is adopted in this thesis. Of cause, the adjusting parameter could be updated, if the updated Lagrangian formulation is adopted.

For the new MITC4+ shell element, the stiffness matrix is obtained by using modified 2×2 Gauss integration in the *r*-*s* plane and standard 2 points Gauss integration in the thickness direction as follows

$$\mathbf{K} = \sum_{k=1}^{2}\sum_{j=1}^{2}\sum_{i=1}^{2} w_i w_j w_k \mathbf{f}(\xi_i^{'}, \xi_j^{'}, \xi_k) \quad \text{with} \quad \xi_1^{'} = \frac{1}{\sqrt{3}}\mu, \quad \xi_1^{'} = -\frac{1}{\sqrt{3}}\mu, \quad w_1 = w_2 = 1. \tag{3.89}$$

Note that there is no modification at the weights. While the standard Gauss integration is employed at integration in thickness direction, the geometry dependent Gauss integration is adopted only at integration in the *r*-*s* plane.

For a plane stress problem, the new MITC4+ shell element become identical to the new 2D-MITC4 solid element because the assumed membrane strain field become identical to each other when the element geometry is in a plane and the geometry dependent Gauss integration gives the same quadrature points [30,36].

Once the integration points in *r*-*s* plane are modified from Eq.(3,84) to Eq.(3.89) to improve the membrane performance, the bending and transverse shear stiffnesses are also affected together. However, there is no problem to pass the basic tests, see the following section. In addition, the affection is not critical to decrease the bending and transverse shear performance of the element. This issues will be treated in the sections for linear analysis problems to study the convergence of the element.

3.4. Basic numerical tests

For the basic tests of the new MITC4+ shell element, the following tree tests are conducted: isotropy, zero energy mode, and patch tests [1,50-54]. The proposed element passes all the tests considered. For the isotropy, the element doesn't show any dependency in the sequence of node numbering. In zero energy mode test, the number of the rigid body modes should be six and this is confirmed by the numver of zeros eigenvalues of the elemental stiffness matrix. In the case of the patch tests, the geometry in Fig. 3.9 is considered. The in-plane stretching and bending are tested in the membrane patch test I and II. In addition, the bending and shearing tests are conducted. The proposed element passes all the cases for the patch tests.

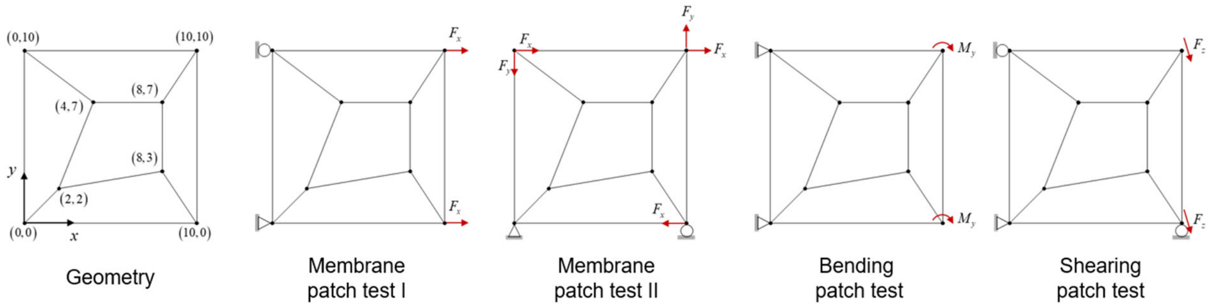

Fig. 3.9. The geometry for the patch tests and the boundary conditions for each test.

3.5. Numerical examples for linear analysis

In order to assess the performance of the proposed MITC4+ shell element, some selected benchmark problems in Table 3.3 are solved. The chosen problems are behavior-encompassing problems in membrane-dominant, bending-dominant, and mixed behavior of them [1].

Table 3.3. List of six benchmark problems considered for the convergence studies.

Problems	Boundary conditions	Descriptions	Results
Square plate	▪ Clamped	Fig. 3.12	Fig. 3.13
Cylindrical shell	▪ Clamped ▪ Free	Fig. 3.14, Fig. 3.15	Fig. 3.16, Fig. 3.17
Hyperboloid shell	▪ Clamped ▪ Free	Fig. 3.18, Fig. 3.19	Fig. 3.20, Fig. 3.21
Scordelis-Lo roof	▪ Diaphragm	Fig. 3.22, Fig. 3.23	Fig. 3.24, Fig. 3.25, Fig. 3.26
Hyperbolic cylinder shell	▪ Partly clamped	Fig. 3.27	Fig. 3.28

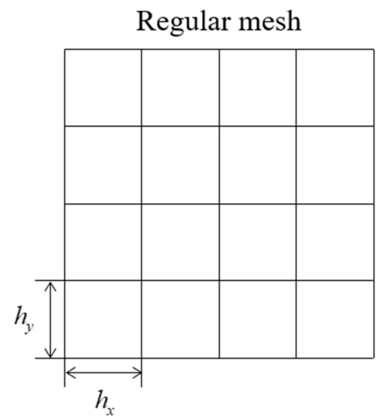

Fig. 3.10. $N \times N$ regular mesh pattern with $N = 4$.

The s-norm proposed by Hiller and Bathe [71] is used to measure the convergence of the finite element solutions

$$\left\|\mathbf{u}-\mathbf{u}_h\right\|_S^2 = \int_\Omega \Delta\boldsymbol{\varepsilon}^{\mathrm{T}} \Delta\boldsymbol{\tau} d\Omega \quad \text{with} \quad \Delta\boldsymbol{\varepsilon} = \boldsymbol{\varepsilon}-\boldsymbol{\varepsilon}_h \,, \;\; \Delta\boldsymbol{\tau} = \boldsymbol{\tau}-\boldsymbol{\tau}_h \,, \tag{3.89}$$

where $\mathbf{u}$ is the exact solution, $\mathbf{u}_h$ is the solution from the finite element discretization, and $\boldsymbol{\varepsilon}$ and $\boldsymbol{\tau}$ are the strain and stress vectors, respectively. This is a proper norm for investigating whether the approximated solution form the finite element analysis satisfy the consistency and inf-sup conditions [72-75].

Because it is extremely hard to obtain the exact or analytical solutions in the most of shell problems, the reference solution using a high-order element with a fine mesh is used to replace the exact solution. Therefore, the s-norm in Eq. (3.89) is modified as [33]

$$\left\|\mathbf{u}_{ref}-\mathbf{u}_h\right\|_S^2 = \int_{\Omega_{ref}} \Delta\boldsymbol{\varepsilon}^{\mathrm{T}} \Delta\boldsymbol{\tau} d\Omega_{ref} \quad \text{with} \quad \Delta\boldsymbol{\varepsilon} = \boldsymbol{\varepsilon}_{ref}-\boldsymbol{\varepsilon}_h \,, \;\; \Delta\boldsymbol{\tau} = \boldsymbol{\tau}_{ref}-\boldsymbol{\tau}_h \,, \tag{3.90}$$

To measure the convergence rate of the shell finite element depending on the thickness, the normalized relative error

$$E_h = \frac{\left\|\mathbf{u}_{ref}-\mathbf{u}_h\right\|_S^2}{\left\|\mathbf{u}_{ref}\right\|_S^2} \,. \tag{3.91}$$

The theoretical convergence rate can be evaluated as

$$\left\|\mathbf{u}_{ref}-\mathbf{u}_h\right\|_S^2 \cong ch^k \tag{3.92}$$

where c is a constant independent to shell thickness, h is the element size, and k denotes the order of convergence. For the 4-node shell element, the optimal value for k is 2.

For the convergence studies in this section, well-converged reference solutions are obtained by using the MITC9 shell element with a fine regular mesh. In the following problems, the results of MITC4, MITC4+, improved MITC4+, and new MITC4+ shell elements are compared to each other considering thickness decrease in both regular and distorted mesh patterns [29,30,36].

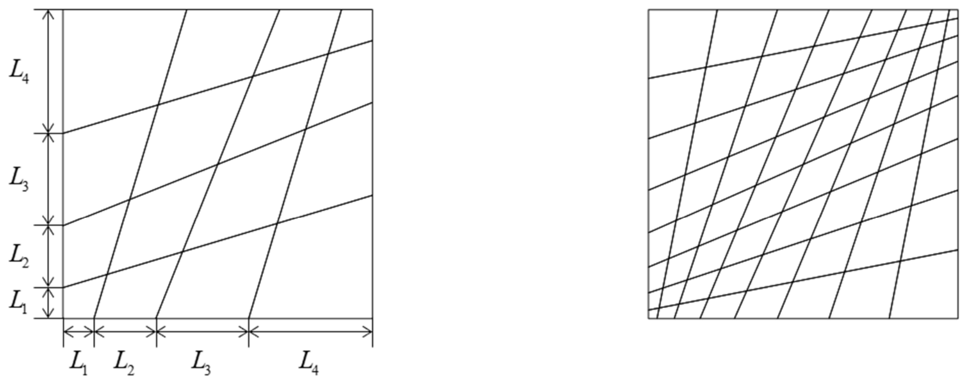

(a) (b)

Fig. 3.11. $N \times N$ distorted mesh patterns with (a) $N = 4$ and (b) $N = 8$.

The mesh patterns are constructed in a square and then, linearly mapped to the problem domain considered. Fig. 3.10 shows a $N \times N$ regular mesh pattern when $N = 4$. Fig. 3.11(a) and Fig. 3.11(b) show the mesh patterns when $N = 4$ and 8, respectively. The ratio of each lines in an edge is $L_1 : L_2 : L_3 : ... : L_N = 1 : 2 : 3 : ... : N$.

For the bending performance of the shell elements, the MITC4, MITC4+, imrpvored MITC4+, and new MITC4+ shell elements are identical when the regular meshes are used, but for the distorted mesh cases, the MITC4 shell element reveal membrane locking. Therefore, all the MITC based 4-node shell elements except the MITC4 shell element would be good enough to used for the bending-domiated problems.

For the membrane performance of the shell elements, the MITC4 and MITC4+ shell elements are identical to each other in both regular and distorted meshes. The MITC4 and MITC4+ shell elements is exatly same with the standard 4-node quadrilateral plane stress element when they are used for the 2D solid problems. The improved MITC4+ and new MITC4+ shell elements become the 2D-MITC4 element when they are employed for the 2D solid problems. In addition, when the distorted meshes are considered, while the imporved MITC4+ deteriorates, but the new MITC4+ performs well due to the geometry dependent Gauss integration scheme.

Note that the shell structures under surface pressure loading show not in-plane bending but in-plane stretching in most cases for the problems enforcing membrane-dominated behavior. Thus, the all elements considered are good enough to used in this cases. However, if the problems have the in-plane bending behavior, the MITC4 and MITC4+ could be seriously locked with revealing overly stiff behavior.

It is not easy to pedict of the shell strucutures until the we try to simulate its response using FEM due to their inherently complex and sensitive behaviors. Therefore, the shell elements should work well in all situations. In short, the proposed element is the best option for general use in shell problems including membrane and bending problmes.

3.5.1. Square plate

The square plate problem [70,76,77] shown in Fig. 3.12 is solved. The dimension of the square is $2L \times 2L$ and uniform thickness is given by t. An uniform pressure is applied to the square plate. Due to the symmetry of the problem, only a one-quarter model is considered. The boundary conditions are $u_x = \alpha = 0$ along BC and $u_y = \beta = 0$ along CD and $u_x = u_y = u_z = \alpha = \beta = 0$ along AB and AD. The convergence behavior is studied considering both regular and distorted meshes shown in Fig. 3.11(a) and Fig. 3.11(b), respectively. The thickness ratios (t/L) are $1/100$, $1/1000$ and $1/10000$.

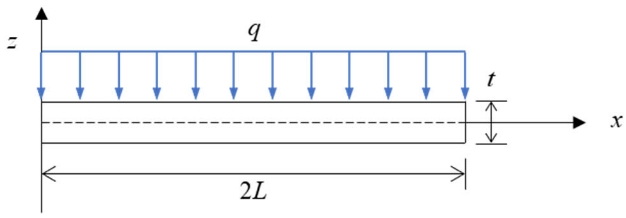

(a)

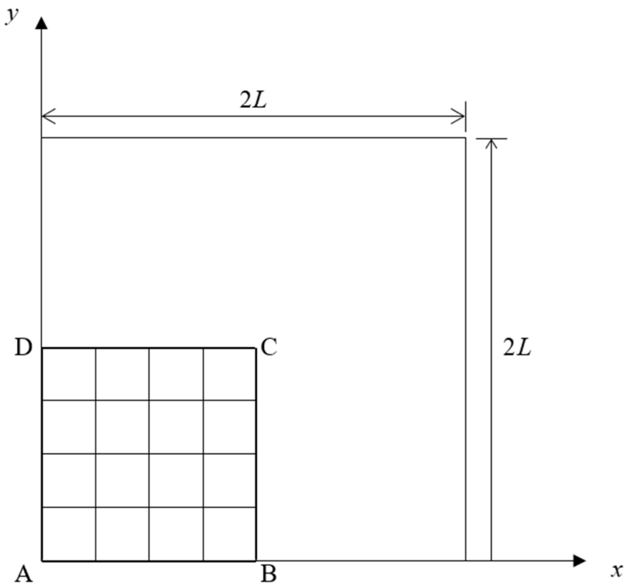

(b)

Fig. 3.12. Descripstion of the square plate problem. (a) Plate subjected to an uniform pressure ($p = 1.0$). (b) Square plate with $E = 1.7472 \times 10^7$, $\nu = 0.3$, and $L = 1.0$.

Fig. 3.13(a) and Fig. 3.13(b) show the convergence curves of the four shell elements for regular and distorted mesh patterns, respectively. A 96×96 element mesh of the MITC9 shell element is employed to obtain the reference solution. $N \times N$ element meshes are used with $N = 4$, 8, 16, 32, and 64 to solve the problem. The element size $h = L / N$ is used in the convergence curves. Note that there is no warped element in both regular and distorted meshes and thus, the membrane locking is not presented in this problem. Therefore, the performance of all elements is uniformly optimal in both regular and distorted meshes.

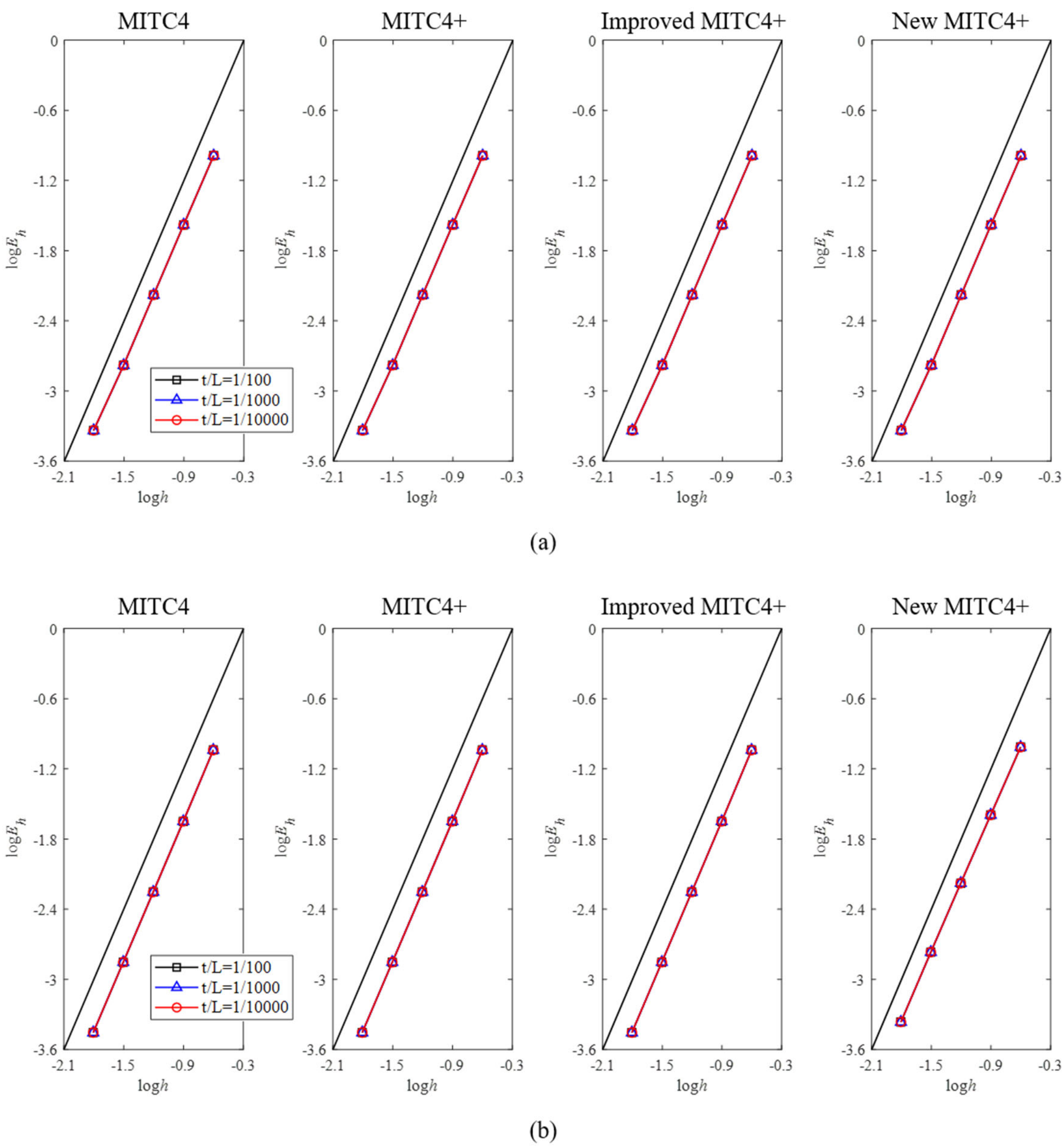

Fig. 3.13. Convergence curves for the square plate problem with fully clamped conditions considering (a) regular meshes and (b) distorted meshes. The bold line denotes the optimal convergence rate.

3.5.2. Cylindrical shell

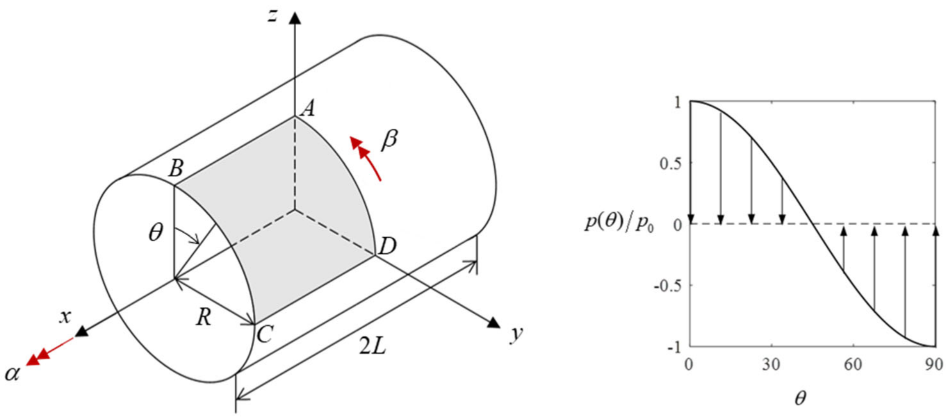

(a) (b)

Fig. 3.14. Description of the cylindrical shell problem. (a) Cylindrical shell subjected to a smoothly varing pressure ($L = R = 1.0$, $E = 2.0\times10^5$, $\nu = 1/3$, and $p_0 = 1.0$). (b) Pressure loading

The cylindrical shell problem subjected to a smoothly varing pressure is considered as shown in Fig. 3.14 [36,78]. The length, radius, and thickness are $2L$, R , and t , repectively. The thickness ratios ($t/L = 1/100$, $1/1000$ and $1/10000$) are considered. Material properties are given by $E = 2.0\times10^5$ and $\nu = 1/3$. As shown in Fig. 3.14(b), the structure is subjected an internal pressure $p(\theta) = p_0 \cos(2\theta)$. The convergence behavior is studied considering both regular and distorted meshes shown in Fig. 3.15, respectively.

(a) (b)

Fig. 3.15. $N\times N$ element mesh with (a) regular and (b) distorted mesh patterns when $N = 4$.

The cylindrical shell structure shows different asymptotic behaviors depending on the boundary conditions at both ends. The membrane-dominated behavior occurs when both ends are clamped and the bending-dominated behavior is obtained when both ends are free. Based on the symmetry of the problem, only one-eighth of the cylindrical shell structure is modeled. For the clamed boundary conditions, $u_y = \alpha = 0$ along AB, $u_z = \alpha = 0$ along CD, $u_x = \beta = 0$ along AD, and $u_x = u_y = u_z = \alpha = \beta = 0$ along BC. For the free boundary conditions, $u_y = \alpha = 0$ along AB, $u_z = \alpha = 0$ along CD, and $u_x = \beta = 0$ along AD. The convergence is studied in both regular and distorted meshes about four shell elements.

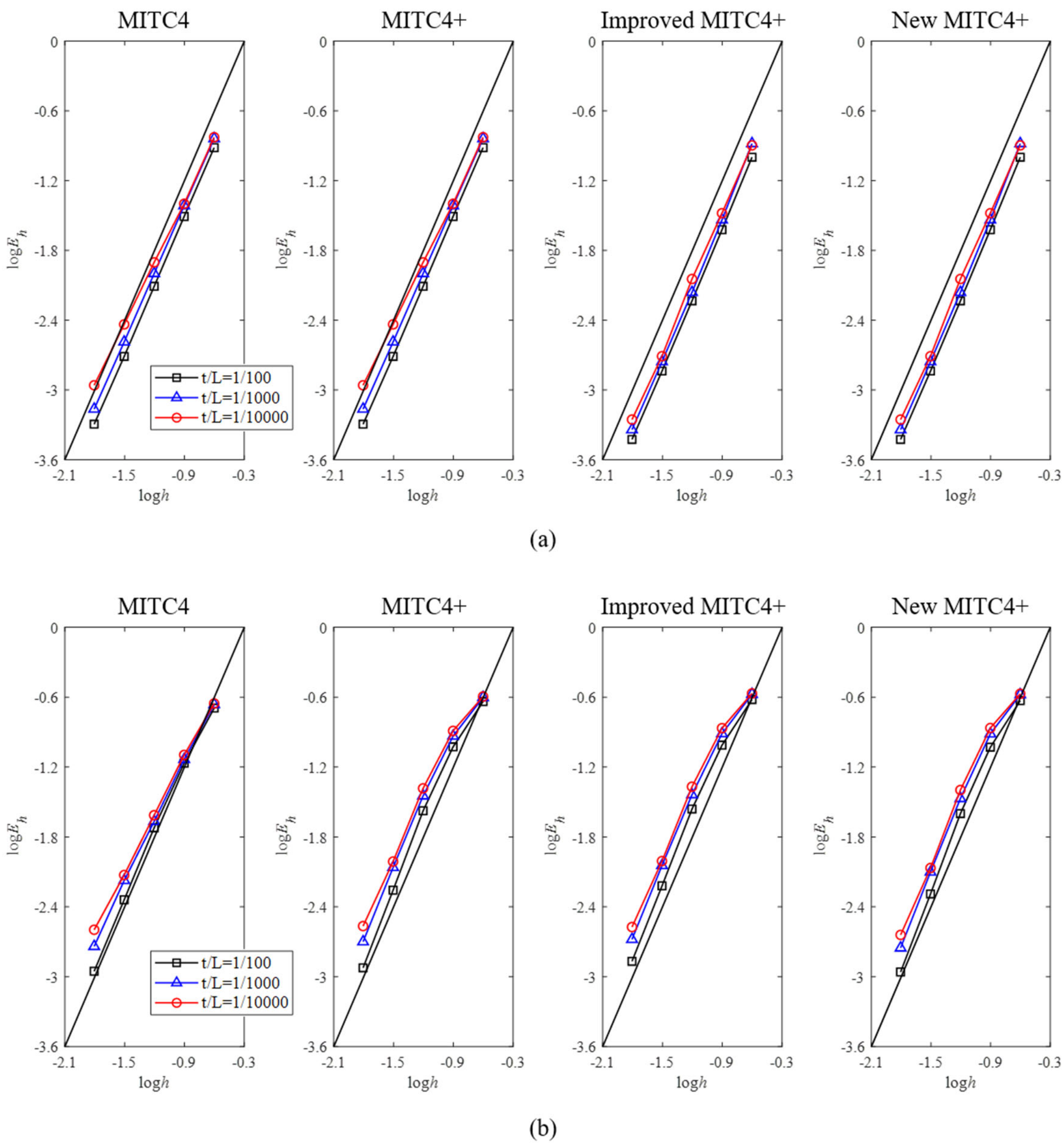

Fig. 3.16. Convergence curves for the cylindrical shell problem with fully clamped conditions considering (a) regular meshes and (b) distorted meshes. The bold line denotes the optimal convergence rate.

Fig. 3.16 show the convergence curves for the cylindrical shell problem considering clamped and free boundary conditions, repectively. A 96×96 element mesh of the MITC9 shell element is employed to obtain the reference solution. $N \times N$ element meshes are used with $N = 4$, 8, 16, 32, and 64 to solve the problem. The element size $h = L / N$ is used in the convergence curves. Note that all elements considered perform well in both clamped and free boundary conditions using regular meshes. However, for the free boundary condition with distorted meshes, the MITC4 shell element reveal membrane locking and thus its convergence rate become worse. For the MITC4+, improved MITC4+, and new MITC4+ shell elements give accurate solutions in similar to each other.

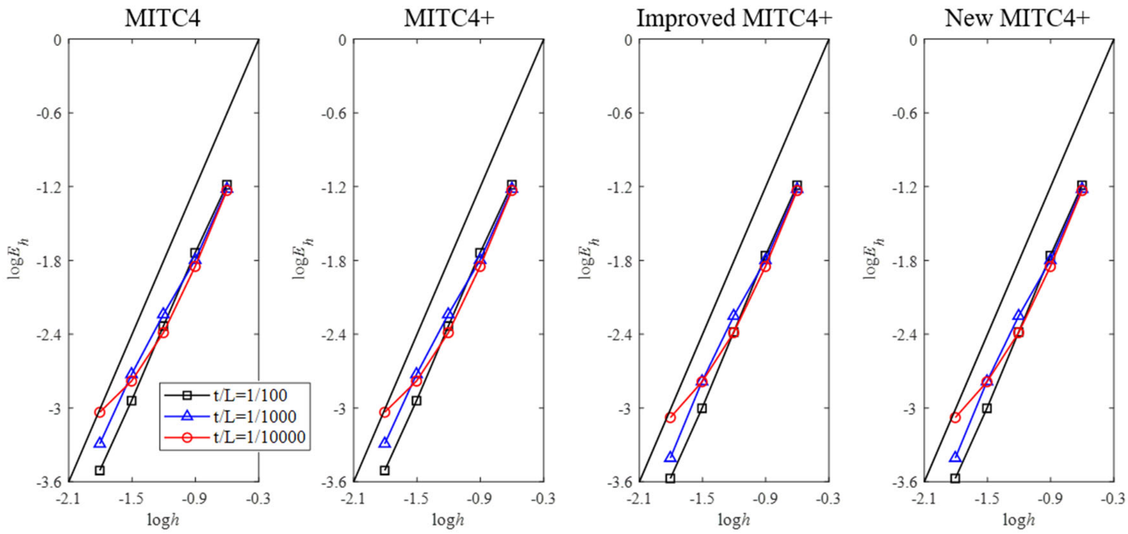

(a)

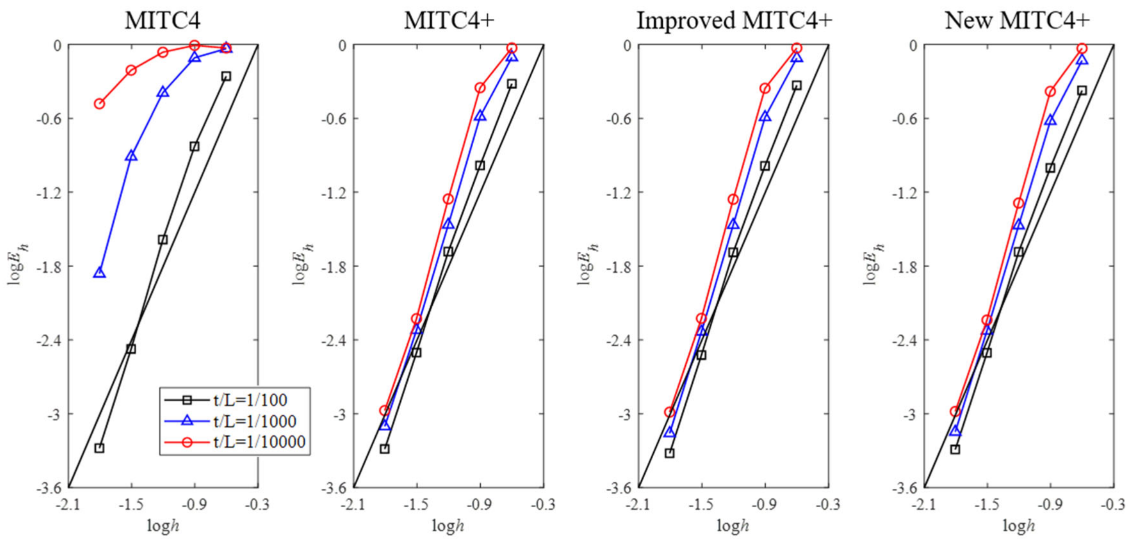

(b)

Fig. 3.17. Convergence curves for the cylindrical shell problem with free conditions considering (a) regular meshes and (b) distorted meshes. The bold line denotes the optimal convergence rate.

3.5.3. Hyperboloid shell

The hyperboloid shell problem under a internal pressure is considered as shown in Fig. 3.18 [78,79]. The mid-surface of the shell structure is given by

$x^2 + z^2 = 1 + y^2$, $y \in [-1,1]$.

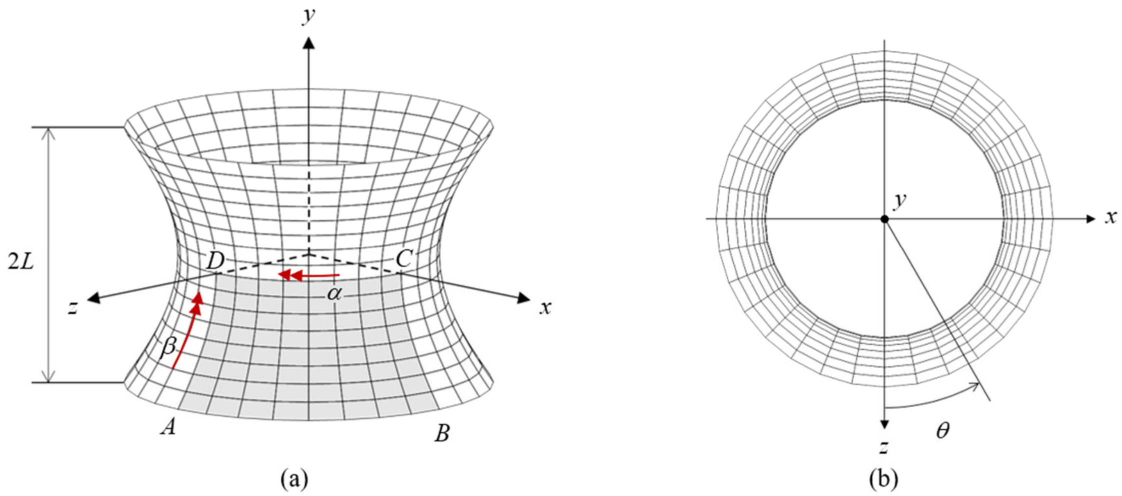

Fig. 3.18. Description of the hyperboloid shell problem. (a) hyperboloid shell ($L = 1.0$, $E = 2.0 \times 10^{11}$, and $\nu = 1/3$). (b) Smoothly varing pressure loading ($p_0 = 1.0$).

The shell structure is subjectied a smoothly varing pressure $p(\theta) = p_0 \cos(2\theta)$, seen in Fig. 3.18(b), and the material properties are given by Young's moduluss $E = 2.0 \times 10^{11}$ and Poisson's ratio $\nu = 1/3$. Similar to the cylindrical shell problem, the hyperboloid shell also shows two different asymptotic behaviors depending on the boundary conditions at both end tips. It reveals the membrane-dominated behavior or the bending-dominated behavior under the clamped or free boundary conditions, repectively.

Due to the symmetry of the problem, only one-eighth of the shell structure is considered. The clamped boundary conditions are given as $u_x = \beta = 0$ along AD, $u_z = \beta = 0$ along BC, $u_y = \alpha = 0$ along CD, and $u_x = u_y = u_z = \alpha = \beta = 0$ along AB. The free boundardy conditions are given as $u_x = \beta = 0$ along AD, $u_z = \beta = 0$ along BC, and $u_y = \alpha = 0$ along CD.

To investigate the convergence using the s-norm, the regular and distorted mesh patterns is considered in Fig. 3.19(a) and Fig. 3.19(b), repectively. For the thickness ratios (t/L), three values ($1/100$, $1/1000$ and $1/10000$) are used. Finite element solutions are obtained unsing $N \times N$ element meshes with $N = 4$, 8, 16, 32 and 64. The reference solutions are obtained by using a 96×96 element mesh of the MITC9 shell element. The element size $h = L/N$ is used in the convergence curves.

(a) (b)

Fig. 3.19. $N \times N$ element mesh with (a) regular and (b) distorted mesh patterns when $N = 8$.

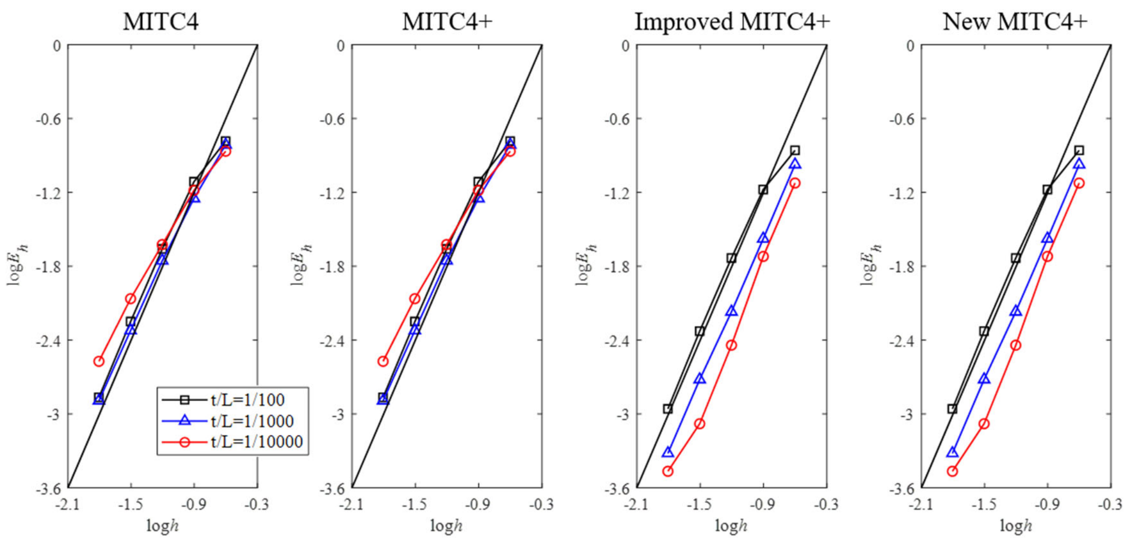

(a)

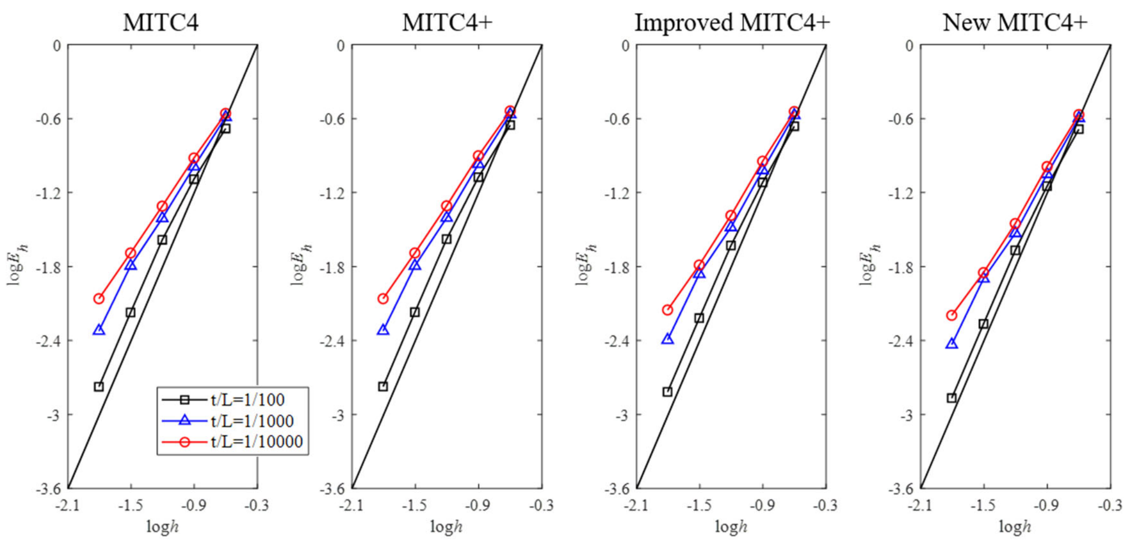

(b)

Fig. 3.20. Convergence curves for the hyperboloid shell problem with fully clamped conditions considering (a) regular meshes and (b) distorted meshes. The bold line denotes the optimal convergence rate.

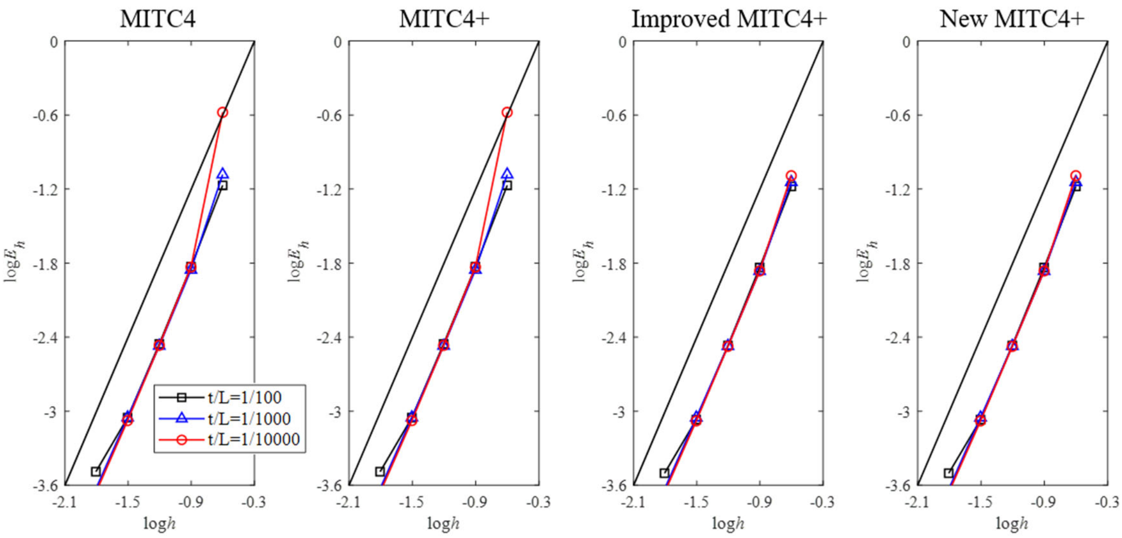

(a)

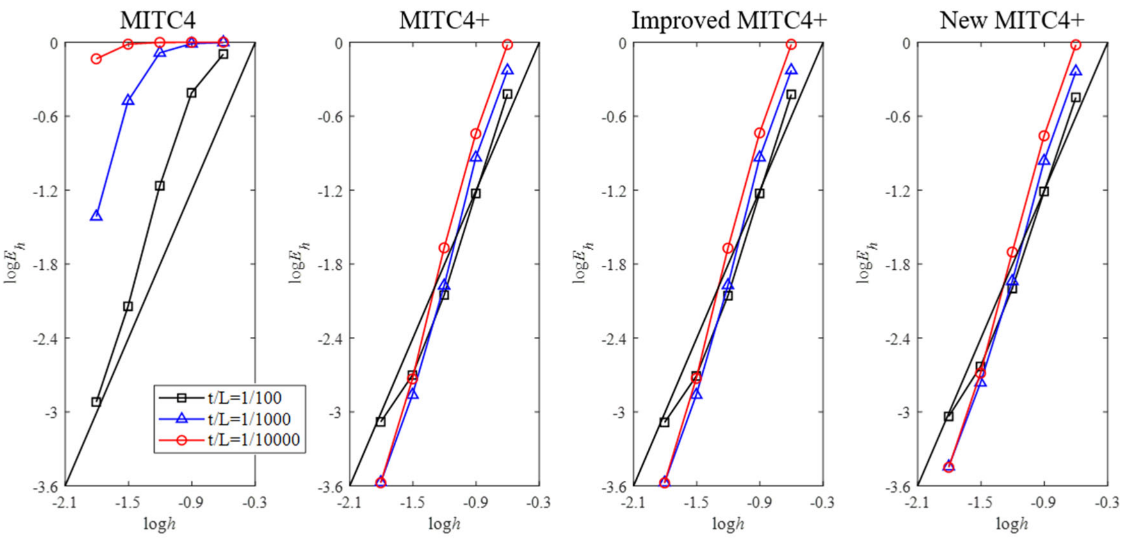

(b)

Fig. 3.21. Convergence curves for the hyperboloid shell problem with free conditions considering (a) regular meshes and (b) distorted meshes. The bold line denotes the optimal convergence rate.

The convergence curves for the clamped hyperboloid shell with regular and distorted meshes are given in Fig. 3.20. In addition, the convergence curves for the free hyperboloid shell with regular and distorted meshes are given in Fig. 3.21. It is difficult to obtain accurate solutions in this problem because the hyperboloid shell has a doubly curved geometry with negative Gauss curvature. In both clamped and free boundary conditions with regular meshes, all elements give accurate solutions. However, when the distorted meshes are employed, the improved MITC4+ and new MITC4+ shell elements perform slightly better than the others.

3.5.4. Scordelis-Lo roof

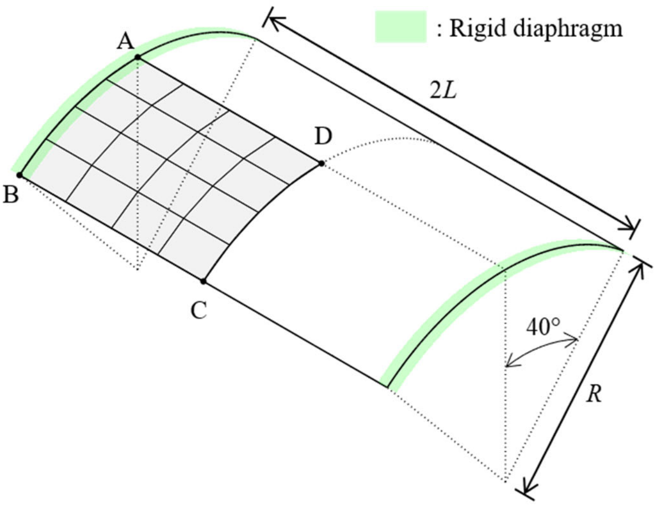

Fig. 3.22. Description of the Scordelis-Lo roof problem ($L = R = 25.0$, $E = 4.32 \times 10^8$, $\nu = 0.0$, and self-weight is 90 per unit area) with 4×4 regular mesh.

The Scordelis-Lo roof problem shown in Fig. 3.22 is considered [80,81]. The structure is a part of a cylinder with length $L = 25.0$, radius $R = 25.0$, and uniform thickness t . The roof is subjected to a self-weight loading $f_z = -90$ per unit area. Young's modulus $E = 4.32 \times 10^8$ and Poisson's ratio $\nu = 0.0$ are used. The rigid diaphragm boundary conditions are given at both ends of the structure. The convergenc is investigated by considering regular and two distorted mesh patterns shown in Fig. 3.23. The Scordelis-Lo roof is known to show bending and membrane mixed behavior [83], and thus it behaves very sensitive depending on the element thickness.

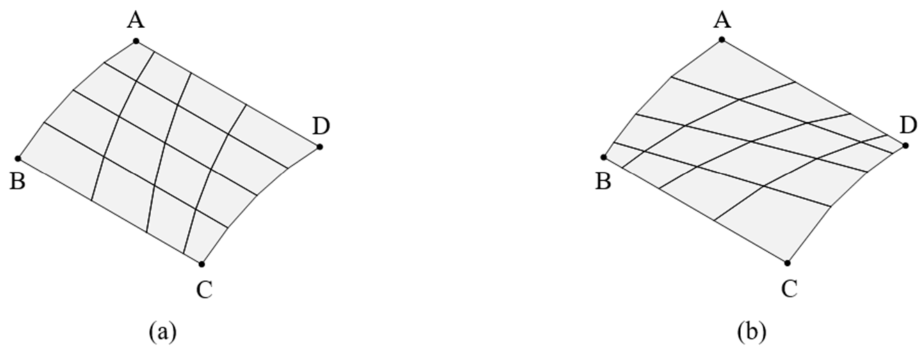

Fig. 3.23. $N \times N$ distorted mesh patterns with (a) distorted I and (b) distorted II when $N = 4$.

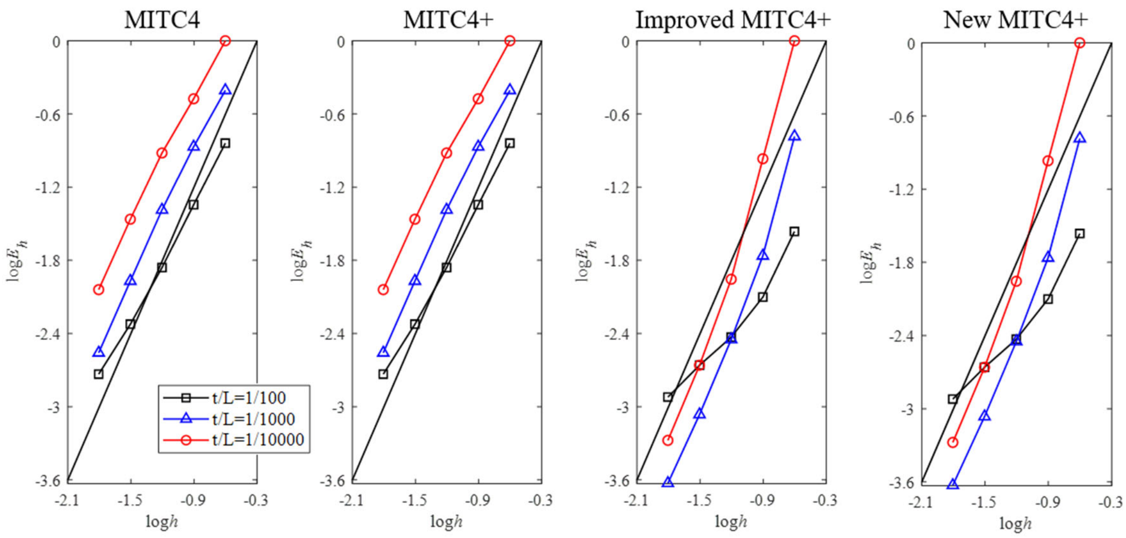

Fig. 3.24. Convergence curves for the Scordelis-Lo roof problem with rigid diaphragm conditions considering regular mesh patterns. The bold line denotes the optimal convergence rate.

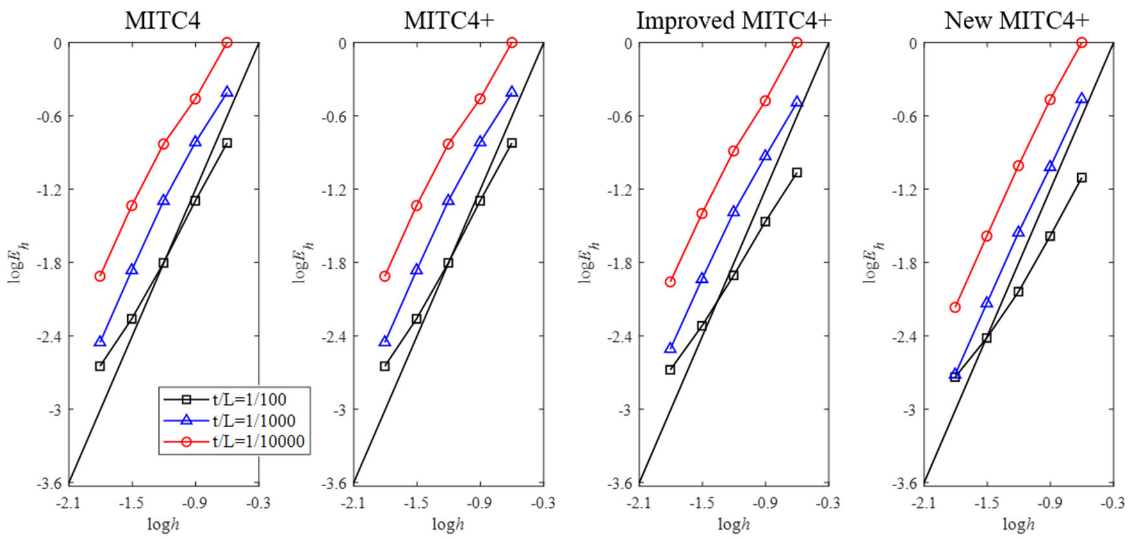

Fig. 3.25. Convergence curves for the Scordelis-Lo roof problem with rigid diaphragm conditions considering distorted mesh patterns (distorted I). The bold line denotes the optimal convergence rate.

Due to the symmetry of the problem cosidered, only one-quarter of the structure corresponding the region ABCD in Fig. 3.22 is modeled for the analysis. $u_x = \beta = 0$ along AD, $u_y = \alpha = 0$ along CD, and $u_x = u_z = 0$ along AB are considered for the rigid diaphragm boundary conditions. Finite element solutions are obtained considering three mesh patterns depending to the thickness ratios ($t/L = 1/100$, $1/1000$ and $1/10000$). For the all mesh patterns, the $N \times N$ element meshes with $N = 4$, 8, 16, 32 and 64 are used.

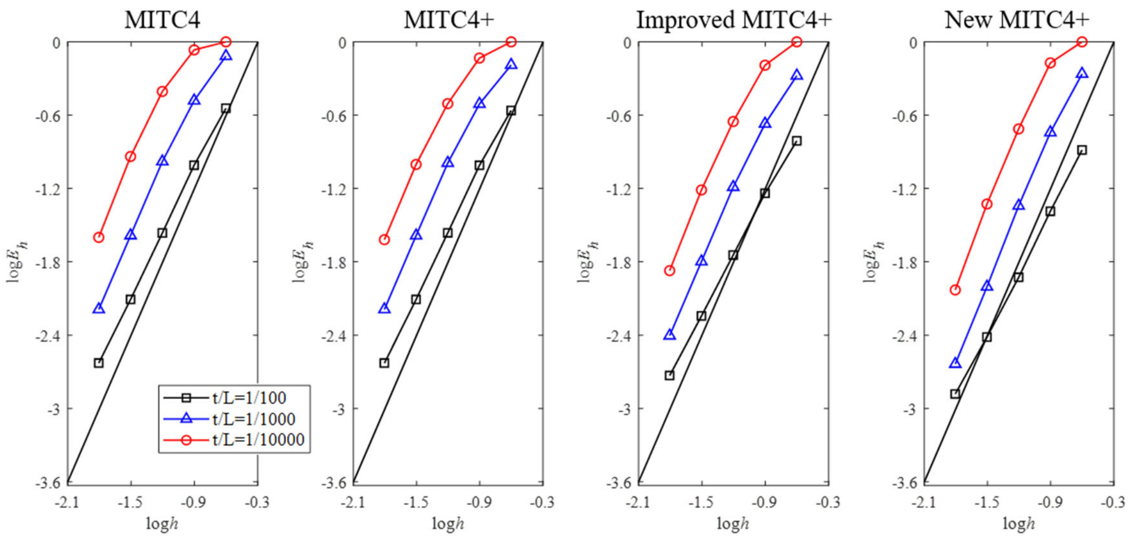

Fig. 3.26. Convergence curves for the Scordelis-Lo roof problem with rigid diaphragm conditions considering distorted mesh patterns (distorted II). The bold line denotes the optimal convergence rate.

For the regular mesh case, the improved MITC4+ and new MITC4+ shell elements give more accurate solutions than the others. Note that the performance of the two element is almost equal to each other. This is because the membrane performance is quite similar when the element is not distorted. However, when considering the distorted meshes with distorted mesh pattern I and II, the new MITC4+ shell element give the most accurate solutions. The incresement in the accuracy is not that much because the Scordelis-Lo roof undergo the membrane and bending mixed behavior. Since the bending performance of the new MITC4+ shell element is nearly same to the improved MITC4+ shell element, the performance increament is relatively small.

3.5.5. Hyperbolic cylinder shell

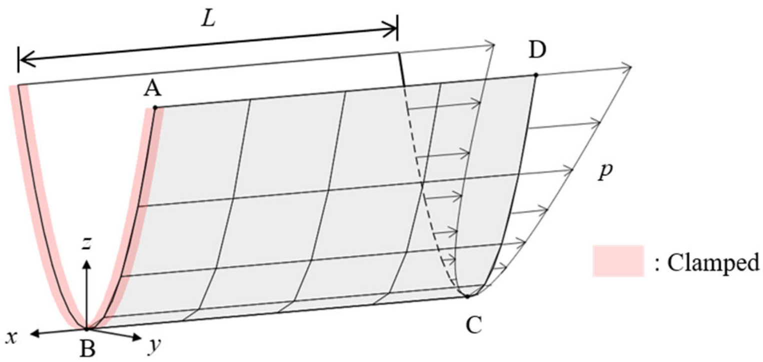

(a)

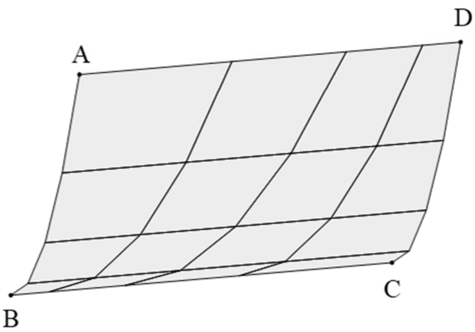

(b)

Fig. 3.27. Description of the hyperbolic cylinder shell problem ($L = 2$, $E = 2.0\times10^{11}$, and $\nu = 1/3$). (a) Problem discriptions with 4×4 regular mesh. (b) 4×4 distorted mesh.

As shown in Fig. 3.27, the hyperbolic cylinder shell problem is considered. The structure is clamped at its one side and subjected to a distributed line force $p_x = -z$ (force per length) at the other side. For the dimension of the structure, the length is $L = 2$ and the mid-surface of the structure is given by

$z = 4y^2$, $y \in [0, 0.5]$.

The material properties are given with Young' s modulus $E = 2.0\times10^{11}$ and Poisson's ratio $\nu = 1/3$. The convergence is studied based on the relative errors in the strain energy by considering thre different thickness to length ratios: $t/L = 1/100$, $1/1000$ and $1/10000$. The regular and distorted mesh patterns are employed, as shown in Fig. 3.27(a) and Fig. 3.27(b). Based on the symmetry, only half of the problem domain is modeled to analysis. The following boundary conditions are considered: $u_y = \alpha = 0$ along BC and $u_x = u_y = u_z = \alpha = \beta = 0$ along AB.

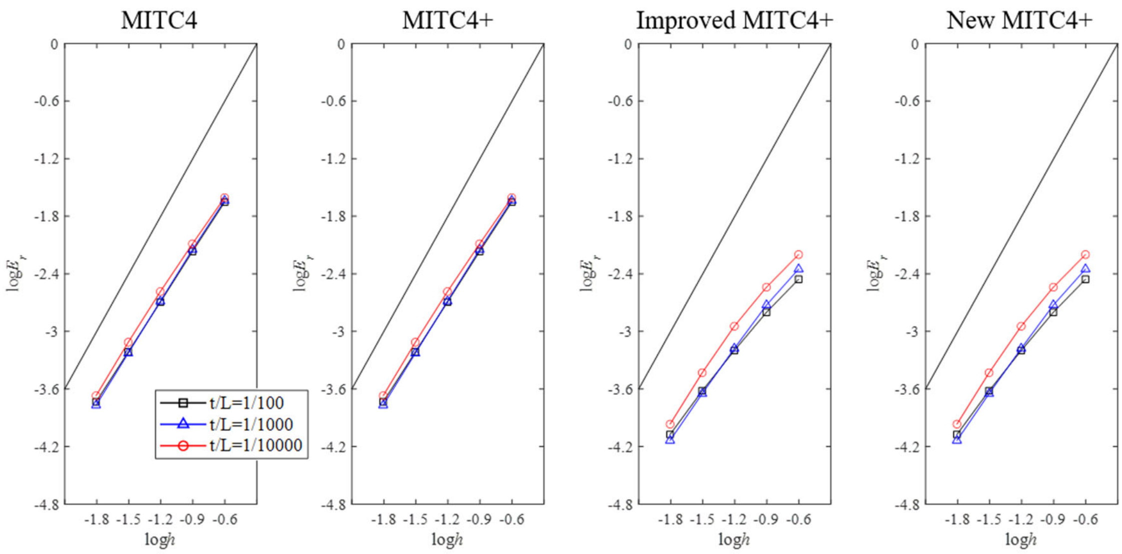

(a)

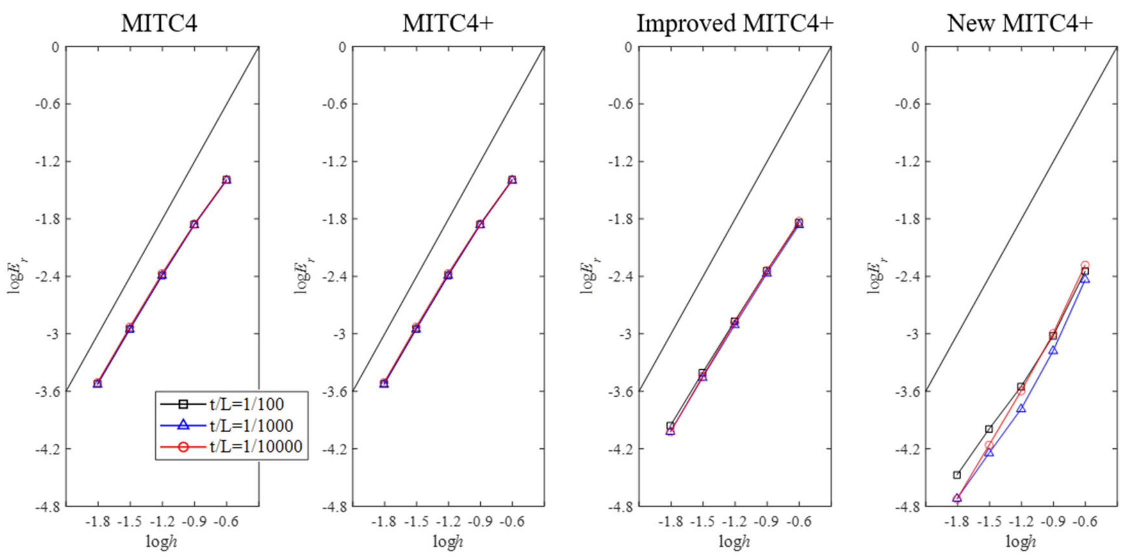

(b)

Fig. 3.28. Convergence curves for the hyperbolic cylinder shell problem with partly clamped conditions considering (a) regular meshes and (b) distorted meshes. The bold line denotes the optimal convergence rate.

Fig. 3.28(a) and Fig. 3.28(b) shows the convergence curves of the partly clamped hyperbolic cylinder shell problem considering regular and disorted mesh patterns, repectively. $N \times N$ element meshes are used with N = 4, 8, 16, 32, and 64 to solve the problem. The reference solutions are obtained by using a 72×72 element mesh of the MITC9 shell element. The element size $h = 1/N$ is used in the convergence curves. This problem is the membrane-dominated problem. More specifically, the shell element undergo the in-plane bending deformation. The improved MITC4+ and new MITC4+ shell elements give more accurate solutions considering regular meshes, but for the distorted meshes, the new MITC4+ shell element give the most accurate solutions.

3.6. Numerical examples for nonlinear analysis

Through the results of linear analysis, it has been verified that the new MITC4+ shell element shows higher accuracy than other elements especially in the membrane-dominated behavior. To assess the performance of the new MITC4+ shell finite element in goemertrically nonlinear analysis including large displacement and large rotation, the following shell problems are considered: a thin curved beam [5,47], a slit annular plate [82,84], and a hemispherical shell problems [82,85]. Here, the results of the new MITC4+ shell element are compared with the results from the MITC4 and MITC4+ shell element, since the improved MITC4+ shell element has not been extended to geometrically nonlinear analysis. The features of the elements are briefly organized in Table 3.4.

In each example, the reference solutions are obtained by using a MITC9 shell element with a fine regular mesh. The MITC9 shell element is known to satisfy the ellipticity and consistency conditions and to show good convergence behavior in both linear and nolinear analysis [32]. The Newtown-Raphson method is used to solve the nonlinear equations at evergy load step with a acceptable tolerance of 0.1 percent of the relative incremental evergy. For comparison purposes, translational displacement at specific points and deformed configurations are obtained at several load steps. In addition, both the regular and distorted mesh patterns are considered to investigate whether the performance is improved.

Note that in the problems that the bending behavior is important, all the three elements considered work well when regular meshes and the membrane locking is inherently not induced in the problems but the MITC4 shell element reveals stiff behavior when distorted meshes are used and then the membrane locking occurs. In the problem that membrane behavior is important, the new MITC4+ shell element is more accurate than the MITC4 and MITC4+ shell elements since the membrane strain field of the two elements are identical to the standard 4-node quadrilateral solid element.

Table 3.4. Considered shell elements and characteristics.

	Transverse shear locking	Membrane locking	Membrane performance	Linear analysis	Nonlinear analysis
MITC4	O	X	Standard Q4	O	O
MITC4+	O	O	Standard Q4	O	O
Improved MITC4+	O	O	Improved 2D-MITC4	O	X
New MITC4+	O	O	New 2D-MITC4	O	O

3.6.1. Thin curved beam

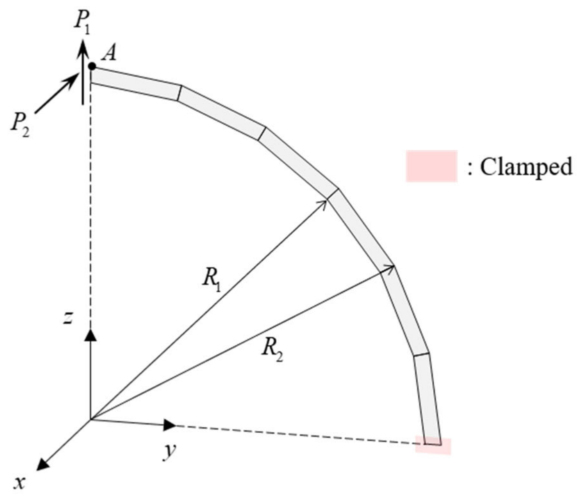

Fig. 3.29. Description of the thin curved beam problem ($R_1 = 4.12$, $R_2 = 4.32$, $t = 0.1$, $E = 1.0 \times 10^7$, $\nu = 0.25$, and $P_1 = P_2 = 100$) with 1×6 regular mesh.

A thin curved beam shown in Fig. 3.29 is considered [5, 47]. The beam is clamped at one end and subjected to two forces P_1 and P_2 in the z and -x driections, respectively. The material properties are given by Young's modulus $E = 1.0 \times 10^7$ and Poisson's ratio $\nu = 0.25$. The thickness of the beam is $t = 0.1$. The curved beam is modeled by using 1×6 regular mesh of the MITC4, MITC4+ and new MITC4+ shell elements. The reference solution is obtained by using the MITC9 shell element with 2×12 elements regular mesh.

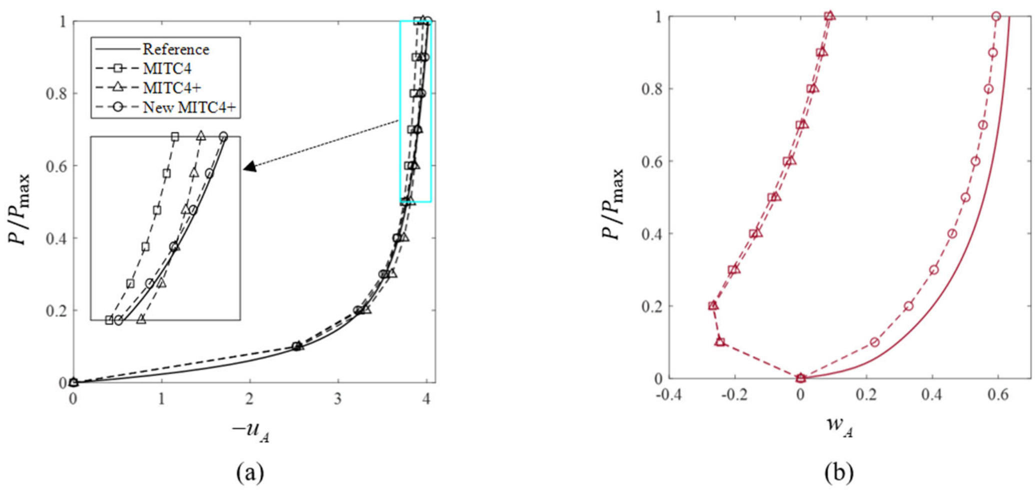

Fig. 3.30. Load-displacement curves of the thin curved beam problem for (a) $-u_A$ and (b) w_A .

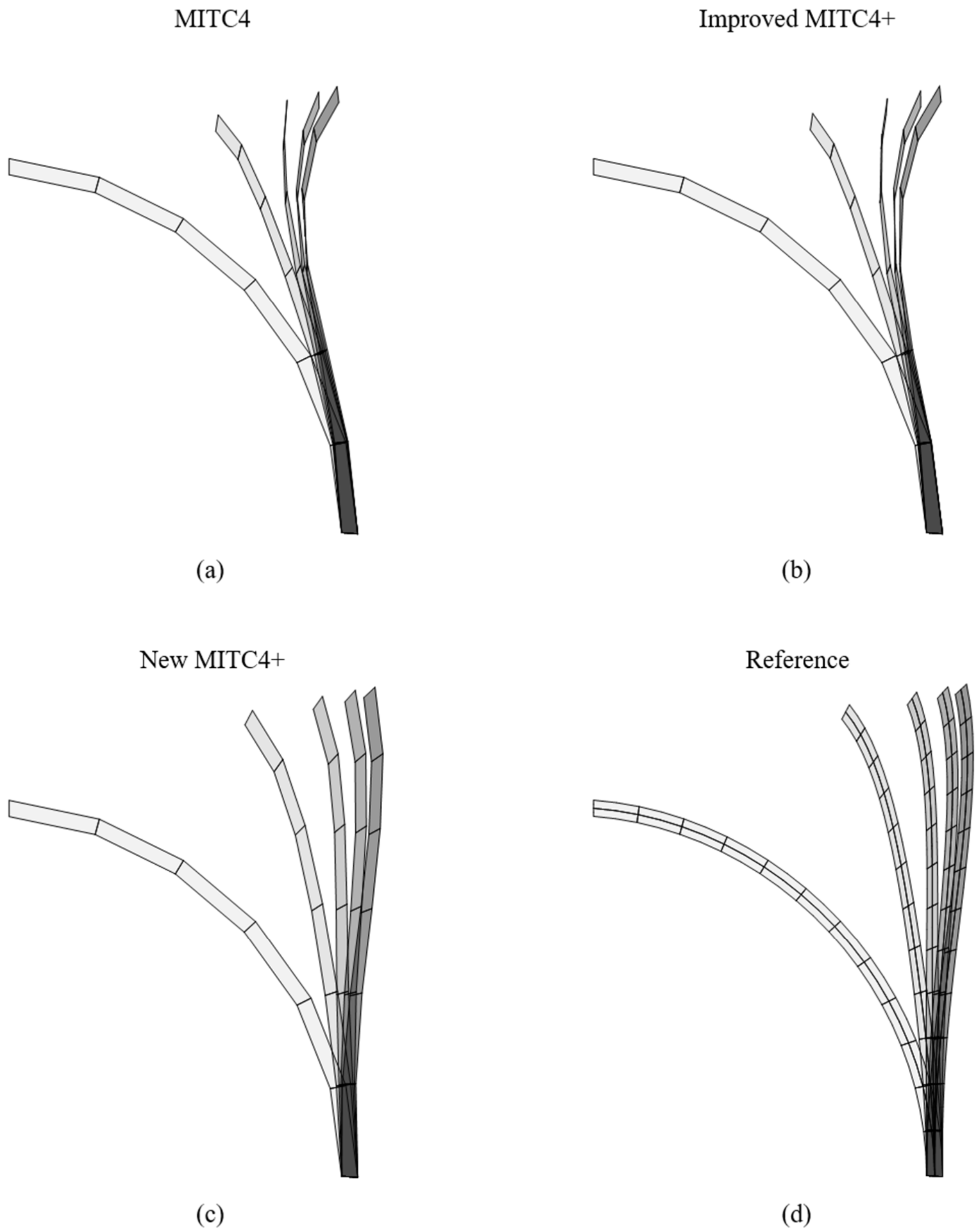

Fig. 3.31. Deformed configurations of the thin curved beam problem at several load steps with (a) MITC4, (b) MITC4+ and (c) new MITC4+ elements. (d) The reference solution with MITC9 element.

Fig. 3.30 gives the load-displacement curves at the point A for the thin curved beam. In the z-directional displacement, the three element the new MITC4+ shell element work well, but for the verical displacement, the MITC4 and MITC4+ shell elements reveal much stiff behavior. In addition, Fig. 3.31 shows the initial configurations and the deformed configurations at the load steps $P = 0.25P_{\max}$, $0.5P_{\max}$, $0.75P_{\max}$ and $P_{\max}$. While both the MITC4 and MITC4+ shell elements show totally differenct final deformed cofigurations compared with the reference solution, but the deformed configuration of the new MITC4+ element is very close to the reference solution.

3.6.2. Slit annular plate

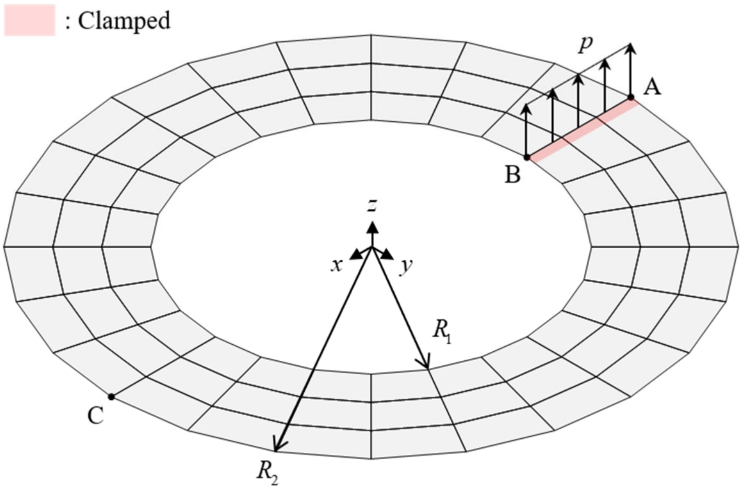

(a)

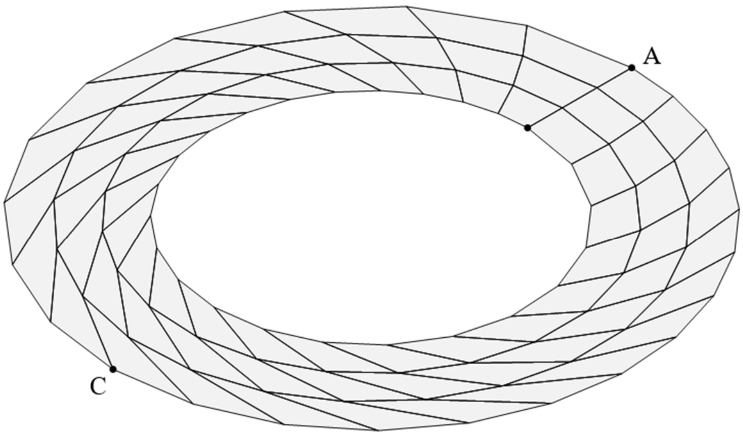

(b)

Fig. 3.32. Description of the slit annular plate problem ($R_1 = 6$, $R_2 = 10$, $t = 0.03$, $E = 2.1\times10^7$, $\nu = 0$ and $p = 0.8$) with 3×24 (a) regular and (b) distorted meshes.

As shown in Fig. 3.32, the slit annular plate is clamped at one side and sujected to vertical distributed load $p = 0.8$ (force per length) at the other free end [82,84]. For the material properties, Young's modulus $E = 2.1\times10^7$ and Poisson's ratio $\nu = 0$ are used. The thickness of the structure is $t = 0.03$. The results are obtained by using the MITC4, MITC4+ and new MITC4+ shell elements considering both 3×24 regular and distortred meshes. The distorted mesh pattern is depicted in Fig. 3.32(b).

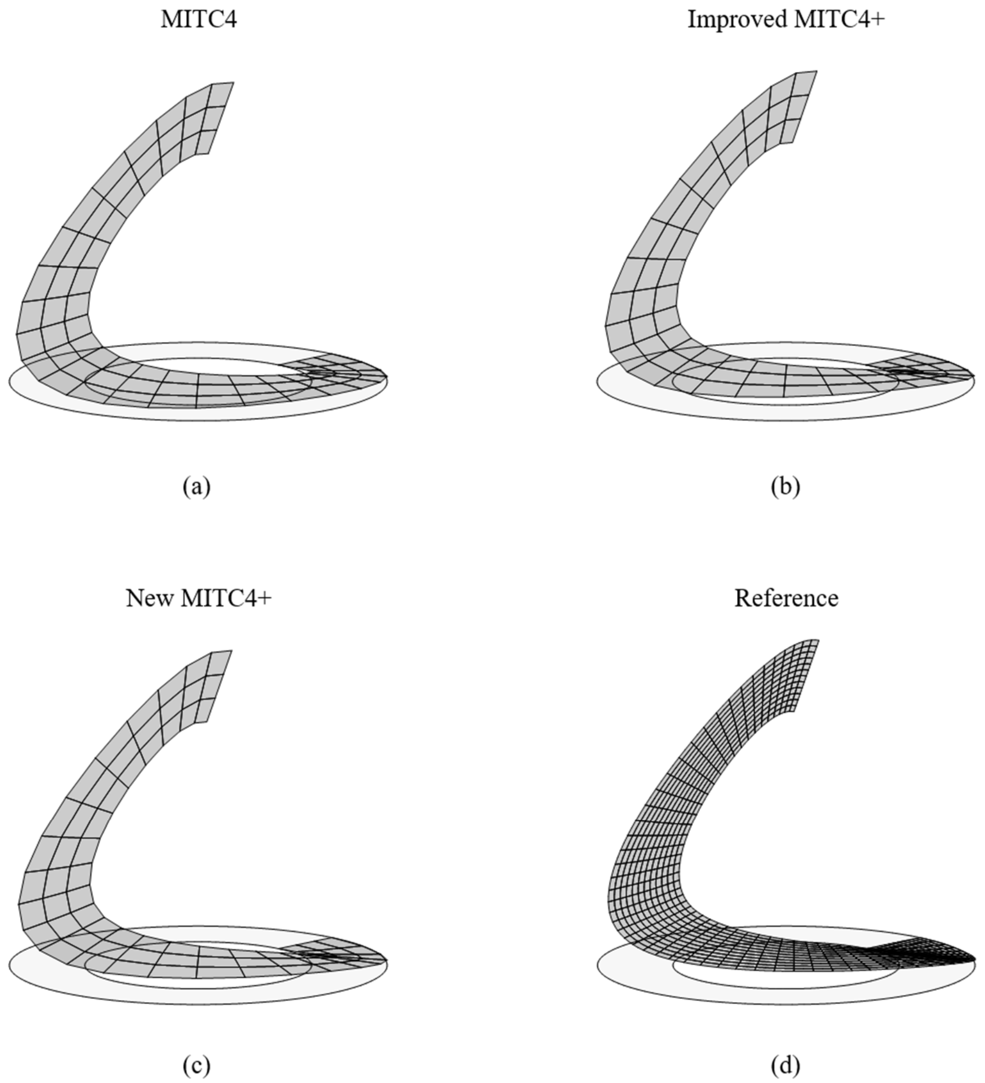

Fig. 3.33. Deformed configurations of the slit annular plate problem considering 3×24 regular mesh of (a) MITC4, (b) MITC4+ and (c) new MITC4+ elements. (d) The reference solution with MITC9 element.

Fig. 3.33 and Fig. 3.34 show the final deformed configurations considering the 3×24 regular and distorted meshes, respectively. The load-displacment curves at the point *A* and *C* are also given in Fig. 3.35 and Fig. 3.36 for the regular and distorted meshes. While all the elements considered seem to work well when the regular mesh is used, amon them, the new MITC4+ shell element is more close to the reference solution. For the disroted mesh case, the MITC4 and MITC4+ shell element show overly stiff behavior and thus the results are differenct compared to the reference solution. However, the new MITC4+ shell element show excellent performance even in when the distorted mesh is employed.

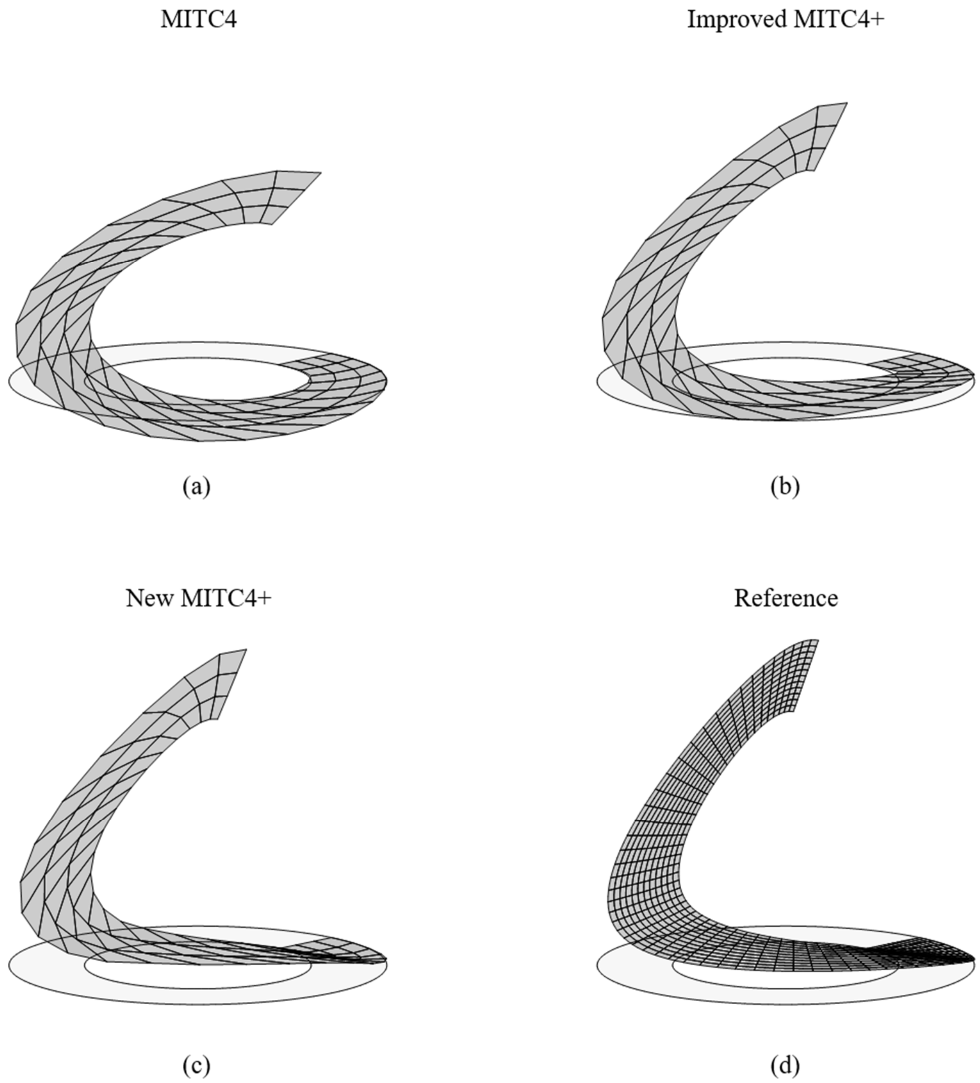

Fig. 3.34. Deformed configurations of the slit annular plate problem considering 3×24 distorted mesh of (a) MITC4, (b) MITC4+ and (c) new MITC4+ elements. (d) The reference solution with MITC9 element.

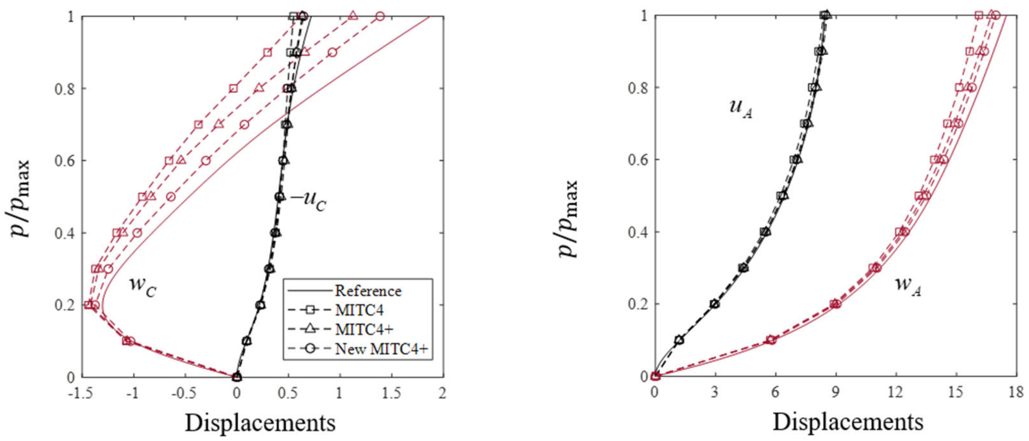

(a) (b)

Fig. 3.35. Load-displacement curves of the slit annular plate problem with 3×24 regular mesh at the points (a) C and (b) A.

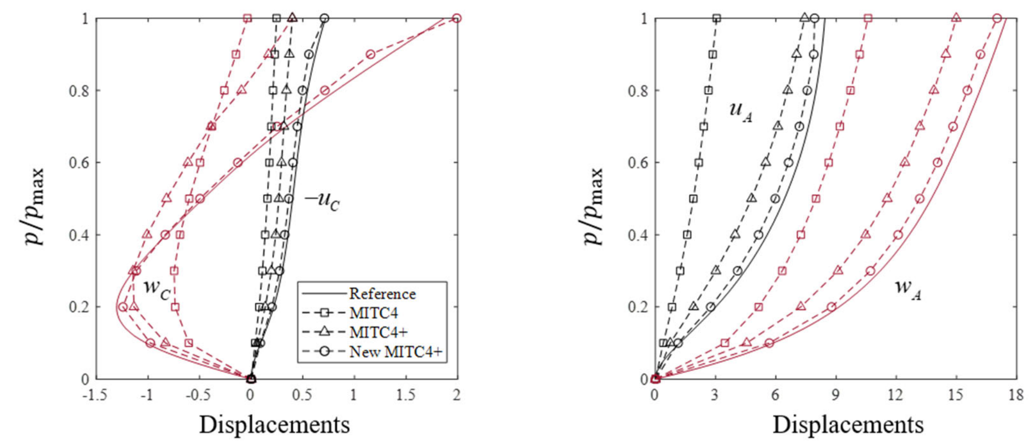

(a) (b)

Fig. 3.36. Load-displacement curves of the slit annular plate problem with 3×24 distorted mesh at the points (a) C and (b) A.

3.6.3. Hemispherical shell

The geometry of the hemispherical shell is given at Fig. 3.37 [82,85]. The hemispherical shell has an $18°$ hole at the top side and is subjected to two pairs of opposite radial concentrated loads $P = 400$. This problem is widely used to investigate whether the element can represent the rigid body roations well and the inextensible bending modes. The following material properties are used: Young's modulus $E = 6.825 \times 10^7$ and Poisson's ratio $\nu = 0.3$. To assess of the performance of the elements, two mesh patterns are considerd including not only the regular mesh but also the distorted mesh seen in Fig. 3.37(b).

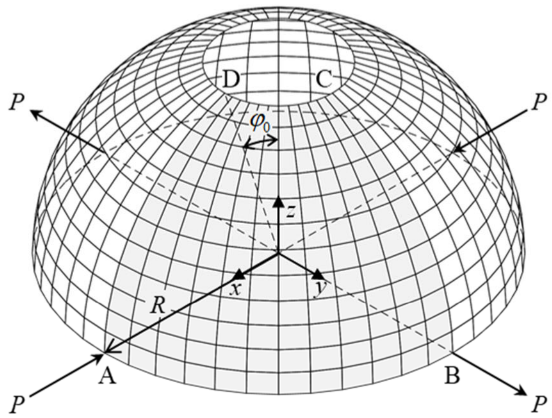

(a)

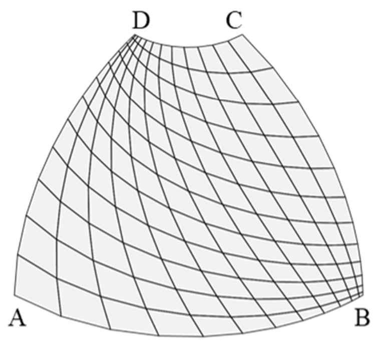

(b)

Fig. 3.37. Description of the hemispherical shell problem ($R = 10$, $\varphi_0 = 18°$, $t = 0.04$, $E = 6.825 \times 10^7$, $\nu = 0.3$, $P = 400$) with 12×12 (a) regular and (b) distorted meshes.

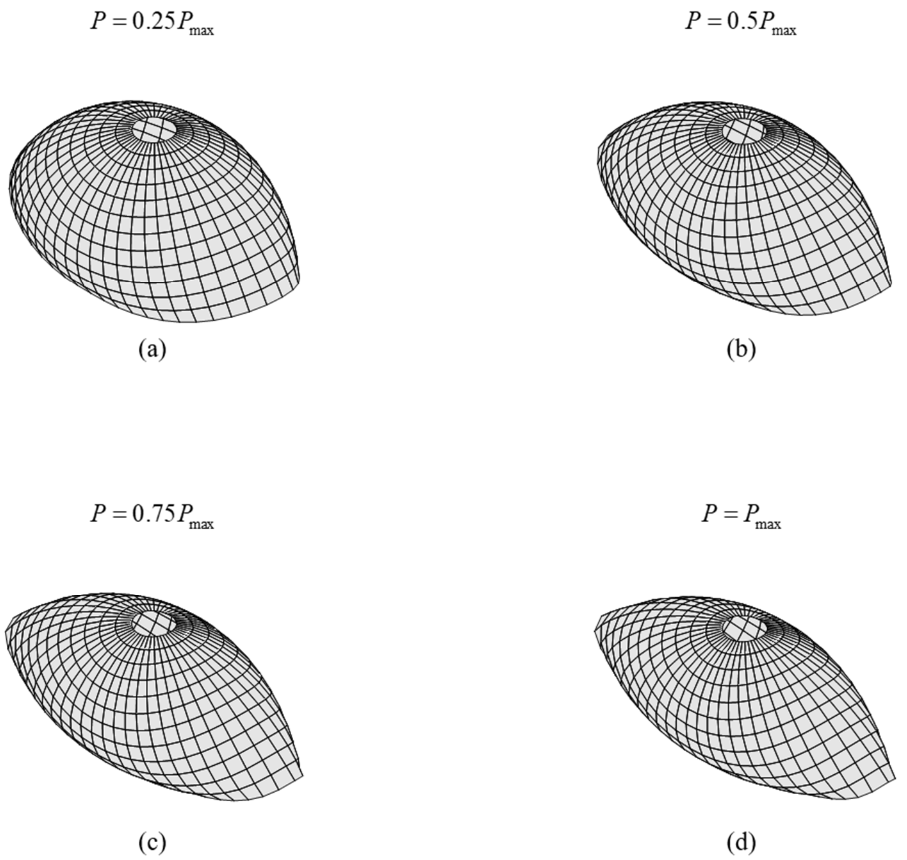

Fig. 3.38. Deformed configurations of the hemispherical shell problem using the 12×12 regular mesh of the new MITC4+ shell element at the load steps of (a) $P = 0.25P_{\max}$, (b) $P = 0.5P_{\max}$, (c) $P = 0.75P_{\max}$ and (d) $P = P_{\max}$.

Based on the symmetry of the problem, only one-quarter model is constructured which is denoted as the region ABCD in Fig. 3.37 with 12×12 elements mesh of the MITC4, MITC4+ and new MITC4+ shell elemet. For the boundary conditions, $u_y = \alpha = 0$ along AD, $u_x = \beta = 0$ along BC, and u_z =0 at point A is considered. To obtain the reference solution, the MITC9 shell element with a 36×36 regular mesh is employed. The deformed configurations at several load steps and the load-displacement curves at the points A and B is compared with the reference solutions.

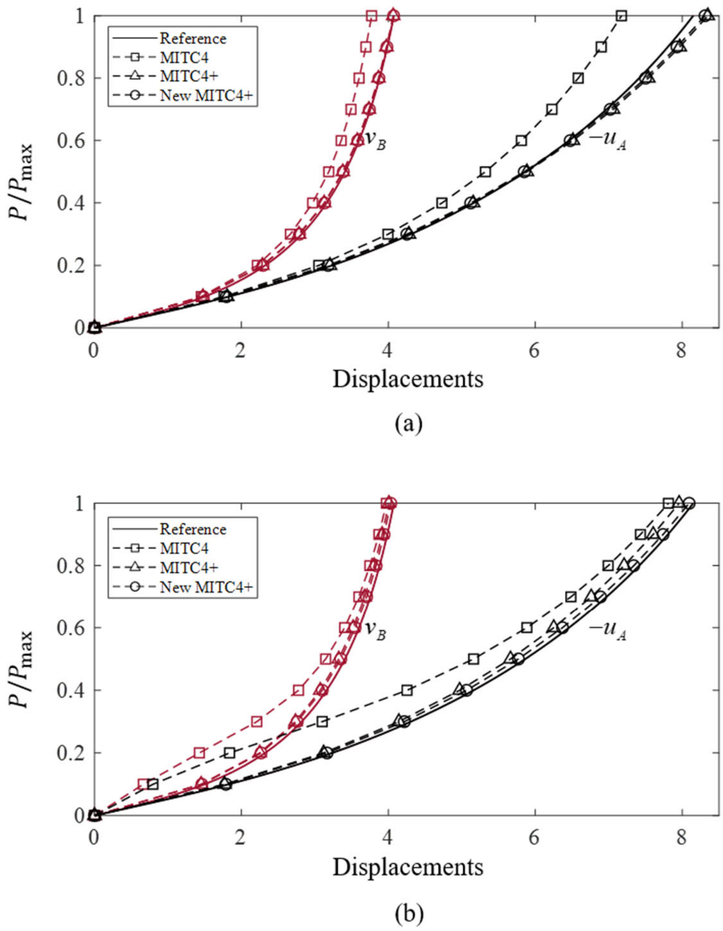

Fig. 3.39. Load-displacement curves of the hemispherical shell problem at the point A and B with 12×12 (a) regular and (b) distorted mesh.

For the new MITC4+ shell element with 12×12 regular mesh case, the deformed configurations at specific load steps with $P/P_{\max}$ =0.25, 0.5, 0.75, and 1 are given in Fig. 3.38. The deformed configurations for the other elements could be found in refs [38,84]. Even in the regular mesh case, the MITC4 shell element is less deformed. While the final deformed configurations from the results of all elements considered are close to each other at the final load step, the configuartaions during the load steps are quite different between them.

Fig. 3.39(a) and Fig. 3.39(b) show the load-displacement curves at point A and B in the regular and distorted meshes, repectively. Note that the MITC4+ and new MITC4+ shell elements closely follow the reference curves but the MITC4 shell element shows some difference even in the regular mesh case. The new MITC4+ shell element shows almost similar performance with the MITC4+ shell element, but it is merely better than the MITC4+ shell element.

Chapter 4. Conclusions

The objectives of this thesis were to develop a new 4-node quadrilateral solid (2D-MITC4) and shell (MITC4+) finite elements to improve the predictive capabilities especially in distorted meshes. The proposed elements consist of two key concepts including the new assumed membrane strain field and the geometry dependent Gauss integration scheme. More specifically, the complicated assumed strain field of the previous 2D-MITC4 solid and MITC4+ shell elements are simplified and become more intuitive by directly using the strain coefficients. In addition, the geometry dependent Gauss integration is introduced to improve the membrane performance of the proposed elements.

The geometry dependent Gauss integration with the new assumed strain field provides smoother solutions and good convergence, and thus the proposed elements can be used with relatively coarse meshes. In addition, it needs no additional degrees of freedom and does not reveal any numerical instability that is shown in the incompatible modes element. The new 2D-MITC4 solid and MITC4+ shell elements pass the three basic numerical tests: including zero energy mode, isotropy, and corresponding patch tests. It has been also thoroughly demonstrated that the proposed elements are very effective and reliable both in linear and nonlinear problems.

First, the new 2D-MITC4 solid element was presented in chapter 2. While the simplified assumed strain field is identical to the assumed strain field of the original 2D-MITC4 element, the formulation of the proposed element is much simpler than that of the original 2D-MITC4 element. In addition, a numerical scheme to modify integration points is introduced to make the element insensitive to distortion. The integration points are moved into the element center in accordance with the adjusting parameter which defines the degree of the distortion. The practical requirements for the adjusting parameter are proposed with observations in the eigen analysis of the stiffness matrix depending on the different adjusting parameters. A selected adjusting parameter was proposed as a function of the distortion angle.

Secondly, the new MITC4+ shell element was presented in chapter 3. The generalized assumed strain field is introduced which includes the simplified assumed strain field as a specific case. Here, the new assumed strain field is proposed by merging the tying points into one point at the element center. This new strain field provides a more straightforward formulation compared with the previous MITC4+ shell element. The proposed strain field is collaborated with the transverse shear and membrane locking treatment of the previous MITC4+ shell elements. In addition, the geometry dependent Gauss integration scheme is extended into the shell element to improve its performance. Note that the geometry dependent Gauss integration also changes both bending and transverse shear strain sampling points, but it rarely affects the corresponding behaviors.

For future works, the concept of the geometry dependent Gauss integration could be extended into the low order 3D solid elements. It would be also valuable to find optimal integration points which provide accurate solutions regardless of the type of element distortions.

Appendix A. Physical strain patterns

The physical strain patterns of the physical strain coefficients in Eqs. (2.18)-(2.20) is directly obtained by the characteristic geometry and displacement vectors in Eqs. (2.8)-(2.9). The physical strain patterns for an element with an arbitrary geometry is shown in.Fig. A.1.

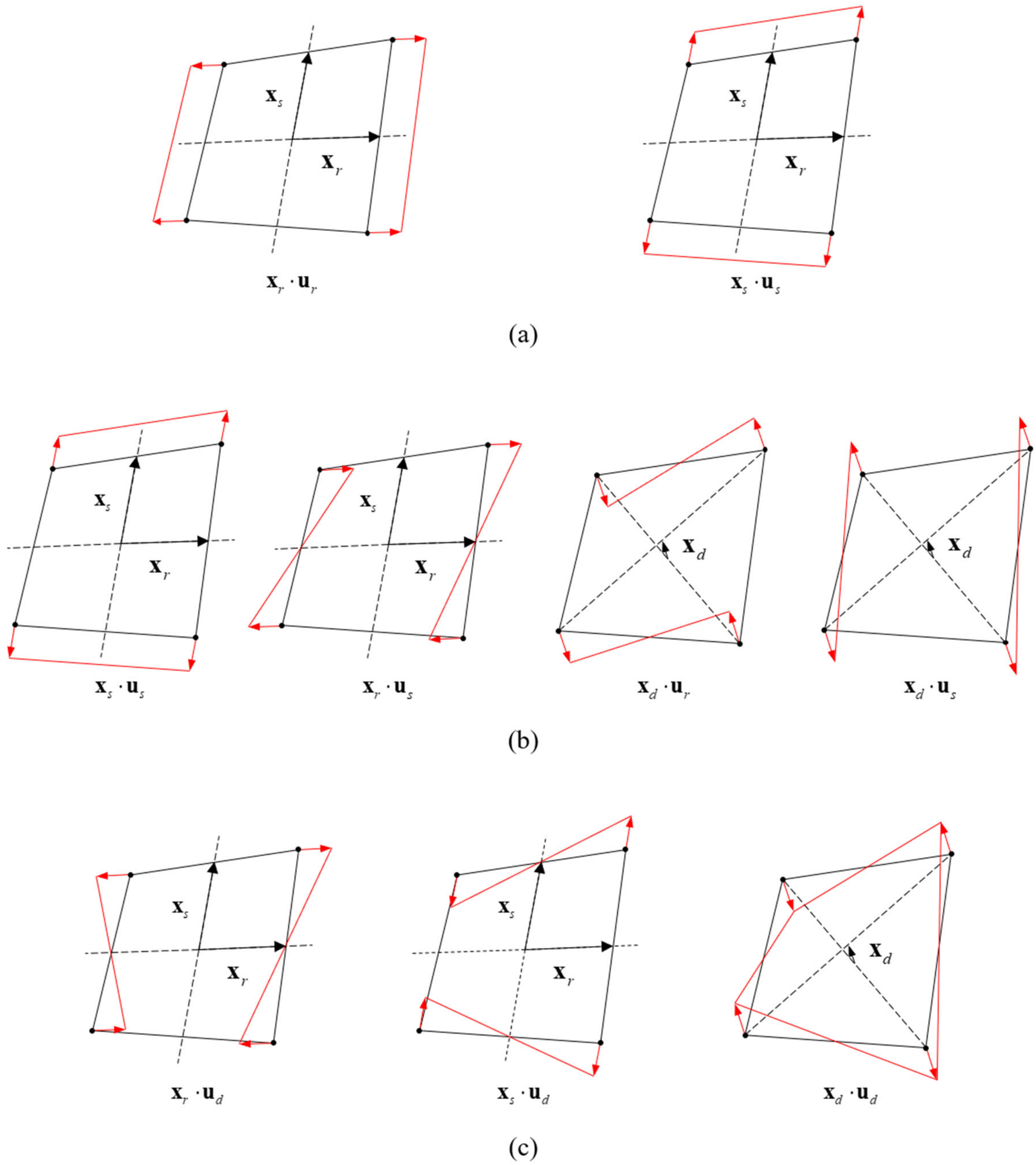

Fig. A.1. Physical strain patterns with the characteristic geometry and displacement vectors. (a) stretching strain patterns, (b) shearing strain patterns, and (c) bending strain patterns.

Appendix B. Modification on Gauss integration point

The various ways to modify Gauss integration are presented and investigated its performance. Although it can be modified in infinitely many arbitrary ways, there are only a few cases to be applied to integrate the stiffness matrix of the finiete elements because the finite element should pass the patch tests. Some cases satisfying the basic properties are shown in Fig. B.1. Of course, there could be another options to modify the position of the Gauss integaration points.

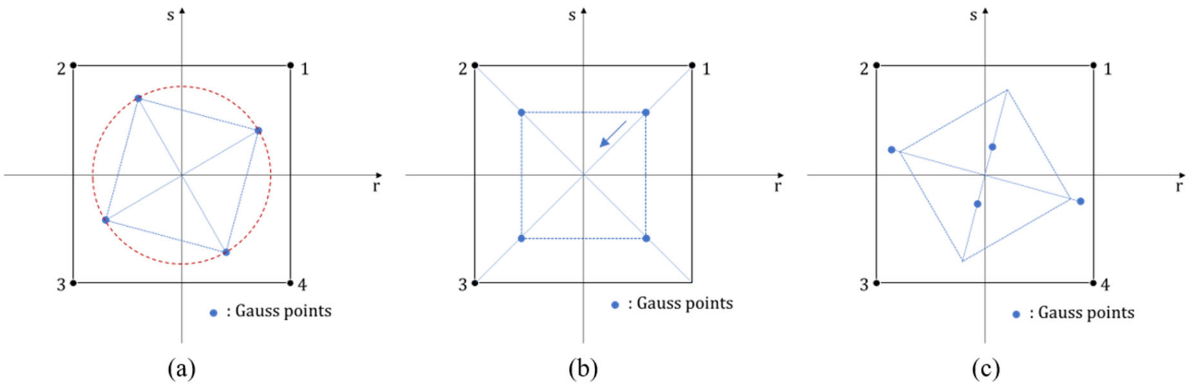

Fig. B.1. Possible ways to modify Gauss integratin points. (a) Rotation, (b) Scaling, and (c) Rotation and scaling.

For the investigation, the Cook's skew beam problem is considered as shown in Fig. 2.16. The ration on Gauss interation points is considered at first in each element as shown in Fig. B.2. It can be seen that the range between minimum and maximum strain energy is small and thus its contribution is not enough to improve the performance. Then, the scaling on Gauss integration points is considered as shown in Fig. B.3. We found that the scaling modfictaion significantly changes the minimum and maximum ragne, and there is an optimal scaling size. Because it is not easy to obtain optimal points analytically, the strain energy from each modification method is calculated by numerical experiment.

Table B.1. Strain energy with modified Gauss integration for Cook's beam with 4x4 elements mesh.

Element	**Gauss integration**	**Strain energy**	**Normalization**
Reference	Standard(3x3)	12.0169	1.0
Q4	Standard	5.899	0.491
ICM-Q4	Standard	10.046	0.836
2D-MITC4	Standard	8.676	0.722
2D-MITC4	Rotation (optimal)	8.719	0.726
2D-MITC4	Scaling (optimal)	11.177	0.930

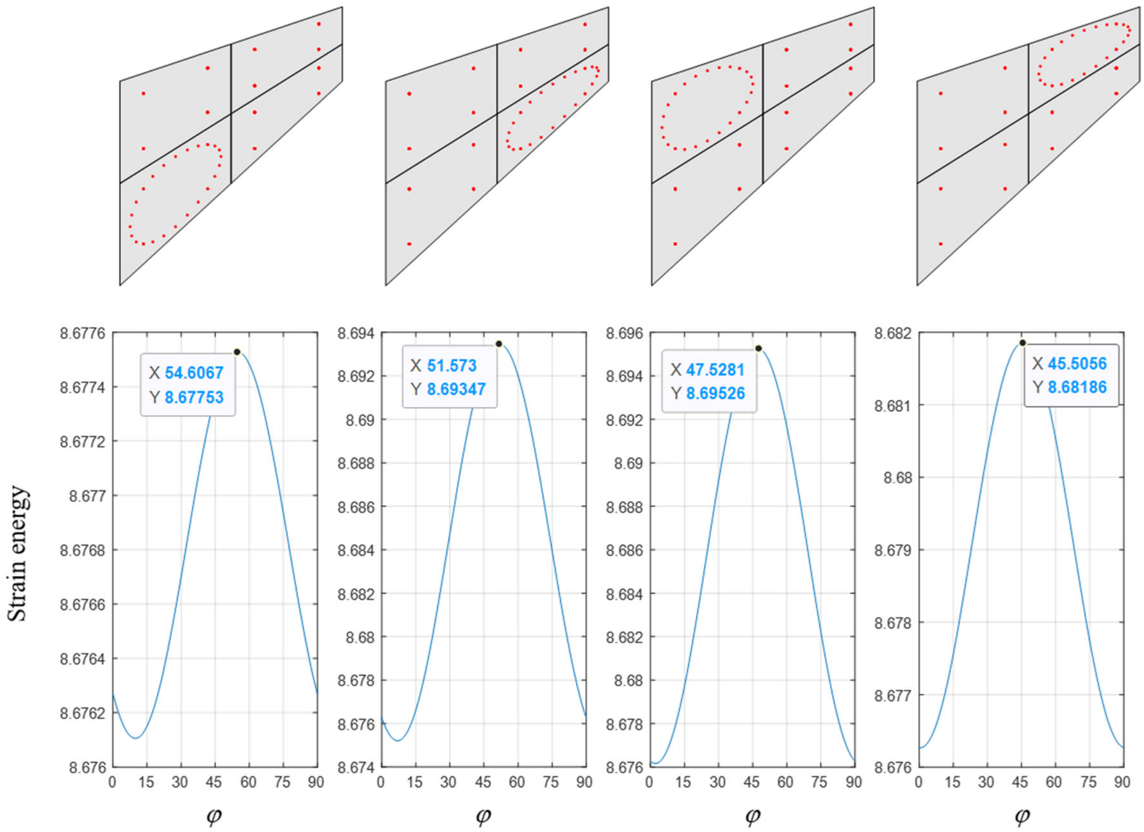

Fig. B.2. Strain energy obtained from rotation modification for each element in Cook's beam.

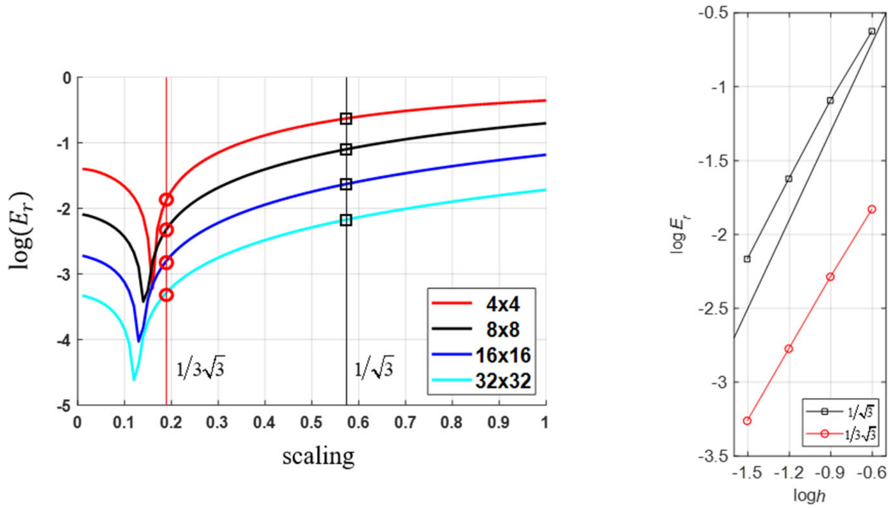

Fig. B.3. Strain energy obtained from scaling modification in Cook's beam.

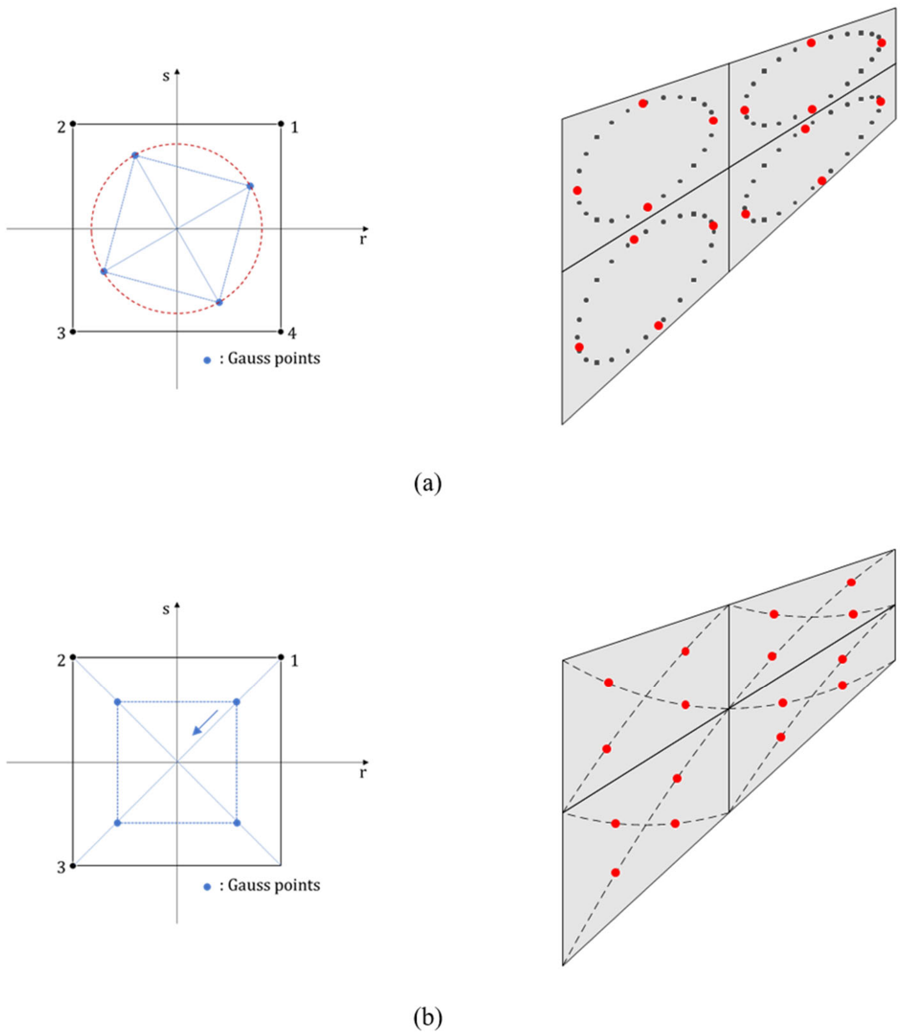

Fig. B.4. Optimally modified Gauss points based on (a) rotation and (b) scaling.

Table B.1 show the strain energy obtrain from the standard element (Q4), incompatible modes element (ICM-Q4), and MITC based element (2D-MITC4). The strain energy is normalized by the reference calculated using 9-node quadrilateral element. The ICM-Q4 element works well when the only standard integration cases are considered. However, for the all cases, the 2D-MITC4 element with scaling modification gives the most accurate solutions.

There is no way to determind the optimal scaling size until iteratively solve the given problem with changing the scaling factor from one to zero. Therefore, a methodology that can appropriately derermind the scaling factor without solving the problem is required. While the quadrilateral solid elements perform well in uniform meshes, they generally show the stiffening effect when they are distorted. This means that the performance could be increased if we modified Gauss integration points based on the element distortion.

For further investigation on the scaling modification, the element distortion is classified and measured by some characteristic values. By coupling the distortion measure to the scaling factor, the modification is tested. For the details, see Appendix C.

Appendix C. Coupling distortion measure with adjusting parameter

In this chapter, it is investigated how to couple the distortion measure with the adjusing parameter that modify Gauss integration poins with scaling. The cantilever beam given in Fig. C.1 is considered. Various functions are designed and tested whether the distortion measure can represent the element distortion and also, the adjusting parameter appropriately modify Gauss integration points.

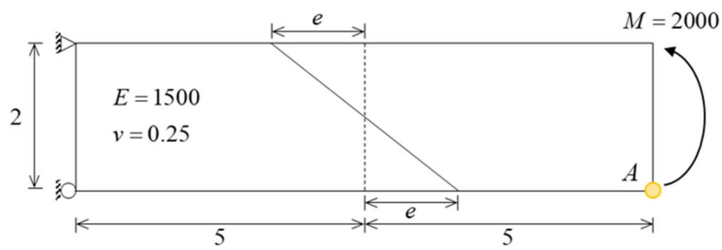

Fig. C.1. Cantilever beam (E = 1500 and v = 0.25) modeled using two elements with distortion parameter (e).

Here, the three distortion measures shown in Fig. C.2 are considred: skewness, tapered, and overall distortion. The skew angle at the element center is used for the skewness distortion, and the two coefficients α and β in Eq. (2.45) are used for the r and s directional tapered distortion, respectively. In addition, the Γ is defined to assess the overall distortion of the element including skewness, tapered and length ratios.

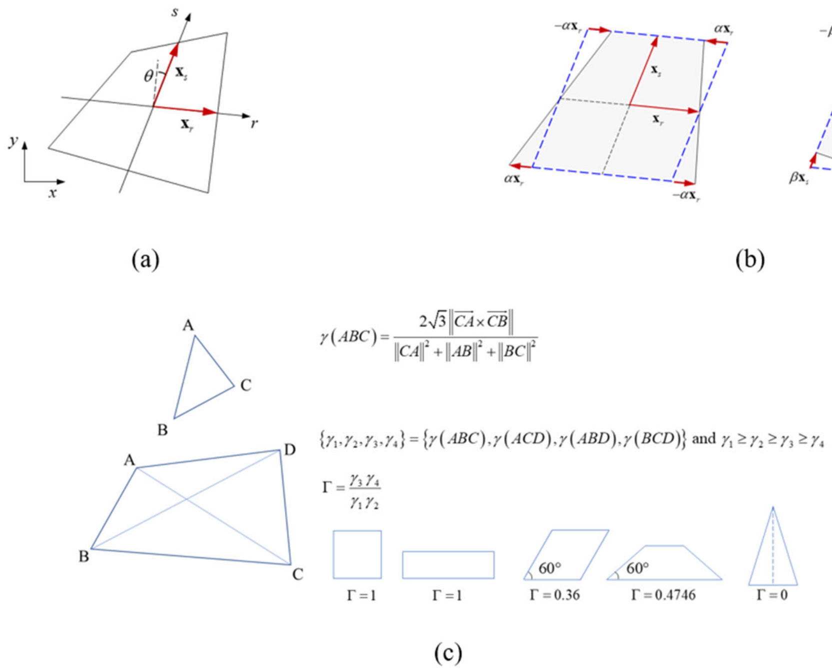

Fig. C.2. Distortion measures. (a) skewness, (b) tapered, and (c) overall distortion.

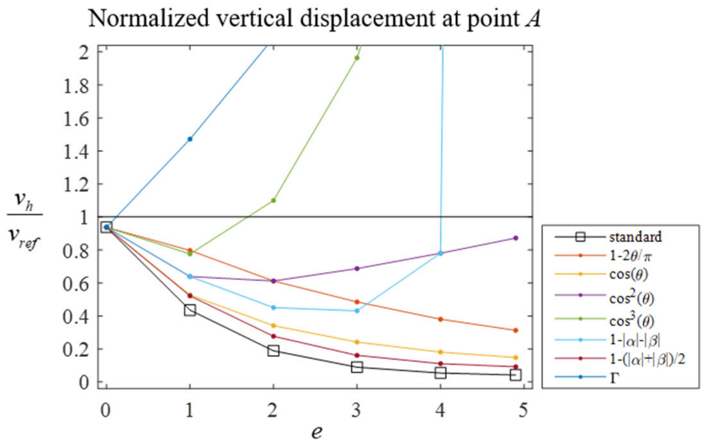

Fig. C.3. Normalized vertical displacement in the cantilever beam with two elements at point A

The adjusting parameter should satisfy the proposed requirements for general use in chatper 2. We checked that all the parameters considered here passes the zeros energy modes and patch tests. Therefore, the performance depending on the element distortion is the main concern.

Among the various test functions considered in Fig. C.3, the cosine square function give accurate and reliable solutions for the whole range in the distortion parameter. For some patial ranges $e \in [0, 2]$, cosine or cosine cubic give more accurate than the cosine square, but they soon fail to give reliable solutions when the distortion becomes large. Therefore, the cosine square function is most pertinent as a adjusting parameter in the group of the functions tested in this problem.

Based on this investigation, the cosine square function is adopted to modify Gauss integration points. Note that the distortion measure is obtained from the skew angle of the element center which is determinded from the element geometry only. Thus, there is no artificial coefficient that the user shoul define. In addition, the modification of Gauss integration points hardly increasesthe computational cost, since the distortion measure could be naturally calculated when construct the assumed field of the 2D-MITC4 element.

Bibliography

[1] Bathe KJ. Finite element procedures. Prentice Hall; 1996, 2nd ed. K.J. Bathe, Watertown, MA; 2014 and Higher Education Press, China; 2016.

[2] Cook RD. Concepts and applications of finite element analysis. John Wiley & Sons, New York; 2007.

[3] Hughes TJR. The finite element method: linear static and dynamic finite element analysis. Dover Publications, Mineola, NY; 2000.

[4] Lee N-S, Bathe K-J. Effects of element distortions on the performance of isoparametric elements. Int J Numer Methods Eng 1993;36:3553–76.

[5] Jung J, Jun H, Lee P-S. Self-updated four-node finite element using deep learning. Comput Mech 2022;69:23–44.

[6] Macneal RH. A theorem regarding the locking of tapered four-noded membrane elements. Int J Numer Methods Eng 1987;24:1793–9.

[7] Panasz P, Wisniewski K, Turska E. Reduction of mesh distortion effects for nine-node elements using corrected shape functions. Finite Elem Anal Des 2013;66:83–95.

[8] MacNeal RH. Toward a defect-free four-noded membrane element. Finite Elem Anal Des 1989;5:31–7.

[9] Jung J, Yoon K, Lee PS. Deep learned finite elements. Comput Methods Appl Mech Eng 2020;372:113401

[10] Kim HJ, Yoon K, Lee PS. Continuum mechanics based beam elements for linear and nonlinear analyses of multi-layered composite beams with interlayer slips. Compos Struct 2020;235:111740. https://doi.org/10.1016/j.compstruct.2019.111740.

[11] Ko Y, Bathe KJ. A new 8-node element for analysis of three-dimensional solids. Comput Struct 2018;202:85–104. https://doi.org/10.1016/j.compstruc.2018.02.015.

[12] Lee C, Kim S, Lee PS. The strain-smoothed 4-node quadrilateral finite element. Comput Methods Appl Mech Eng 2021;373:113481. https://doi.org/10.1016/j.cma.2020.113481.

[13] Hyun C, Lee PS. A load balancing algorithm for the parallel automated multilevel substructuring method. Comput Struct 2021;257:106649. https://doi.org/10.1016/j.compstruc.2021.106649.

[14] Wisniewski K, Turska E. Improved nine-node shell element MITC9i with reduced distortion sensitivity. Comput Mech 2018;62:499–523. https://doi.org/10.1007/s00466-017-1510-4.

[15] Barlow J. More on optimal stress points—reduced integration, element distortions and error estimation. Int J Numer Methods Eng 1989;28:1487–504. https://doi.org/10.1002/nme.1620280703.

[16] Jung J, Yoon K, Lee PS. Deep learned finite elements. Comput Methods Appl Mech Eng 2020;372:113401. https://doi.org/10.1016/j.cma.2020.113401.

[17] Zienkiewicz OC, Taylor RL, Too JM. Reduced integration technique in general analysis of plates and shells. Int J Numer Methods Eng 1971;3:275–90.

[18] Belytschko T, Tsay C -S. A stabilization procedure for the quadrilateral plate element with one-point quadrature. Int J Numer Methods Eng 1983;19:405–19.

[19] Malkus DS, Hughes TJR. Mixed finite element methods - Reduced and selective integration techniques:

A unification of concepts. Comput Methods Appl Mech Eng 1978;15:63–81.

[20] Griffiths D V, Mustoe GGW. Selective Reduced Integration of Four-Node Plane Element in Closed Form. J Eng Mech 1995;121:725–9.

[21] Simo JC, Rifai MS. A class of mixed assumed strain methods and the method of incompatible modes. Int J Numer Methods Eng 1990;29:1595–638.

[22] Bischoff M, Ramm E, Braess D. A class of equivalent enhanced assumed strain and hybrid stress finite elements. Comput Mech 1999;22:443–9.

[23] Kožar I, Rukavina T, Ibrahimbegović A. Method of incompatible modes – overview and application. J Croat Assoc Civ Eng 2018;70:19–29.

[24] Wilson EL, Taylor RL, Doherty WP, Ghaboussi J. Incompatible Displacement Models. ACADEMIC PRESS, INC.; 1973.

[25] Taylor RL, Beresford PJ, Wilson EL. A non-conforming element for stress analysis. Int J Numer Methods Eng 1976;10:1211–9.

[26] Bischoff M, Romero I. A generalization of the method of incompatible modes. Int J Numer Methods Eng 2007;69:1851–68.

[27] Wilson EL, Ibrahimbegovic A. Use of incompatible displacement modes for the calculation of element stiffnesses or stresses. Finite Elem Anal Des 1990;7:229–41.

[28] Sussman T, Bathe KJ. Spurious modes in geometrically nonlinear small displacement finite elements with incompatible modes. Comput Struct 2014;140:14–22.

[29] Dvorkin EN, Bathe K. A continuum mechanics based four-node shell element for general nonlinear analysis. Eng Comput 1984;1:77–88. https://doi.org/10.1108/eb023562.

[30] Ko Y, Lee PS, Bathe KJ. A new 4-node MITC element for analysis of two-dimensional solids and its formulation in a shell element. Comput Struct 2017;192:34–49.

[31] Bucalem ML, Bathe K -J. Higher-order MITC general shell elements. Int J Numer Methods Eng 1993;36:3729–54.

[32] Bathe KJ, Lee PS, Hiller JF. Towards improving the MITC9 shell element. Comput Struct 2003;81:477–89.

[33] Lee PS, Bathe KJ. Development of MITC isotropic triangular shell finite elements. Comput Struct 2004;82:945–62.

[34] Beirão da Veiga L, Chapelle D, Paris Suarez I. Towards improving the MITC6 triangular shell element. Comput Struct 2007;85:1589–610.

[35] Lee Y, Lee PS, Bathe KJ. The MITC3+ shell element and its performance. Comput Struct 2014;138:12–23.

[36] Ko Y, Lee PS, Bathe KJ. A new MITC4+ shell element. Comput Struct 2017;182:404–18.

[37] Ko Y, Lee PS. A 6-node triangular solid-shell element for linear and nonlinear analysis. Int J Numer Methods Eng 2017;111:1203–30.

[38] Ko Y, Lee PS, Bathe KJ. The MITC4+ shell element in geometric nonlinear analysis. Comput Struct 2017;185:1–14.

[39] Ko Y, Lee Y, Lee PS, Bathe KJ. Performance of the MITC3+ and MITC4+ shell elements in widely-used

benchmark problems. Comput Struct 2017;193:187–206.
[40] Jun H, Yoon K, Lee PS, Bathe KJ. The MITC3+ shell element enriched in membrane displacements by interpolation covers. Comput Methods Appl Mech Eng 2018;337:458–80.
[41] Dvorkin EN, Vassoloâœ SI. A quadrilateral 2-D finite element based on mixed interpolation of tensorial components. Eng Comput 1989;6:217–24. https://doi.org/10.1108/eb023777.
[42] Robinson J. CRE method of element testing and the Jacobian shape parameters*. Eng Comput 1987;4:113–8. https://doi.org/10.1108/eb023689.
[43] Stander N, Wilson EL. A 4-node quadrilateral membrane element with in-plane vertex rotations and modified reduced quadrature. Eng Comput 1989;6:266–71.
[44] Reddy BD, Küssner M. The four-noded quadrilateral with a 2 × 1 integration rule: Application to plates and other problems. Comput Methods Appl Mech Eng 1997;149:101–12.
[45] Oishi A, Yagawa G. Computational mechanics enhanced by deep learning. Comput Methods Appl Mech Eng 2017;327:327–51.
[46] Chen XM, Cen S, Long YQ, Yao ZH. Membrane elements insensitive to distortion using the quadrilateral area coordinate method. Comput Struct 2004;82:35–54. https://doi.org/10.1016/j.compstruc.2003.08.004.
[47] Cen S, Chen XM, Fu XR. Quadrilateral membrane element family formulated by the quadrilateral area coordinate method. Comput Methods Appl Mech Eng 2007;196:4337–53. https://doi.org/10.1016/j.cma.2007.05.004.
[48] Long ZF, Cen S, Wang L, Fu XR, Long YQ. The third form of the quadrilateral area coordinate method (QACM-III): Theory, application, and scheme of composite coordinate interpolation. Finite Elem Anal Des 2010;46:805–18. https://doi.org/10.1016/j.finel.2010.04.008.
[49] Sze KY. On immunizing five-beta hybrid-stress element models from “trapezoidal locking” in practical analyses. Int J Numer Methods Eng 2000;47:907–20. https://doi.org/10.1002/(SICI)1097-0207(20000210)47:4<907::AID-NME808>3.0.CO;2-A.
[50] Bucalem ML, Bathe KJ. Finite element analysis of shell structures. Arch Comput Methods Eng 1997;4:3–61. https://doi.org/10.1007/BF02818930.
[51] Lee C, Lee PS. The strain-smoothed MITC3+ shell finite element. Comput Struct 2019;223:106096. https://doi.org/10.1016/j.compstruc.2019.07.005.
[52] Lee C, Lee DH, Lee PS. The strain-smoothed MITC3+ shell element in nonlinear analysis. Comput Struct 2022;266:106768. https://doi.org/10.1016/j.compstruc.2022.106768.
[53] Belytschko T, Leviathan I. Projection schemes for one-point quadrature shell elements. Comput Methods Appl Mech Eng 1994;115:277–86. https://doi.org/10.1016/0045-7825(94)90063-9.
[54] Lee Y, Yoon K, Lee PS. Improving the MITC3 shell finite element by using the Hellinger-Reissner principle. Comput Struct 2012;110–111:93–106. https://doi.org/10.1016/j.compstruc.2012.07.004.
[55] Sussman T, Bathe KJ. 3D-shell elements for structures in large strains. Comput Struct 2013;122:2–12. https://doi.org/10.1016/j.compstruc.2012.12.018.
[56] Bathe KJ, Iosilevich A, Chapelle D. Evaluation of the MITC shell elements. Comput Struct 2000;75:1–30. https://doi.org/10.1016/S0045-7949(99)00214-X.
[57] Roh HY, Cho M. The application of geometrically exact shell elements to B-spline surfaces. Comput

Methods Appl Mech Eng 2004;193:2261–99. https://doi.org/10.1016/j.cma.2004.01.019.

[58] Belytschko T, Leviathan I. Physical stabilization of the 4-node shell element with one point quadrature. Comput Methods Appl Mech Eng 1994;113:321–50. https://doi.org/10.1016/0045-7825(94)90052-3.

[59] Kulikov GM, Plotnikova S V. A family of ANS four-node exact geometry shell elements in general convected curvilinear coordinates. Int J Numer Methods Eng 2010;83:1376–406. https://doi.org/10.1002/nme.2872.

[60] Mi Y, Yu X. Isogeometric MITC shell. Comput Methods Appl Mech Eng 2021;377:113693. https://doi.org/10.1016/j.cma.2021.113693.

[61] Batoz J-L, Bathe K-Jür, Ho L-W. A study of three-node triangular plate bending elements. Int J Numer Methods Eng 1980;15:1771–812. https://doi.org/10.1002/nme.1620151205.

[62] Choi C-K, Paik J-G. An efficient four node degenerated shell element based on the assumed covariant strain. Struct Eng Mech 1994;2:17–34. https://doi.org/10.12989/sem.1994.2.1.017.

[63] Belytschko T, Wong BL, Stolarski H. Assumed strain stabilization procedure for the 9-node Lagrange shell element. Int J Numer Methods Eng 1989;28:385–414. https://doi.org/10.1002/nme.1620280210.

[64] Prathap G. A C0 continuous four-noded cylindrical shell element. Comput Struct 1985;21:995–9. https://doi.org/10.1016/0045-7949(85)90212-3.

[65] Kizio S, Schweizerhof K, Düster A, Rank E, others. Benchmark Computations of low and high order Shell Elements on adaptively generated FE Meshes. Proceedings 2006;10:311–30.

[66] Dvorkin EN. Nonlinear analysis of shells using the MITC formulation. Arch Comput Methods Eng 1995;2:1–50. https://doi.org/10.1007/BF02904994.

[67] Bathe K-J, Dvorkin EN. A four-node plate bending element based on Mindlin/Reissner plate theory and a mixed interpolation. Int J Numer Methods Eng 1985;21:367–83. https://doi.org/10.1002/nme.1620210213.

[68] Jeon HM, Lee PS, Bathe KJ. The MITC3 shell finite element enriched by interpolation covers. Comput Struct 2014;134:128–42. https://doi.org/10.1016/j.compstruc.2013.12.003.

[69] Bathe K -J, Dvorkin EN. A formulation of general shell elements—the use of mixed interpolation of tensorial components. Int J Numer Methods Eng 1986;22:697–722. https://doi.org/10.1002/nme.1620220312.

[70] Ko Y, Lee PS, Bathe KJ. The MITC4+ shell element and its performance. Comput Struct 2016;169:57–68. https://doi.org/10.1016/j.compstruc.2016.03.002.

[71] Hiller JF, Bathe KJ. Measuring convergence of mixed finite element discretizations: An application to shell structures. Comput Struct 2003;81:639–54. https://doi.org/10.1016/S0045-7949(03)00010-5.

[72] Bathe KJ, Lee PS. Measuring the convergence behavior of shell analysis schemes. Comput Struct 2011;89:285–301. https://doi.org/10.1016/j.compstruc.2010.09.007.

[73] Bathe KJ, Iosilevich A, Chapelle D. Inf-sup test for shell finite elements. Comput Struct 2000;75:439–56. https://doi.org/10.1016/S0045-7949(99)00213-8.

[74] Chapelle D. The mathematical shell model underlying general shell elements. Int J Numer Methods Eng 2000:1–26.

[75] Urgen Bathe K-J. The inf-sup condition and its evaluation for mixed finite element methods. Comput Struct 2001;79:243–52.

[76] Lee PS, Bathe KJ. Insight into finite element shell discretizations by use of the "basic shell mathematical model." Comput Struct 2005;83:69–90. https://doi.org/10.1016/j.compstruc.2004.07.005.

[77] Lee PS, Bathe KJ. The quadratic MITC plate and MITC shell elements in plate bending. Adv Eng Softw 2010;41:712–28. https://doi.org/10.1016/j.advengsoft.2009.12.011.

[78] 이필승, 노혁천. 쉘 구조물의 유한요소해석에 대하여. 대한토목학회 논문집 A 2007;27:277–89.

[79] Lee Y, Jeon HM, Lee PS, Bathe KJ. The modal behavior of the MITC3+ triangular shell element. Comput Struct 2015;153:148–64. https://doi.org/10.1016/j.compstruc.2015.02.033.

[80] Vampa V. Analysis of in-layer strains in the low order MITC shell element. Lat Am J Solids Struct 2007;4:87–102.

[81] Lee PS, Bathe KJ. On the asymptotic behavior of shell structures and the evaluation in finite element solutions. Comput Struct 2002;80:235–55. https://doi.org/10.1016/S0045-7949(02)00009-3.

[82] Wagner W, Gruttmann F. An improved quadrilateral shell element based on the Hu–Washizu functional. Adv Model Simul Eng Sci 2020;7. https://doi.org/10.1186/s40323-020-00162-5.

[83] Sze KY, Liu XH, Lo SH. Popular benchmark problems for geometric nonlinear analysis of shells. Finite Elem Anal Des 2004;40:1551–69. https://doi.org/10.1016/j.finel.2003.11.001.

[84] Jeon HM, Lee Y, Lee PS, Bathe KJ. The MITC3+ shell element in geometric nonlinear analysis. Comput Struct 2015;146:91–104. https://doi.org/10.1016/j.compstruc.2014.09.004.

[85] Macneal RH, Harder RL. A proposed standard set of problems to test finite element accuracy. Finite Elem Anal Des 1985;1:3–20. https://doi.org/10.1016/0168-874X(85)90003-4.